INFORMATION TO USERS

This manuscript has been reproduced from the microfilm master. UMI films the text directly from the original or copy submitted. Thus, some thesis and dissertation copies are in typewriter face, while others may be from any type of computer printer.

The quality of this reproduction is dependent upon the quality of the copy submitted. Broken or indistinct print, colored or poor quality illustrations and photographs, print bleedthrough, substandard margins, and improper alignment can adversely affect reproduction.

In the unlikely event that the author did not send UMI a complete manuscript and there are missing pages, these will be noted. Also, if unauthorized copyright material had to be removed, a note will indicate the deletion.

Oversize materials (e.g., maps, drawings, charts) are reproduced by sectioning the original, beginning at the upper left-hand corner and continuing from left to right in equal sections with small overlaps.

Photographs included in the original manuscript have been reproduced xerographically in this copy. Higher quality 6" x 9" black and white photographic prints are available for any photographs or illustrations appearing in this copy for an additional charge. Contact UMI directly to order.

Bell & Howell Information and Learning
300 North Zeeb Road, Ann Arbor, MI 48106-1346 USA
800-521-0600

Mathematical Modeling of the Hot Strip Rolling of Nb Microalloyed Steels

by

Fulvio Siciliano Jr.

A Thesis Submitted to the Faculty of Graduate Studies and Research in Partial Fulfillment of the Requirements for the Degree of Doctor of Philosophy

Department of Mining and Metallurgical Engineering
McGill University
Montreal, Canada

February 1999

ABSTRACT

Industrial mill logs from 7 different hot strip mills were analyzed in order to calculate the mean flow stresses developed in each stand. The schedules were typical of the processing of Nb microalloyed, multiply-alloyed and plain C-Mn steels. The calculations, based on the Sims analysis, take into account work roll flattening, redundant strain and the forward slip ratio. The measured stresses are then compared with the predictions of a model based on an improved Misaka mean flow stress equation, in which solute effects, strain accumulation, as well as the kinetics of static and metadynamic recrystallization are fully accounted for. Good agreement between the measured and predicted mean flow stresses is obtained over the whole range of rolling temperatures. The evolution of grain size and the fractional softening are also predicted by the model during all stages of strip rolling. Special attention was paid to the Nb steels, in which the occurrence of Nb(C,N) precipitation strongly influences the rolling behaviour, preventing softening between passes. The present study leads to the conclusion that Mn addition retards the strain-induced precipitation of Nb. By contrast, Si addition has an accelerating effect. The model calculates the critical strain for the onset of dynamic recrystallization in Nb steels. It shows that the critical strain/peak strain ratio decreases with increasing Nb content, and that Mn and Si have marginal but opposite effects. It is demonstrated that dynamic recrystallization followed by metadynamic recrystallization occurs under most conditions of hot strip rolling, during the initial passes due to the high strains, low strain rates and high temperatures, or in the final passes as a consequence of strain accumulation.

RÉSUMÉ

Les relevés de production provenant de 7 laminoirs à bandes à chaud différents ont été analysés dans le but de calculer la contrainte d'écoulement moyenne développée à chaque passe. Les programmes opératoires sont représentatifs de ceux utilisés pour des aciers: *a)* micro-alliés au niobium, *b)* fortement alliés, et *c)* des aciers doux au manganèse. Les calculs, basés sur l'analyse de Sims, prennent en compte l'écrasement élastique des rouleaux, la déformation redondante et le taux de glissement. Les contraintes mesurées ont ensuite été comparées avec les prédictions d'un modèle basé sur l'équation modifiée de la contrainte moyenne d'écoulement de Misaka, dans laquelle les effets des solutés, de la déformation accumulée mais aussi des recristallisations statique et dynamique sont pris en compte. Les résultats mesurés et prédits sont en bon accord sur toute la plage de température de laminage.

L'évolution de la taille de grain et de l'adoucissement sont aussi prédits par le modèle à toutes les étapes du laminage des bandes. Une attention particulière a été portée aux aciers au niobium, dans lesquels la précipitation des composés de type Nb(C,N) affecte fortement le comportement au laminage en diminuant l'adoucissement entre les passes. Cette étude conduit à la conclusion que l'addition de manganèse retarde la précipitation du niobium induite par déformation. Par opposition, l'addition de silicium a un effet accélérateur. Le modèle permet le calcul du taux de déformation critique pour l'apparition de la recristallisation dynamique. Il montre que le rapport entre le taux de déformation critique et le taux de déformation correspondant à la contrainte maximum décroît lorsque la concentration de niobium augmente, et que le manganèse et le silicium ont des effets faibles mais de sens contraire. On montre que la recristallisation dynamique suivie de la recristallisation méta-dynamique se produit dans la plupart des conditions de laminage à chaud, au cours des premières passes à cause des déformations élevées, de la faible vitesse de déformation et de la température élevée, et dans les passes finales en raison de la déformation accumulée.

RESUMO

Dados de laminação de tiras a quente provenientes de 7 laminadores diferentes foram analisados para calcular a tensão média de escoamento (ou tensão média equivalente-TME) desenvolvida em cada passe. As seqüências de passes analisadas são típicas do processamento de aços microligados ao nióbio, aços ligados ao Cr e Mo e aços C-Mn. Os cálculos, baseados no modelo de Sims, levam em conta o achatamento do cilindro de trabalho, a deformação redundante e o escorregamento entre a tira e o cilindro. As tensões medidas foram então comparadas com previsões de um modelo matemático, basedo na equação de Misaka melhorada para levar em conta os efeitos: *(i)* da adição de elementos de liga em solução sólida, *(ii)* do acúmulo de deformação e *(iii)* das cinéticas de recristalização estática e metadinâmica. Obteu-se boa previsão de TME numa vasta faixa de temperaturas de laminação. A evolução de tamanhos de grão e do amaciamento entre passes são também previstos pelo modelo durante todos os estágios da laminação de tiras. Atenção especial foi dada aos aços microligados ao nióbio, nos quais a ocorrência de precipitação de Nb(C,N) influencia fortemente o comportamento em laminação, impedindo o amaciamento entre passes. O presente estudo leva a concluir que a adição de Mn atrasa a precipitação de Nb(C,N) induzida por deformação. Por outro lado, adições de Si têm efeito acelerador. O modelo calcula a deformação crítica para o início da recristalização dinâmica nos aços ao Nb. É mostrado que a razão entre a deformação crítica e a deformação de pico diminui com o aumento do teor de Nb e também que os elementos Mn e Si exercem efeitos secundários, mas opostos. O estudo mostra que a recristalização dinâmica seguida pela metadinâmica ocorre na maioria dos casos de laminação de tiras a quente, seja nos passes iniciais devido a altas deformações, baixas taxas de deformação e altas temperaturas, ou nos passes finais, como conseqüência do acúmulo de deformações.

ACKNOWLEDGMENTS

I would like to express my sincere thanks to all those who made this work possible and to whom I owe so much.

To Professor John J. Jonas, my thesis supervisor, for his guidance and support throughout this work; with his kind and experienced nature. Working with Prof. Jonas is like playing the blues with B.B. King or the bossa nova with A.C. Jobim.

To Professor Terrence M. Maccagno (University of Alberta, Edmonton, Canada), Mr. Koji Minami (Trico Steel Corp., Decatur, AL, USA) and Mr. Atsushi Kirihata (Sumitomo Metal Industries, Wakayama, Japan) with whom I had the pleasure of working in different stages of my research.

To Professors Peter D. Hodgson (Deakin University, Geelong, Australia), C. Michael Sellars (University of Sheffield, U.K.), Hugh J. McQueen (Concordia University, Montreal, Canada) and Oscar Balancin (Dema-UFSCAR, São Carlos, Brazil) for their helpful suggestions and several useful discussions.

To Mr. Brian D. Nelson (Dofasco Steel Inc., Hamilton, Canada), Mr. Brian J. McCrady (Algoma Steel Inc., Sault Ste. Marie, Canada) and Dr. Chris Killmore (BHP Steel, Port Kembla, Australia) for supplying extensive mill log data and materials related to this work.

To Professors Angelo F. Padilha and José D.T. Capocchi (Escola Politécnica da Universidade de São Paulo, Brazil) for supporting me when no one else did, and to Mr. Pascoal Bordignon (CBMM-Brazil) for his aid in the final stages of this research. I am grateful for all their help to make this investigation possible.

To Mrs. Lorraine Mello and Mr. Edwin Fernandes for their smiling faces, good humor and for all kinds of metallurgical and non-metallurgical help.

To my family and friends, my invaluable treasures, who gave me short and long-distance support and encouragement throughout my stay in Montreal.

Finally, I thank the Conselho Nacional de Desenvolvimento Científico e Tecnológico-CNPq, Brazil, for financial support.

Thank you, merci, obrigado!

I dedicate this thesis to my parents, Leila and Fulvio, from whom I learned all I needed to know.

TABLE OF CONTENTS

LIST OF FIGURES

LIST OF TABLES

LIST OF SPREADSHEETS

Chapter 1 - Introduction

Most of the metallic materials produced commercially undergo at least one hot deformation stage during their fabrication. Such processing leads to the production of plates, strips, rods, pipes, etc. at low cost when compared to the cold deformation/annealing route. Comprehensive study of the metallurgical phenomena associated with hot deformation has considerable potential application in the control of industrial processes. However, investigations in the hot deformation field usually require appreciable effort and specialized equipment. The temperatures involved for most metals, especially steels, make the direct observation of mechanisms very difficult. Special attention must be given to steels, the most important metallic material in terms of history, present and future. Most steels are ferritic at ambient temperatures and hot deformation is, by definition, performed in the austenite phase. Therefore, study of the metallurgical mechanisms taking place during the hot deformation of steels involves a great deal of creativity, imagination and hard work.

The topic selected in this study is the mathematical modeling of flow stress and microstructure during the hot strip rolling of steels. This includes such microstructural aspects as hardening and softening. Here, the niobium microalloyed steels play the main role, but plain C-Mn steels are also of interest, and a few multiply-alloyed grades as well. Special attention is given to the large-scale softening process concurrent with deformation known as dynamic recrystallization and its occurrence during industrial hot strip rolling. Some laboratory work was also performed in this investigation. However, most of the study is based on data supplied by various steel plants from around the world. These data are considered to come from the laboratory of "real life"

and are analyzed in some detail here. In this case, no extrapolation from laboratory observations to the actual industrial process was needed.

1.1-The Hot Strip Mill (HSM)

The multiple stand finishing mill is one of the most productive machines in a steel plant. It consists of 6 or 7 tandem stands, each in a four-high configuration. Devices such as loopers, automatic gauge controllers, work roll benders, descalers, coilboxes and others are usually present in these complex machines. A schematic

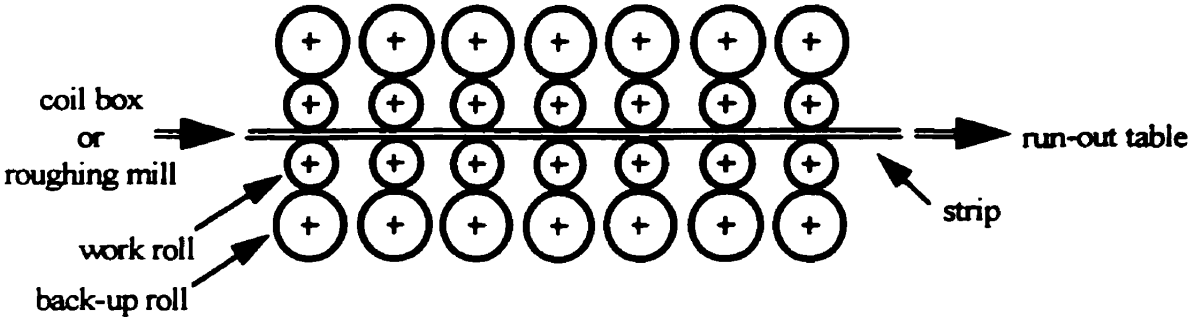

Figure 1.1 Schematic representation of a hot strip mill

representation is provided in Figure 1.1. Data acquisition is done by load cells, work roll rotational speed sensors, gauge sensors and optical pyrometers located before the first pass and after the last stand (there are some mills with an interstand pyrometer). The pyrometers are amongst the most important devices and the temperature accuracy can be improved by processing the pyrometer readings through a temperature model. The latter can correct for temperature gradients between the surface, center and edges, as well as for scale formation. Numerous operational constraints apply to HSM's; as a result, there is generally no way to change a single parameter without changing the others.

1.2-Advantages and Basic Types of Mathematical Modeling

Hodgson [1] has carried out an excellent analysis of the different types of mathematical models and has supplied a list of the advantages associated with the application of a particular model to a given practical situation. According to this author, the main types of models fall into the following categories [1]:

A) Phenomenological: These describe the actual physical processes that occur. Typical examples are differential equations for heat and material flow. Very few microstructural events are modeled at this level of detail.

B) Empirical: These are characterized by the empirical analysis of data. The aim of this approach is to provide relationships between the process variables and parameters of interest. While simple regressions have been the most applied technique, there are increasing numbers of sophisticated methods available for constructing empirical models.

C) Semi-Empirical: These combine certain features of the above two methods. An example of this type is the modeling of the high temperature recrystallization behavior of austenite. Mathematical models for the recrystallization kinetics use an Arrhenius temperature term combined with expressions relating the changes in the driving and drag forces (strain, dislocation density and particle/solute drag), and the surface area per unit volume (grain size and morphology). Such relationships have a fair degree of universality, although they are essentially empirical in nature.

D) Heuristic: These include the rule-based models that are now gaining widespread acceptance within the steel industry. These models do not contain mathematical representations of the physical processes, but predict the outcome of a series of events on the basis of previous experience. The application of neural networks to predict the rolling force is a current example of this type [2,3].

Taking into account the cost and time spent in industrial experiments and trials, it is possible to list the following benefits that arise from improvements in model accuracy:

1) Reduction in the number of mill trials

This is one of the obvious advantages. It is desirable to reduce the frequency of mill trials because of the high costs involved. The time lost to production, the possible generation of high quantities of scrap, as well as the associated personnel and delay costs are the most important factors justifying simulation and modeling.

2) Evaluation of hardware modifications

This possibility offers the greatest benefit of model development in hot rolling. Changes in mill configuration can be carefully tested and assessed by modeling. Also, personnel training can be accomplished prior to the change or installation of the equipment.

3) Prediction of variables that cannot be measured

One important and simple example is the internal temperature of steel during rolling. In certain processes, there is a very little correspondence between surface pyrometer measurements and the bulk temperature. Similar considerations apply to microstructural evolution during rolling; the austenite grain size, start time of precipitation, and other parameters cannot be measured, but must be evaluated with the aid of a mathematical model.

4) The effect of interactions

Modeling creates the possibility of studying more than one parameter at a time. This is useful because, in thermomechanical processing, there are important interactions between the thermal, mechanical and microstructural phenomena.

5) Model-based control

The use of model-based on-line control systems in hot rolling should increase in the years to come. It has been found that when semi-empirical models are employed in control environments, more flexibility and better performance can be achieved. It is also possible to use modeling in off-line simulations as well.

6) Inexpensive research

When simple numerical methods are used, the experimental costs are almost negligible. When employed in association with mechanical testing, the costs are still quite low in comparison with mill trials. The flexibility of simulation and modeling is also extensive, permitting the generation of large quantities of data, without incurring appreciable costs, beyond the time of the personnel involved.

The applicability of any model must be intensively tested in advance, preferably with industrial data. After improved accuracy in predicting the operational parameters has been demonstrated, it may be applied to production.

1.3-Aims of this Investigation

The aim of this work was basically to answer the four questions listed below:

- Does dynamic recrystallization take place during hot strip rolling?
- How does the Nb concentration change the critical strain for the onset of dynamic recrystallization?
- How do the Mn and Si concentrations influence Nb carbonitride precipitation?
- Are current controlled rolling theories and models consistent with mill log observations?

These questions will be considered in the pages that follow.

Chapter 2 - Literature Review

Some of the basic mechanisms and mathematical models relevant to this work will now be described briefly in the pages that follow.

2.1-Calculation of Mean Flow Stress

The mean flow stress (MFS) is defined as the area under a given stress-strain curve for the strain interval selected. With reference to Figure 2.1, the MFS between strains ε_0 and ε_1 is calculated as follows:

$$MFS = \frac{1}{\varepsilon_1 - \varepsilon_0} \int_{\varepsilon_0}^{\varepsilon_1} \sigma d\varepsilon \tag{2.1}$$

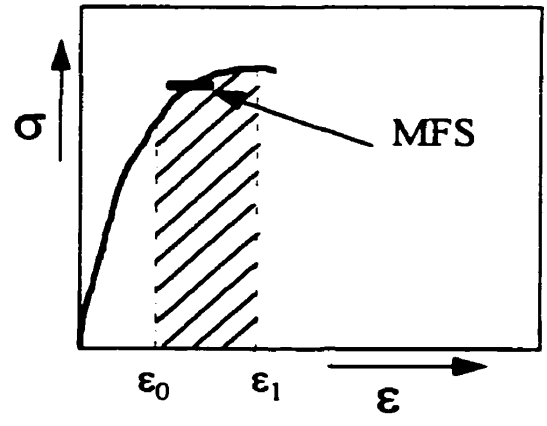

Figure 2.1 Graphical representation of the MFS.

Although the MFS calculation is fairly simple in the case of stress-strain curves, in which case numerical methods can be used for the integration, the situation is different during rolling. A "mechanical" description of the MFS is more complex than that described above, but will be required for the rolling calculations and is described below.

2.1.1-Mechanical Description of the MFS in Hot Rolling

It is not straightforward or easy to determine the flow stress in the roll gap; this is because of the complexity and inhomogeneity of the deformation. Numerical methods such as finite elements have been used, which can provide a detailed description of the strain distribution. However, this method requires long computer times and simple "mechanical" methods are desirable in most applications. The first complete and comprehensive calculation of the roll pressure distribution was described by Orowan [4]. However, due to its complexity and the need for numerical integration to describe the non-uniform deformation associated with the assumption of a variable friction coefficient, other theories have been proposed, like the one developed by Sims [5].

Sims' approach for the calculation of roll force and torque made assumptions to allow for an analytical solution of the numerical integration needed in Orowan's theory. Also, Sims considered that sticking friction occurs between the work roll and the workpiece, resulting in a simpler calculation that is widely used. Sims' calculation of the MFS in each pass requires knowledge of the strip width, thickness, work roll diameter and rolling force. The MFS equation is shown below:

$$MFS = \frac{P}{\left(\frac{2}{\sqrt{3}} w[R(H-h)]^{1/2} Q\right)} \tag{2.2}$$

where P is the roll force,
R is the roll radius,
w is the strip width,
H is the entry thickness,
h is the exit thickness, and
Q is a geometrical factor (defined below).

Note that the MFS is expressed in equivalent (von Mises) stress units and that the factor $2/\sqrt{3}$ is included to allow for plane strain.

The geometrical factor is calculated with reference to Figure 2.2, which shows the geometry of the roll gap during strip rolling.

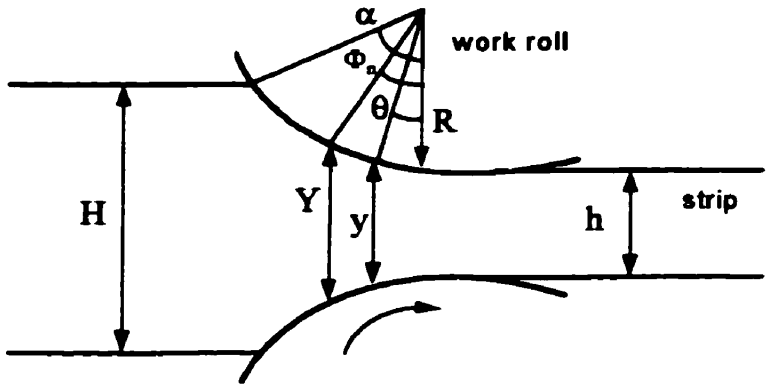

Figure 2.2 Geometry of strip/roll contact.

The normal roll pressure s and the yield strength in plane strain compression k are related from the neutral point (Φ_n) to the exit point (θ) as given by:

$$\frac{s^+}{k} = \frac{\pi}{4}\ln\frac{y}{h} + \frac{\pi}{4} + \left(\frac{R}{h}\right)^{1/2}\tan^{-1}\left[\left(\frac{R}{h}\right)^{1/2}\theta\right] \tag{2.3}$$

and from the roll gap entrance ($\theta = \alpha$) to the neutral point by,

$$\frac{s^-}{k} = \frac{\pi}{4}\ln\frac{y}{h} + \frac{\pi}{4} + \left(\frac{R}{h}\right)^{1/2}\tan^{-1}\left[\left(\frac{R}{h}\right)^{1/2}\alpha\right] - \left(\frac{R}{h}\right)^{1/2}\tan^{-1}\left[\left(\frac{R}{h}\right)^{1/2}\theta\right] \tag{2.4}$$

where θ is a generic angle in the working zone. For small angles, the differences between normal and vertical roll pressures are negligible. Under this assumption, the neutral point angle, Φ_n, can be determined by setting $s^+ = s^-$ and rearranging:

$$\Phi_n = \left(\frac{h}{R}\right)^{1/2} \cdot \tan\left[\frac{\pi}{8}\left(\frac{h}{R}\right)^{1/2} \ln(1-r) + \frac{1}{2}\tan^{-1}\left(\frac{r}{r-1}\right)^{1/2}\right] \tag{2.5}$$

where r is the reduction, defined by: r = (H-h)/H. The thickness at the neutral point is defined by:

$$Y = 2R(1-\cos\Phi_n) + h \tag{2.6}$$

and the geometric factor Q is finally defined by:

$$Q = \left(\frac{1-r}{r}\right)^{1/2}\left[\frac{\pi}{2}\tan^{-1}\left(\frac{r}{1-r}\right) - \left(\frac{R}{h}\right)^{1/2}\ln\left(\frac{Y}{h}\right) + \frac{1}{2}\left(\frac{R}{h}\right)^{1/2}\ln\left(\frac{1}{1-r}\right)\right] - \frac{\pi}{4} \tag{2.7}$$

The Sims model can also use the "elastically flattened" work roll radius, which is defined by R' according to the relation derived by Hitchcock [6]. The flattened radius R' is given by:

$$R' = R(1 + C \cdot P / w \cdot \Delta h) \tag{2.8}$$

where Δh is the height reduction defined by Δh = (H-h), P is the roll pressure, w is the strip width and C is an elastic term specified by:

$$C = \frac{16 \cdot (1-\upsilon^2)}{\pi \cdot E} \tag{2.9}$$

Here υ is Poisson's ratio and E is Young's modulus for the work roll material. The MFS can be now calculated with the aid of Equation (2.2) .

A simplification of the Sims model was proposed by Ford and Alexander [7] that is sometimes used in on-line models because of its computational simplicity. Their equation for the "mean shear yield stress" (MSYS) is shown below:

$$MSYS = \frac{P}{\left[\sqrt{R(H-h)}\right]\left[1.57 + \frac{\sqrt{R(H-h)}}{(H+h)}\right]} \tag{2.10}$$

where P is the roll force, H and h are the entry and exit thicknesses, respectively, as before, and R is the work roll radius.

Note that the Sims approach refers to the von Mises mean flow stress, while the F&A method calculates the "mean shear yield stress". The relation between the Sims von Mises and the F&A MSYS is therefore:

$$MFS_{Sims} = \sqrt{3} \cdot MSYS_{F\&A} \tag{2.11}$$

2.1.2-Experimental Formulations for the MFS

Misaka and Yoshimoto [8] derived an equation that correlates the MFS and simple process parameters such as temperature, carbon content, strain and strain rate for the hot strip rolling of C-Mn steels. The original "Misaka" MFS equation is expressed as follows:

$$\sigma_M = \exp\left(0.126 - 1.75\,[C] + 0.594\,[C]^2 + \frac{2851 + 2968\,[C] - 1120\,[C]^2}{T}\right)\varepsilon^{0.21}\,\dot{\varepsilon}^{0.13} \tag{2.12}$$

Here σ_M = the mean flow stress (in kg/mm^2), C = the carbon content (in wt%), T = the mean rolling temperature (in °C), ε = the strain, and $\dot{\varepsilon}$ = the strain rate (in s^{-1}). The equation was tested for the following ranges of variables: C: 0.05~1.20%, strain rate: 30~200 s^{-1}, temperature: 750~1200°C, and true strain up to 0.30. The Misaka equation, however, makes no allowance for the effects of other alloying elements as well as for the occurrence of dynamic recrystallization during hot rolling. It is based on a "power law", and so calls for continuously higher MFS values with decreasing temperature and increasing strain, strain rate and carbon content. Also, the use of Misaka's equation assumes that full softening takes place between passes.

Misaka's equation can be converted to express the MFS in MPa units by inserting a multiplier C = 9.8 before the exponential.

Shida [9] derived a similar relation for the MFS using 8 grades of C-Mn steel. The equation was tested for the following experimental range: C: 0.01~0.8%, strain

rate: 0.2~30 s^{-1}, temperature: 650~1200°C, and true strain up to 0.60. This equation is considered to be valid for both the austenite and ferrite phases:

$$K_f = K\left[1.3\cdot\left(\frac{\varepsilon}{0.2}\right)^n - 0.3\cdot\left(\frac{\varepsilon}{0.2}\right)\right]\cdot\left(\frac{\dot{\varepsilon}}{10}\right)^m \qquad (2.13)$$

Here, the parameters K, m and n are factors that depend on the temperature and carbon content, in an approach similar to that of Misaka and Yoshimoto.

Biglou et al. [10] developed an MFS equation from torsion tests for a steel containing 0.07%C-1.30%Mn-0.076%Nb-0.24%Ti. Here, the stress, expressed in MPa, is solely a function of the absolute temperature, T:

$$MFS = 166.6 + 391.2\cdot\left(\frac{1000}{T}\right) \qquad (2.14)$$

The above equation was derived under conditions of full softening between passes and, as temperature is the only variable, the use of this equation is only valid under very specific conditions.

Karjalainen et al. [11] derived another MFS equation (expressed in MPa) from torsion tests for steels containing C: 0.05-0.9%, Mn: 1.20-1.57%, Nb: 0.011-0.046%, Ti: 0.001-0.142%, V: 0-0.082%, Ni: 0.03-0.7%:

$$MFS = -225 + \frac{380000}{T} \qquad (2.15)$$

As in the previous case, there is no allowance for any parameter other than the temperature.

2.2-Metallurgical Phenomena Taking Place During Hot Working

The physical metallurgy of hot working has been a major topic of study of various research groups around the world for the past 40 years. In the following

sections, the equations used to describe recrystallization, grain growth and precipitation will be reviewed, and the aspects of interest to the present work will be highlighted.

2.2.1-Static and Dynamic Recovery

Recovery is the softening mechanism that releases strain energy by the annihilation and rearrangement of dislocations and other crystalline defects such as vacancies and interstitials. There is no grain boundary motion involved. However, the subgrain boundaries are sharpened. Dynamic recovery is basically the same process, however, it occurs *during* deformation. The rate of annihilation of dislocations depends on the stacking fault energy (SFE) of the metal. Usually, the dislocations are decomposed into partials. In order to move by the climb and cross-slip mechanisms, the partials must be recombined. Therefore, in high SFE metals, where the partial dislocations are already close to each other, the rate of recovery is high, leading to the formation of cellular distributions of dislocations. The opposite occurs in low SFE metals, leading to planar dislocation distributions after deformation.

During the recrystallization of high SFE metals, rapid recovery in the unrecrystallized regions leads to a decrease in the driving force (stored energy of the dislocations) for grain boundary motion. This effect softens the material and can even stop the grain boundary migration (i.e. recrystallization) if the driving force is sufficiently reduced. Considering austenite as a low or medium SFE phase, recovery processes (both static and dynamic) are neglected here. In this way, it is assumed that fractional softening and recrystallized fraction are numerically the same.

2.2.2-Static Recrystallization (SRX) Kinetics

Static recrystallization (SRX) is a softening mechanism that occurs commonly during the hot working of steels; this process involves the migration of high angle boundaries, which annihilates dislocations and releases stored energy in this way. In a HSM, it frequently occurs between passes, after the deformation and during the interpass time. The driving force is the energy stored previously in the material in the form of dislocations. The latter depends on both the strain rate and the strain applied during the pass. As SRX is a nucleation and growth transformation, its kinetics follow the Avrami [12] - Johnson-Mehl [13] - Kolmogorov [14] type of equation, as given below:

$$X = 1 - \exp(-b \cdot t^n) \tag{2.16}$$

where X is the fraction transformed,
b is a constant that depends on the nucleation and growth rates,
t is the time, and
n is the time exponent.

The above equation represents a sigmoidal curve and describes a nucleation and growth transformation taking place under isothermal conditions. For the present purposes, Eq. 2.16 can be rewritten as a function of the time required to attain a certain level of softening or of recrystallization. This includes the effects of temperature, strain, strain rate and initial grain size indirectly:

$$X = 1 - \exp\left[-A \cdot (t / t_f)^n\right] \tag{2.17}$$

where t_f is the time to reach a given fractional softening f,
A is defined by -ln (1-f), and
n is the time exponent.

The time for a given amount of fractional softening, f, is usually specified by an equation that depends on the temperature (T) and strain rate ($\dot{\varepsilon}$) via the Zener-Hollomon parameter (Z), as well as on the strain (ε), initial grain size (d_0) and activation energy for recrystallization (Q_{rex}).

Investigations carried out in the past decades have led to fairly full descriptions of the kinetics of SRX [15-23]. The general form of these equations is shown below.

$$t_f = B \cdot \varepsilon^{-p} \cdot d_0^{\,q} \cdot Z^r \exp\left(\frac{Q_{rex}}{RT}\right) \tag{2.18}$$

Here R is the gas constant, given by 8.31 [J.mol/K]
Z is defined by: $Z = \dot{\varepsilon} \cdot \exp\left(\frac{Q_{def}}{RT}\right)$
Q_{def} is the activation energy for deformation
B, p, q and r are material-dependent constants.

The strain stored in the material represents the main driving force for recrystallization and the strain exponent is therefore negative, usually between -2 and -4. The effect of decreasing the grain size is to decrease t_f due to the higher density of nucleation sites; there is also a contribution from the deformation constraints imposed by fine-grained microstructures, which lead to slightly higher rates of work hardening. The grain size exponent, q, is usually about 2; however, in a recent study [24], an exponent of 1.7 was proposed for a 0.055%Nb grade, on the basis of results from three different mechanical test methods. According to Sellars [15], the activation energy for recrystallization does not depend on the strain. Furthermore, not all the equations published in the literature include a dependence on strain rate. Nevertheless, the higher the strain rate, the finer the subgrains that are produced; this will result in higher dislocation densities and therefore higher driving forces. However, this effect is small and the exponent r generally lies between 0 and -0.2.

Several authors have fitted equations for X and $t_{0.5}$ to data obtained on various materials. In this work, the ones determined on plain C-Mn steels and Nb microalloyed steels are considered. In Table 2.1, there is a list of the equations available in the literature that describe the kinetics of static recrystallization.

Table 2.1 Equations available to describe SRX kinetics.

Author	Steel	Equation
Sellars [16]	C-Mn	$X = 1 - \exp[-0.693(t/t_{0.5})^2]$ (2.19) $t_{0.5}^{SRX} = 2.5 \times 10^{-19} \varepsilon^{-4} d_0^2 \exp\left(\frac{300\,000}{RT}\right)$ (2.20)
Yada and Senuma [17,18]	C-Mn	$X = 1 - \exp[-0.693(t/t_{0.5})^2]$ (2.21) $t_{0.5}^{SRX} = 2.2 \times 10^{-12} \cdot \varepsilon^{-2} \cdot \dot{\varepsilon}^{-0.2} \cdot S_v^{-0.5} \exp\left(\frac{30\,000}{T}\right)$ (2.22) $S_v = \frac{24}{\pi d_0}[0.491\exp(\varepsilon) + 0.155\exp(-\varepsilon) + 0.1433\exp(-3\varepsilon)]$ (2.23)

Williams et al. [19]	Nb-Ti	$X = 1 - \exp[-0.288(t / t_{0.25})]$ (2.24) Above 990°C: $t_{0.25}^{SRX} = 1.5 \times 10^{-18} d_0^2 (\varepsilon - 0.025)^{-2.8} \exp(30\,[Nb]) \exp\left(\frac{300\,000}{RT}\right)$ (2.25) Below 990°C: $t_{0.25}^{SRX} = 10^{-54} d_0^2 (\varepsilon - 0.025)^{-2.8} \exp(30\,[Nb]) \exp\left(\frac{885\,000}{RT}\right)$ (2.26)
Hodgson et al. [20,21]	C-Mn Nb	$X = 1 - \exp[-0.693(t / t_{0.5})]$ (2.27) $t_{0.5}^{SRX} = 2.3 \times 10^{-15} \varepsilon^{-2.5} d_0^2 \exp\left(\frac{230\,000}{RT}\right)$ (2.28) $t_{0.5}^{SRX} = (-5.24 + 550\,[Nb]) \times 10^{-18} \varepsilon^{(-4.0+77[Nb])} d_0^2 \exp(330000 / RT)$ (2.29)
Roberts et al. [23]	C-Mn	$X = 1 - \exp[-0.693(t / t_{0.5})^{1.7}]$ (2.30) $t_{0.5}^{SRX} = 5.1 \times 10^{-21} \varepsilon^{-4} d_0^2 \exp\left(\frac{330\,000}{RT}\right)$ (2.31)
Laasraoui and Jonas [25]	Nb	$X = 1 - \exp[-0.69(t / t_{0.5})]$ (2.32) $t_{0.5} = 1.27 \times 10^{-18}\ \varepsilon^{-3.81}\ \dot{\varepsilon}^{-0.36} \exp(404000 / RT)$ (2.33)

The constants in the above equations have somewhat different values, probably because different test methods and materials were used. Nevertheless, the equations have the same basic form.

2.2.3-Statically Recrystallized Grain Size

The grain sizes produced after full SRX are a function of the prior strain and the initial grain size. The equations describing the recrystallized grain size are generically given by:

$$d_{rex} = D \cdot d_0^{\,v} \cdot \varepsilon^{-z} \tag{2.34}$$

where D, v and z are constants. Note that the final grain size increases with the initial grain size and decreases with increasing applied strain. According to Sellars [15], the constant z tends to be higher for C-Mn than for Nb steels. A small initial grain size leads to a higher dislocation density. Consequently, the nucleation rate is increased, resulting in finer recrystallized grain sizes. Table 2.2 displays some relations available in the literature for the calculation of statically recrystallized grain size.

Some of the above equations are applied to the C-Mn grades and the results are plotted in Figure 2.3 for comparison purposes. They converge to various constant values; here, initially d_0 = 60μm and strain increments of 0.3 are applied at a strain rate of 1 s^{-1}.

Table 2.2 Equations describing the final grain size after complete SRX.

Author	Steel	Equation
Hodgson et al. [20,21]	C-Mn	$d_{SRX} = 343 \cdot d_0^{\,0.4} \cdot \varepsilon^{-0.5} \exp\left(\frac{-45000}{RT}\right)$ (2.35)
Sellars [15,16]	C-Mn	$d_{SRX} = 0.5 \cdot d_0^{\,0.67} \cdot \varepsilon^{-1.0}$ (2.36)
	Nb	$d_{SRX} = 1.1 \cdot d_0^{\,0.67} \cdot \varepsilon^{-0.67}$ (T > 950°C) (2.37)

Roberts et al. [23]	C-Mn	$d_{SRX} = 6.2 + 55.7 \cdot d_0^{0.5} \cdot \varepsilon^{-0.65}\left[\exp\left(\frac{-350000}{RT}\right)\right]^{-0.1}$ (2.38)
	Ti-V	$d_{SRX} = 4.3 + 195.7 \cdot d_0^{0.15} \cdot \varepsilon^{-0.57}\left[\exp\left(\frac{-350000}{RT}\right)\right]^{-0.11}$ (2.39)
Choquet et al. [22]	C-Mn	$d_{SRX} = 45\exp\left(\frac{-24980}{RT}\right)\varepsilon^{-0.6} d_0^{0.374}\dot{\varepsilon}^{-0.1}$ (2.40)
	Nb	$d_{SRX} = 472\exp\left(\frac{-48597}{RT}\right)\varepsilon^{-0.7} d_0^{0.277}\dot{\varepsilon}^{-0.1}$ (2.41)
Yada et al. [17,18]	C-Mn	$d_{SRX} = \frac{5}{(S_v \cdot \varepsilon)^{0.6}}$ (2.42) $S_v = \frac{24}{\pi d_0}[0.491\exp(\varepsilon) + 0.155\exp(-\varepsilon) + 0.1433\exp(-3\varepsilon)]$ (2.43)

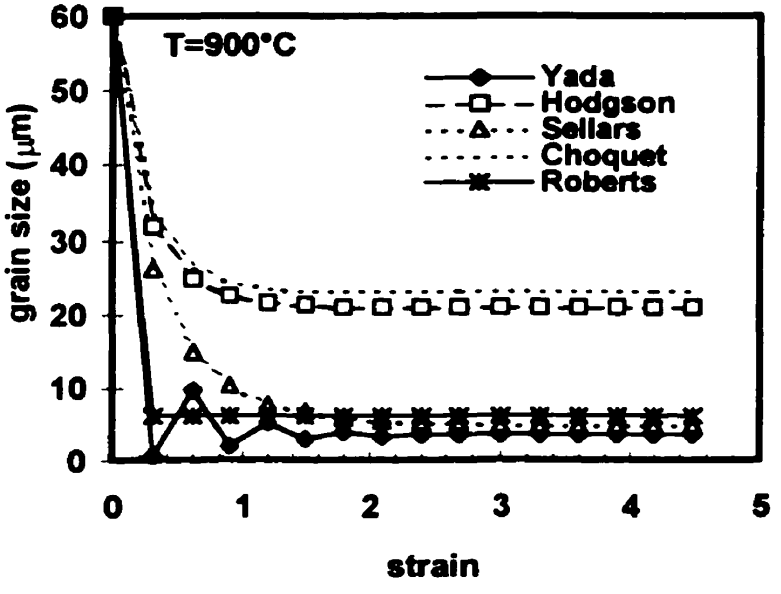

Figure 2.3 Comparison of statically recrystallized grain size models for C-Mn steels at 900°C, pass strain of 0.3 and strain rate of $1s^{-1}$.

The two temperature-independent equations, 2.36 and 2.42 converge to somewhat finer grain sizes, of about 5μm. For the temperature-dependent equations, the final grain size converges to about 20μm at 900°C after several passes. Decreasing the temperature to 800°C, the temperature dependent equations converge to about 12μm, decreasing the difference. Global convergence occurs at 650°C; however, this temperature is too low for hot strip rolling. Finally, convergence always occurs even though there can be large differences in the initial grain size [26].

2.2.4-Dynamic Recrystallization (DRX)

DRX occurs during deformation when the applied strain exceeds the critical strain, ε_c, for the initiation of DRX. At high strain rates, the work hardening is "balanced" by the rapid DRX softening that takes place, causing a peak (at a strain ε_p), followed by a drop in stress. After a certain time (strain), the generation and annihilation of dislocations reach an equilibrium and the material can be deformed without any further increase or decrease in stress; this is referred to as attaining the steady state stress. These phenomena are exemplified by the stress-strain curve shown in Figure 2.4:

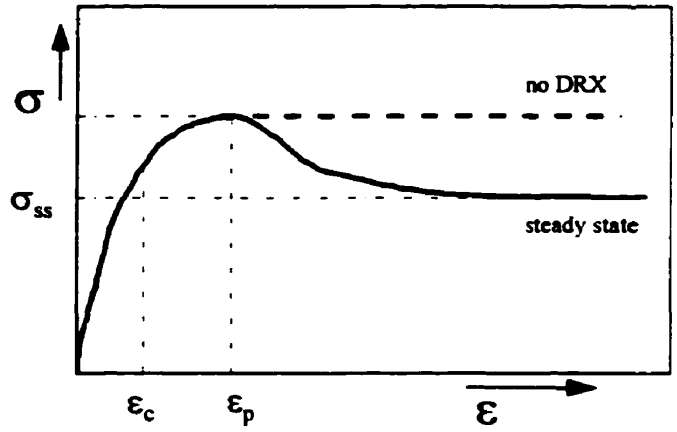

Figure 2.4 Stress-strain curve showing the effect during hot working of DRX at a high strain rate.

The occurrence of DRX causes large scale and rapid softening. When the strain rate is reduced sufficiently, the stress-strain curve generally displays a "cyclic" or multiple peak behavior. The DRX kinetics under both conditions were modeled by

Luton and Sellars [27]. In a more recent investigation, Sakai and Jonas [28] showed that single peak behavior is associated with grain refinement and multiple peak behavior with grain coarsening.

Critical Strain for the Initiation of DRX

Knowledge of the critical strain for the initiation of dynamic recrystallization (DRX) is a requirement for prediction of the operating static softening mechanism during a given hot working interpass period. In this way, the rapid softening and intense grain refinement caused by DRX can considerably modify the work hardening, and therefore the load behavior in the following pass.

It is useful to express the critical strain for DRX (ε_c) as a function of the peak strain (ε_p), as determined from a stress-strain curve. This is because several equations are available to specify the peak strain as a function of the initial grain size, temperature and strain rate for Nb steels. The $\varepsilon_c/\varepsilon_p$ ratio often lies between 0.67-0.86 [15] and is generally taken as 0.8 for plain C-Mn steels. Collinson et al. [29] correlated the effect of carbon on the critical strain in plain C-Mn steels. They concluded that the addition of C can decrease the $\varepsilon_c/\varepsilon_p$ ratio. Previous workers have reported values for Nb steels as low as 0.65 [30,31].

2.2.5-DRX Kinetics

Compared to SRX, very few descriptions of DRX kinetics are available in the literature. Nevertheless, DRX kinetics can be described by an AJMK type of equation in which the kinetics are considerably faster than in the case of SRX [1]. Table 2.3 displays some equations available in the literature that describe the DRX kinetics.

Table 2.3 Models describing the kinetics of DRX

Author	Steel	Equation
Hodgson et al. [20,21]	C-Mn	$X = 1 - \exp[-0.693(t/t_{0.5})^{1.5}]$ (2.44)
		$t_{0.5}^{DRX} = 1.1 \cdot Z^{-0.8} \exp\left(\frac{230\,000}{RT}\right)$ (2.45)

Sellars [15,16]	C-Mn	$X = 1 - \exp[-0.693(t / t_{0.5})^2]$	(2.46)
		$t_{0.5}^{DRX} = 1.06 \cdot Z^{-0.6} \exp\left(\frac{300\,000}{RT}\right)$	(2.47)
Yada [18]	C-Mn	$X = 1 - \exp\left[-0.693\left(\frac{\varepsilon - \varepsilon_c}{\varepsilon_{0.5}}\right)^2\right]$	(2.48)
		$\varepsilon_c = 4.76 \times 10^{-4} \exp(8000 / T)$	(2.49)
		$\varepsilon_{0.5} = 1.144 \times 10^{-5}\ d_0^{0.28}\ \dot{\varepsilon}^{0.05} \exp(6420 / T)$	(2.50)

2.2.6-Metadynamic Recrystallization (MDRX)

Metadynamic recrystallization (MDRX) basically results from continued growth after unloading of the nuclei formed during deformation. This situation is generally observed in hot deformation schedules when the reductions applied do not reach the steady-state regime, but nevertheless attain or exceed the peak strain. Once deformation is interrupted, the nuclei formed dynamically grow statically during the interpass time. Like DRX, MDRX is known to involve rapid kinetics, sometimes attributed to the absence of the incubation period normally required for nucleation. Table 2.4 lists some models for the kinetics of MDRX.

Table 2.4 Models describing the kinetics of MDRX

Hodgson [32]	Nb	$X = 1 - \exp[-0.693(t / t_{0.5})^{1.1}]$	(2.51)
		$t_{0.5}^{MDRX} = 1.1 Z^{-0.8} \exp(230000 / RT)$	(2.52)
Roucoules [31]	Nb	$X = 1 - \exp[-0.693(t / t_{0.5})\ ]$	(2.53)
		$t_{0.5}^{MDRX} = 4.42 \times 10^{-7} \dot{\varepsilon}^{(-0.59)} \exp(153000 / RT)$	(2.54)
Hodgson [33]	Nb and C-Mn (literature)	$X = 1 - \exp[-0.693(t / t_{0.5})^{1.1}]$	(2.55)
		$t_{0.5}^{MDRX} = 0.4\ Z^{-0.8} \exp(240000 / RT)$	(2.56)

As first detected by Djaic and Jonas [34], the kinetics of MDRX do not depend on the strain, but only on the strain rate, as confirmed later by various investigators [15,20,21,30,31]. Higher strain rates produce higher dislocation densities, and therefore higher driving forces, when compared to lower strain rates. By contrast, little dependence on temperature, alloying and microalloying elements has been observed [32]. In a recent study [35], it has also been shown that the addition of Mo, Nb or Ti has little effect on the MDRX kinetics. However, clear physical reasons why MDRX has a strong dependence on the strain rate and a weak dependence on the other parameters have not been reported in the literature.

The grain sizes produced by MDRX are larger than the ones associated with DRX after deformation at the same strain rate [33]. Some expressions for the grain size (in μm) produced after MDRX are presented in Table 2.5.

Table 2.5 Equations describing the final grain size after complete MDRX.

Author	Steel	Equation
Hodgson et al. [20,21]	C-Mn	$d_{MDRX} = 2.6 \times 10^4 \cdot Z^{-0.23}$ (2.57)
Roucoules [31]	Nb	$d_{MDRX} = 1370 \times \varepsilon^{-0.13} \exp\left(\frac{-45000}{RT}\right)$ (2.58)
Hodgson [33]	Nb and C-Mn (literature)	$d_{MDRX} = 6.8 \times 10^4 Z^{-0.27}$ (2.59)

2.2.7-Grain Growth

After complete recrystallization, grain growth takes place. The energy stored in the grain boundaries is the driving force and high temperatures produce kinetic conditions that favor rapid diffusion across the boundaries. In this study, the term **grain growth** is used to describe the mechanisms that reduce grain boundary area, resulting in larger grain sizes. This is what occurs after full recrystallization when a sample is held at a high temperature. The expression "grain coarsening" (as opposed to

"grain refinement") will be used to describe the relation between the initial and final grain sizes after a process, such as DRX, SRX, and so on, has taken place.

The general equation of grain growth is given by:

$$d^m = d_0^m + k \cdot t \cdot \exp\left(\frac{-Q_{gg}}{RT}\right) \tag{2.60}$$

where m is the growth exponent,

R is the gas constant,

k is a constant, and

Q_{gg} is the activation energy for grain growth.

Some of the grain growth models are concerned with the grain sizes present after the occurrence of at least 95% of recrystallization [36]. This condition is selected because, in practical terms, growth can only take place in fully recrystallized regions (even though such regions can form well before the last regions to recrystallize).

The interpass times seems to play an important role in the grain growth equations [21]. Usually, during the first second, grain growth is parabolic (m = 2); after about 1s of this rapid growth, the rate decreases (m = 7). A 'pragmatic' solution to this problem is to adopt different equations for times shorter or longer than 1s [21]. This effect is especially critical when dealing with plain C-Mn steels, where the grain growth kinetics are very rapid.

These models suggest that different grain growth rates apply following SRX or DRX [21,37]. SRX requires nucleation, which means that the 'freshly' formed grains are small and have a fast growth rate. During MDRX, which does not require nucleation, the recrystallized grains start from a certain size. The grains produced by MDRX are finer and fully formed during the very beginning of the interpass time. The rapid MDRX softening kinetics as well as the difference in the recrystallized grain size (as compared to SRX) require a different description for their growth. Thus, the different kinetic equations may correspond to different overall grain growth processes [37]. Different descriptions for the kinetics of grain growth after SRX and MDRX are given in a grain size model for the rod rolling of C-Mn steels [36]. Figure 2.5 displays

the effects discussed above. The kinetics of grain growth are represented by the power laws listed in Table 2.6.

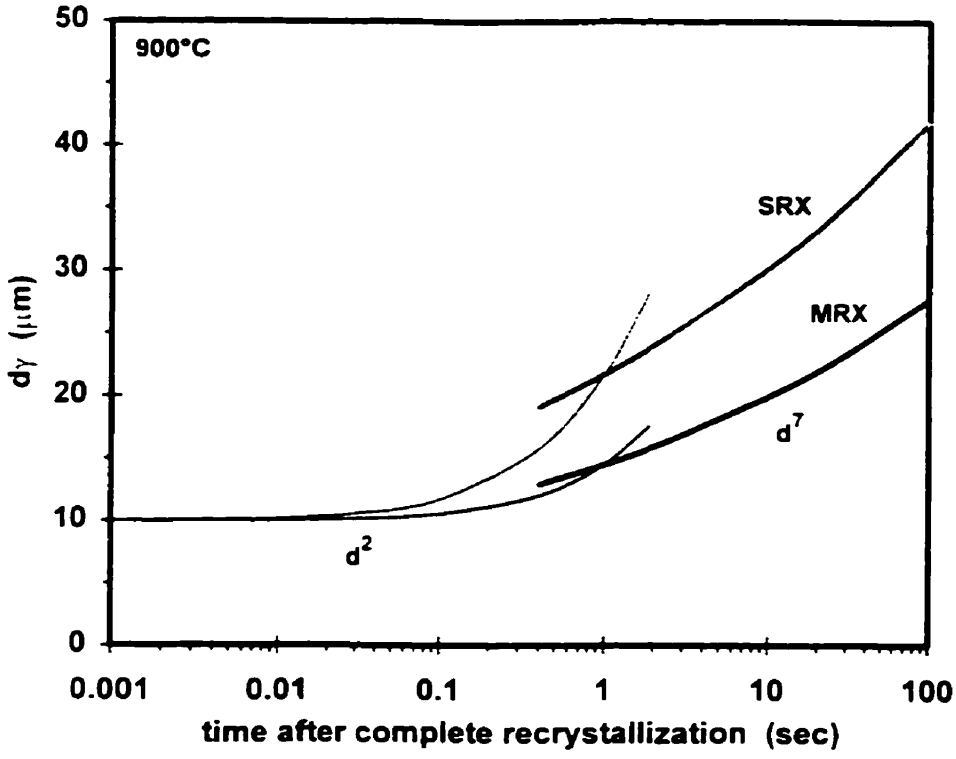

Figure 2.5 Austenite grain growth behavior after either full SRX or full MDRX. The transition from parabolic to seventh order growth occurs at 1s [36].

Table 2.6 Austenite grain growth models. t_{ip} is the interpass time.

Author	Steel	Equation
Hodgson et al. [21,36,37]	SRX	$d^2 = d_{SRX}^2 + 4.0\times10^7 (t_{ip} - 4.32t_{0.5}) \exp\left(\frac{-113\,000}{RT}\right)$ (2.61)
	If t_{ip}<1s	
	MDRX	$d^2 = d_{MDRX}^2 + 1.2\times10^7 (t_{ip} - 2.65t_{0.5}) \exp\left(\frac{-113\,000}{RT}\right)$ (2.62)
	C-Mn	
	SRX	$d^7 = d_{SRX}^7 + 1.5\times10^{27} (t_{ip} - 4.32t_{0.5}) \exp\left(\frac{-400\,000}{RT}\right)$ (2.63)
	If t_{ip}>1s	
	MDRX	$d^7 = d_{MDRX}^7 + 8.2\times10^{25} (t_{ip} - 2.65t_{0.5}) \exp\left(\frac{-400\,000}{RT}\right)$ (2.64)
Roberts et al. [23]	C-Mn	$d^2 = {d_0}^2 + \exp(6.6 - 6200/T)\cdot t_{ip}$ (2.65)
Senuma and Yada [17]	C-Mn	$d^2 = d_0^2 + 1.44\times10^{12}\ t\ \exp\left(\frac{32100}{T}\right)$ (2.66)
Sellars and Whiteman [38]	C-Mn T>1000°C	$d^{10} = d_0^{10} + 3.87\times10^{32}\ t\ \exp\left(\frac{400000}{RT}\right)$ (2.67)
	T<1000°C	$d^{10} = d_0^{10} + 5.02\times10^{53}\ t\ \exp\left(\frac{914000}{T}\right)$ (2.68)
Hodgson and Gibbs [20]	Nb	$d^{4.5} = d_0^{4.5} + 4.1\times10^{23} \times t_{ip} \times \exp(-435000/RT)$ (2.69)

2.2.8-Role of Nb Addition During Controlled Rolling

The addition of microalloying elements such as Al, Mo, Nb, Ti and V causes a retarding effect on austenite recrystallization. The drag force acting on a grain boundary can be either attributed to solute drag [39] or to particle pinning [40]. The most important effect is particle pinning after the strain-induced precipitation of Nb(C,N) [41]. However, in a more realistic analysis, both can occur at the same time. The balance between driving forces (the stored energy of dislocations) and dragging forces (particle pinning and solute drag) will decide whether recrystallization can occur or not. Some models are available for the calculation of these forces, such as Zener's model for particle pinning on moving boundaries [42]. The only exception is solute drag. A rough approximation, which considers solute atoms as particles, is not strictly correct because the atoms can move by diffusion. Also, calculations using Zener's equation lead to unrealistically high values of the drag force because of the atomic dimensions involved.

The mathematical description of solute drag is also very complex, as it must account for [43]: (*i*) the interaction energy between solute atoms and grain boundaries, something that is difficult to measure or to calculate; and (*ii*) the observation that solute atoms tend to follow moving boundaries by diffusion. Slowly moving boundaries (e.g. grain growth) do not experience much drag. Rapidly moving boundaries are also subjected to a reduced effect. The maximum retarding effect occurs at intermediate boundary velocities, such as those associated with recrystallization.

Niobium is the most effective microalloying element at hot strip rolling temperatures, that is, in the range 1100 to 850°C. This is because it influences recrystallization and grain growth as well as precipitation in both austenite and ferrite. These effects are present up to 1200°C and beyond, when Nb compounds are almost completely dissolved for most compositions of microalloyed steels [44,45].

2.2.9-Precipitation of Nb Carbonitrides during Hot Rolling

The effects of Nb on the behavior of microalloyed steels are well known at several stages of processing, especially roughing, finishing and coiling. The retardation of recrystallization, either by solid solution or by precipitation effects, can completely change the behavior of a steel during strip rolling. We consider here that Nb in solid solution retards the kinetics of static and metadynamic recrystallization and that Nb

precipitation essentially stops any further recrystallization. Although the precipitates can coarsen at high temperatures and therefore decrease their effectiveness, such coalescence and growth are considered to have relatively slow kinetics during the short times that the strip remains in the HSM.

The opposite effects of Mn and Si on precipitation should also be taken into account. The influence of Mn and Si on the solubility of NbC and NbN were studied by Koyama et al. [46,47]; they showed that Mn increases the solubility of NbC and NbN in austenite. On the other hand, the opposite effect of Si, which decreases the solubility of these compounds in austenite, was also detected. Mn is known for decreasing the precipitation rate of Nb(C,N), as reported by Akben et al. [48]. The effect of Si on the precipitation kinetics is expected to be the opposite, accelerating the rate of precipitation; this is based on the view that Mn and Si have opposite effects on the solubility of Nb(C,N).

Two quite contrasting precipitation models are available in the literature, one due to Dutta and Sellars [49] for Nb carbonitride precipitation and the other proposed by Liu and Jonas [50], derived to describe the precipitation of Ti carbonitride.

The DS model has the advantage that it is easy to apply on the basis of data obtained in the laboratory or an industrial process. It was derived using nucleation theory and data obtained from the literature, from a variety of sources and, sometimes, on steels with different base chemistries (e.g. Mn and Si contents). Therefore, some "tuning" is necessary for its practical use. Adaptations of this model were performed in this investigation, in order to improve the fit to experimental data [51,52].

The DS model describes the isothermal precipitation of Nb(C,N) from supersaturated austenite. The time for 5% precipitation is obtained from the relation below, which specifies the dependence of the precipitation start time, t_{ps} in Nb steels on process variables such as the strain, strain rate, and temperature. It also includes the Nb concentration as well as the supersaturation ratio, K_S. The latter, which determines the "driving force" for precipitation, is expressed as:

$$K_S = \frac{10^{-6770/T_{RH}+2.26}}{10^{-6770/T_{Pass}+2.26}} \tag{2.70}$$

where the parameters T_{RH} and T_{Pass} are the absolute reheat and pass temperatures. The solubility products that apply to the reheat and pass temperatures are taken from the relation derived by Irvine et al. [53]. The K_S term expresses the ratio between the

amounts of Nb and C in solution at the reheat and pass temperatures, under equilibrium conditions. The final equation is:

$$t_{ps} = A\,[Nb]^{-1}\varepsilon^{-1}\,Z^{-0.5}\exp\frac{270000}{RT}\exp\frac{B}{T^3[\ln(K_s)]^2} \qquad (2.71)$$

The constants $A = 3\times10^{-6}$ and $B = 2.5\times10^{10}$ (K^3) were found by fitting to published data. The constant B is basically a product of constants and does not seem to be critical. However, the constant A depends on the number of nuclei per unit volume, which is greatly affected by the strain and temperature. The effect of Mn addition in retarding the precipitation kinetics [48] was not accounted for in this model and therefore it usually needs some fine tuning in order to predict the precipitation start times during hot strip rolling with accuracy.

The LJ model has a clear physical and thermodynamic background and was derived to model the precipitation kinetics of a Ti-microalloyed austenite. The theoretical model was fitted to experimental precipitation data obtained using the stress-relaxation technique. Later, Park and Jonas [54] rewrote the LJ model and applied it to a Nb-microalloyed austenite. The approach of Park and Jonas led to the following prediction of the Nb(C,N) precipitation start time, P_s:

$$P_s = \frac{N_c \cdot a^3_{Nb(C,N)}}{D_0 \cdot \rho}\left(X_{Nb}\right)^{-1}\exp\left(\frac{Q}{RT}\right)\exp\left(\frac{\Delta G^*}{kT}\right) \qquad (2.72)$$

Here N_c is the critical number of nuclei per unit volume,
a is the lattice parameter of Nb(C,N),
D_0 is the pre-exponential for the diffusion of Nb in austenite,
ρ is the dislocation density,
X_{Nb} is the concentration of Nb in solution,
Q is the activation energy for the diffusion of Nb in austenite,
R is the gas constant,
k is the Boltzmann constant, and
ΔG^* is the critical activation free energy for nucleation.

ΔG^* is in turn given by:

$$\Delta G^* = \frac{16\pi(\xi\gamma)^3}{3(\Delta G_{chem} + \Delta G_\varepsilon)^2} \tag{2.73}$$

where ΔG_ε is the volume strain energy, γ is the particle/matrix interfacial energy, ξ is a γ modifier (between 0 and 1), and the chemical free energy, ΔG_{chem}, is given by:

$$\Delta G_{chem} = \frac{RT}{2\Omega}\left[\ln\left(\frac{X^e_{Nb}}{X^0_{Nb}}\right) + y\ln\left(\frac{X^e_C}{X^0_C}\right) + (1-y)\ln\left(\frac{X^e_N}{X^0_N}\right)\right] \tag{2.74}$$

Here Ω is the molar volume of precipitate,
y is the volumetric ratio of NbC in Nb(C,N),
X^e is the equilibrium concentration of Nb, C or N in the steel, and
X^o is the overall concentration of Nb, C or N in the steel.

Park and Jonas gave values for all the above parameters, evaluated using literature data, except for N_c and ρ. These parameters are listed below:

$a_{Nb(C,N)} = 4.44\times10^{-10}$ m,
$Q = 266.5$ kJ/mol,
$D_0 = 0.83$ cm^2/s,
$\gamma = 0.5$ J/m^2

Nevertheless, a good approximation for the dislocation density can be obtained from the model by Senuma and Yada [17,18,55]. Although the model was derived to calculate the dislocation density in C-Mn steels, ρ can be estimated to a first approximation for Nb steels to be:

$$\rho = \frac{10^{11}}{b}\left[1-\exp(-b\varepsilon)\right] + \rho_0\exp(-b\varepsilon) \tag{2.75}$$

where ρ_0 is the initial dislocation density, and b is given by:

$$b = 9850 \cdot \dot{\varepsilon}^{-0.315} \cdot \exp(-8000/T) \qquad (2.76)$$

For practical applications, ρ_0 can be neglected, as it is usually orders of magnitude smaller than ρ. The presence of Nb in austenite is expected to produce higher dislocation densities than are present in C-Mn steels. Some adjustment must therefore be made in order to decrease the b parameter by changing the constants in Equation (2.76).

The parameter N_c of Equation (2.72) still needs to be calculated. The option adopted by Park and Jonas was to use experimental data to fit the N_c/ρ ratio.

Although internally consistent, to be useful for practical applications, the LJ model needs the availability of accurate physical parameters. These are difficult to obtain for a wide range of steel chemistries.

2.2.10-The Additivity Rule

The application of an isothermal precipitation model to a rolling schedule carried out under continuous cooling conditions is not straightforward. Park [54,56] applied the additivity rule proposed by Scheil [57]. Additivity requires that at least one of the following conditions applies to the reaction:

(*i*) that the reaction is isokinetic, with the rate of nucleation proportional to the rate of growth,
(*ii*) that there is site saturation early in the reaction, or
(*iii*) that the reaction is nucleation-controlled.

Application of the additivity rule concept involves dividing the continuous cooling curve into a series of isothermal steps and calculating the precipitation-start time for each step. Taking t^{ip} as the interpass time after pass i, considered isothermal, and t^{ps} as the precipitation-start time calculated for the conditions of pass i, precipitation will occur when:

$$\frac{t_1^{ip}}{t_1^{ps}} + \frac{t_2^{ip}}{t_2^{ps}} + \frac{t_3^{ip}}{t_3^{ps}} + \ldots + \frac{t_n^{ip}}{t_n^{ps}} = 1 \qquad (2.77)$$

This relation can be rewritten as:

$$\sum_{i=1}^{n} \frac{t_i^{ip}}{t_i^{ps}} = 1 \qquad (2.78)$$

Considering one pass as a single isothermal step can be a good approximation for strip rolling, where the interpass times are short [58]. The approximation described above is shown graphically in Figure 2.6.

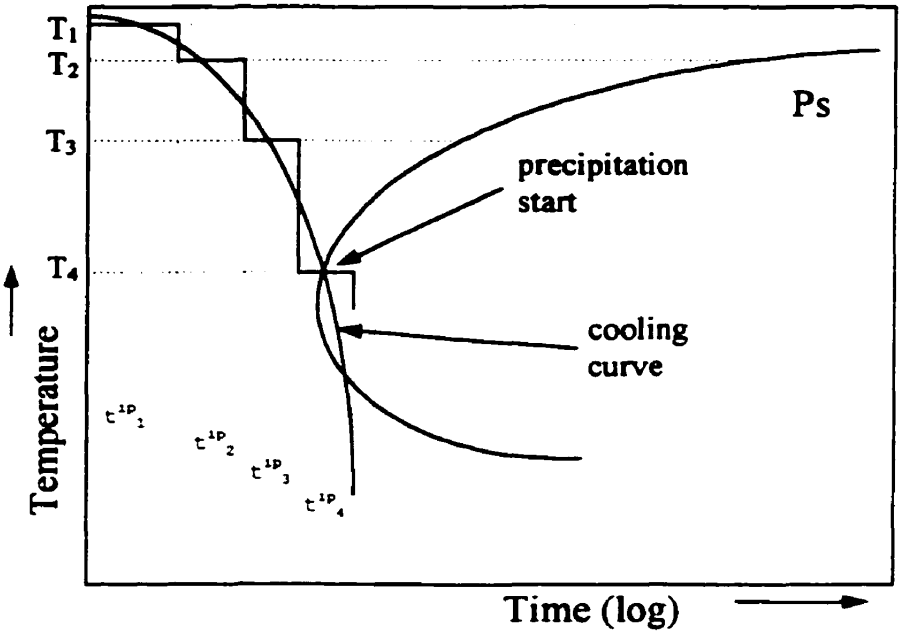

Figure 2.6 Schematic representation of the additivity rule concept [56].

Applying Park's approach to seamless tube rolling schedules, Pussegoda et al. [59] took into account the strain accumulation that occurs when calculating the t_{ps} times. They carried out their simulation by applying the addition of Eq. (2.77) to the whole schedule. Such an approach seems to be adaptable to HSM schedules as well.

2.3-The Analysis of Mean Flow Stress Curves

Prediction of the rolling force during finish rolling is an important tool for the improvement of rolling schedules by off-line simulations. The control of microstructural evolution during hot rolling is also important as it is the key factor that influences the mean flow stress (MFS) and, consequently, the rolling load. Analysis of the MFS behavior as a function of the inverse absolute temperature can lead to identification of the main microstructural changes taking place. These include SRX, DRX followed by MDRX, strain accumulation, and phase transformation. Knowledge of these events is vital for the development of accurate models for the control of hot strip mills (HSM's). Figure 2.7 illustrates these phenomena schematically in the form of an MFS versus 1/T curve for a hypothetical 5-pass schedule:

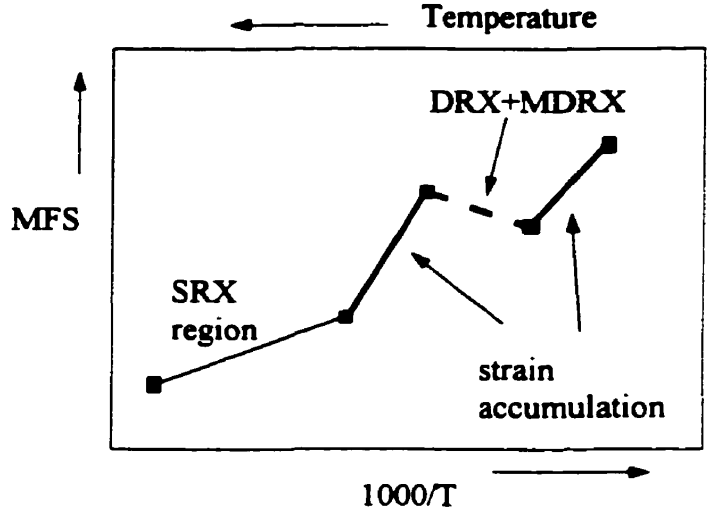

Figure 2.7. Schematic representation of the evolution of MFS as a function of the inverse absolute temperature. Each characteristic slope is associated with a distinct metallurgical phenomenon.

Starting at the first pass (high temperature side) there is a low slope region, where SRX occurs. The higher temperatures permit full softening during the interpass time. After pass 2, the lower temperature does not permit full softening, leading to the accumulation of some strain. This accumulation then leads to the onset of DRX (as there is no precipitation), which is followed by MDRX between passes 3 and 4.

The analysis of MFS curves as described above was first proposed by Boratto et al. [60] for prediction of the three critical temperatures of steel rolling (Ar3, Ar1, T_{nr}) [61,62,63]. This technique has also been used to predict the occurrence of DRX in seamless tube rolling [59,64], as well as in hot strip mills [65,66]. In this regard, special attention must be paid to the study of Sarmento and Evans [66]. They plotted MFS against the total strain, using industrial data from two hot strip mills. Their analysis of the MFS behaviors of C-Mn and Nb steels indicated that DRX takes place in the Nb steels during hot strip rolling. They observed a drop in MFS, when compared to the Misaka MFS predictions, in the final stands. For the Nb grades analyzed, the occurrence of DRX was attributed to strain accumulation that attained and then exceeded the critical strain for DRX.

2.4-Approaches to Controlled Rolling

The controlled rolling techniques currently being employed on microalloyed steels were first tested and published in the 1960's. After the first large conference in this field in 1975 [67], the use of Nb steels increased significantly. The aim of controlled rolling is to produce pancaked austenite during the finishing passes of plate or strip rolling, causing intense grain refinement after the austenite-to-ferrite transformation. The fine ferrite grain sizes produced in this way in high strength low alloy (HSLA) steels, associated with their low C contents, raise the yield strength and ductility [68-70], decrease the impact transition temperature [68,69], and improve the weldability [71,72]. The main types of controlled rolling known today are listed below.

Recrystallization Controlled Rolling (RCR)

This approach is normally used for thick plates and thick-walled seamless tubes, where the rolling loads are near the upper limit of the mill [73]. The high rolling temperatures involved (above 950°C) cause full recrystallization to take place between passes. For this purpose, Ti and V are added, allowing recrystallization to go to

completion all along the schedule, but preventing grain growth from taking place when recrystallization is complete well before the next pass. The low levels of Ti added lead to the precipitation of TiN during continuous casting. This fine dispersion prevents the occurrence of extensive grain growth. These conditions are not suited to producing the finest grain sizes; nevertheless, mill load limitations make this approach necessary in some cases. The RCR process should be employed in association with fast cooling rates in order to produce relatively fine ferritic grain sizes after transformation.

Conventional Controlled Rolling (CCR)

The main purpose of CCR is to produce a work hardened austenite after the last stand in order to increase the number of nucleation sites for the austenite-to-ferrite transformation. This leads to production of the finest ferrite grain sizes, improving mechanical properties such as the toughness and yield strength. The application of final passes in the austenite + ferrite region is sometimes also desired. In this case, the transformed ferrite will work harden and the remaining austenite will transform to undeformed ferrite [74]. Also, the ferrite present at this stage leads to lower loads in the mill because it is softer than austenite, thus compensating for the load increase associated with the decrease in temperature [75]. The fine microstructures formed in this way are responsible for yield strength and toughness improvements in the hot rolled steel.

This approach generally involves the use of high reheat temperatures so as to dissolve the microalloying elements Nb and V completely in the austenite. Then, roughing is carried out, at temperatures above the T_{nr}, allowing full softening between passes and keeping the microalloying elements in solution. Finally, finishing is applied to flatten or "pancake" the austenite grains at temperatures below the T_{nr}. The effect of the microalloying element (usually Nb) is crucial here. The solute drag acting on the moving grain boundaries and the particle pinning (after the precipitation of Nb(C,N)) retard or even prevent the occurrence of recrystallization. However, in some cases, the strain accumulation caused by this process can trigger DRX, followed by metadynamic recrystallization (MDRX), leading to rapid softening between passes. In terms of mathematical modeling, if there is no precipitation and the accumulated strain exceeds the critical strain, DRX is initiated, often causing full and fast softening. This is usually associated with unpredictable load drops in the final passes [76].

Dynamic Recrystallization Controlled Rolling (DRCR)

This type of process consists of inducing DRX in one or more passes during the rolling schedule. This can be done either by applying large single strains to the material or via strain accumulation. Both methods will allow the total strain to exceed the critical strain for the initiation of DRX. The former can be applied in the initial passes at high temperatures. The latter can occur at relatively low temperatures, in the last passes, after the strain has accumulated in the previous passes. Some of the benefits of this approach involve the intense grain refinement caused by DRX when high strain rates are employed and large strains are applied (single peak behavior in the stress-strain curve). Some DRX nucleation/growth mechanisms, such as "necklacing" (a special type of the classical "strain induced grain boundary migration" mechanism) [77-82] and the formation of "serrations" [83,84] can explain the intense grain refinement produced under high strain rate conditions. Circumstantial evidence for the occurrence of DRX in seamless tube rolling [59,64] and hot strip mills [65,66] can be found in the literature .

Figure 2.8 illustrates schematically the three controlled rolling approaches described above for a hypothetical 5-pass schedule. The conditions associated with each type of controlled rolling are displayed in Table 2.7. Knowledge of the rolling parameters and process limitations associated with each method makes possible the design of rolling schedules to fit the needs and constraints of each case.

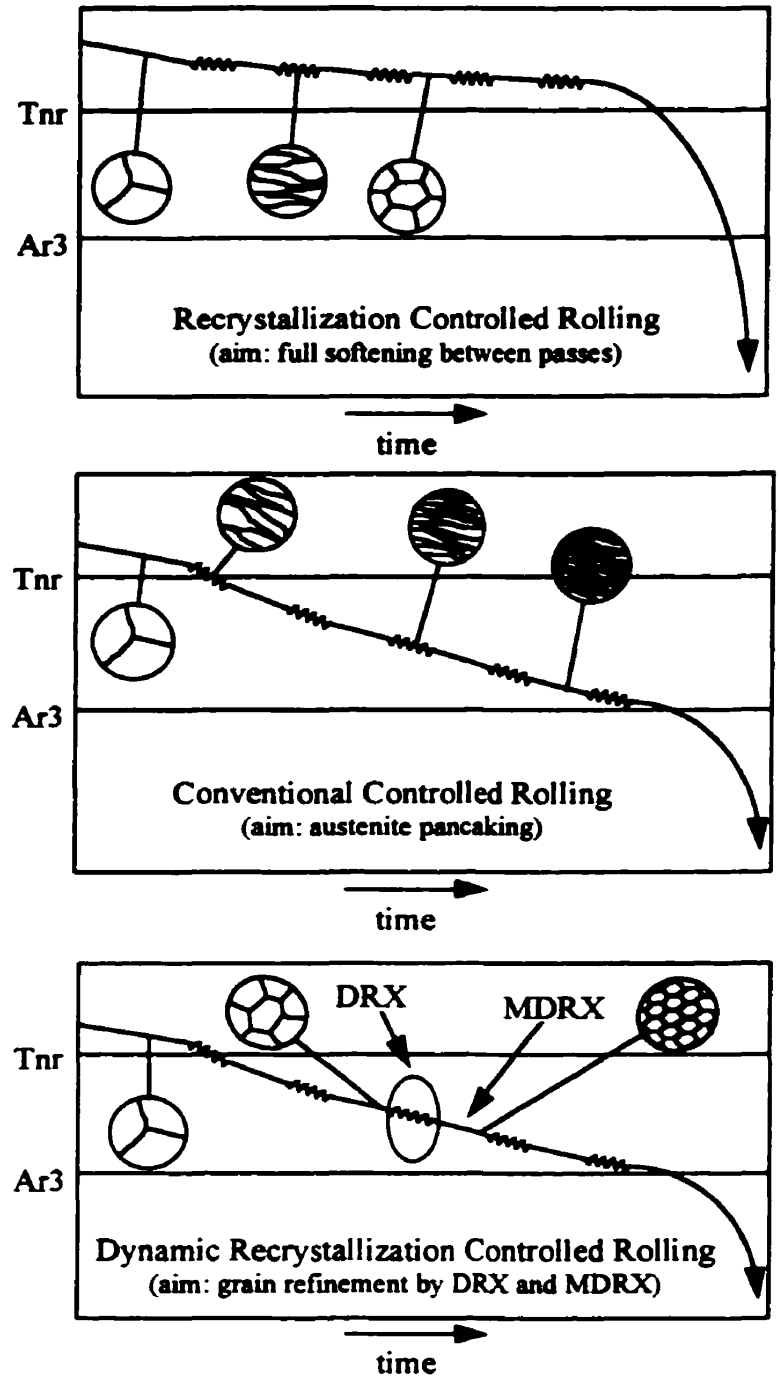

Figure 2.8. Temperature-time diagrams comparing three rolling approaches. (a) Recrystallization Controlled Rolling, (b) Conventional Controlled Rolling, (c) Dynamic Recrystallization Controlled Rolling.

Table 2.7 Mechanistic conditions pertaining to the three controlled rolling techniques [73].

Type of process	T range with respect to T_{nr}	Role of strain-induced precipitation	Relation between precipitation and recrystallization
RCR	above	absence required	SRX before precipitation
CCR	below	presence required	Precipitation before SRX or DRX
DRCR	below	absence required	No SRX and DRX before precipitation

2.5-Mathematical Models for Hot Rolling

Numerous mathematical models for use in the hot rolling of bars and flat products have been published. Some of these can predict temperatures, rolling loads and microstructures during rolling as well as mechanical properties in the final product. Some of the integrated models available in the literature will be described briefly here.

The McGill/CANMET model for long products [85-87] predicts cross-sectional temperatures during the process and the microstructural evolution during rolling, including the precipitation of Nb(C,N). To determine whether recrystallization is stopped by precipitation, the precipitation start time (t_{ps}) is compared to the recrystallization start time (t_{rex}). If $t_{ps} < t_{rex}$, recrystallization will not occur. The model also calculates the final properties of the steel after transformation and cooling and runs in a MS-Windows ™ environment, providing graphical outputs.

The "SLIMMER" model [88,89], developed by researchers at Sheffield and Leicester Universities, includes a temperature model that accounts for heat losses by convection, descaling, roll contact, and water cooling, as well as temperature increases by deformation heating and oxidation. The model also predicts rolling loads and microstructures during rolling for C-Mn and Nb steels.

The models developed by Hodgson and co-workers [1,20,21,29,32] account for microstucture evolution during rolling (SRX, DRX+MDRX and Nb(C,N) precipitation)

as well as after accelerated cooling, predicting the ferrite grain size for C-Mn and Nb microalloyed steels. A model for the rolling load is also available.

The model by Senuma and Yada [17,18,55] for C-Mn steels accounts for microstructure evolution, including SRX, DRX and phase transformation during cooling. The tensile strength (TS) in the final product can also be calculated; however, the values of the constants in the TS equation are not specified.

The model developed by Wang and Tseng at Drexel University [90] is another example of a complete model for the hot rolling of C-Mn steels. The microstructural relationships are taken from the Senuma and Yada model. The deformation model accounts for inhomogeneous deformation in the roll bite using a finite-element model and temperature calculations are performed using a finite difference model. These authors carried out complete simulations and compared their predictions with industrial data. Whether or not DRX occurred in their simulations is not clear, however, as few details are given.

The integrated model developed by Torizuka et al. [91] at the NKK Corporation, Japan, includes a clear description of the austenite-to-ferrite transformation and of the resulting mechanical properties of the steel. No allowance is made for DRX+MDRX or for the strain-induced precipitation of Nb(C,N) during rolling.

The spreadsheet model developed by Maccagno et al. [36] for microstructure evolution during rod rolling is an innovative approach for organizing several physical sub-models into a simple commercial Microsoft EXCEL™ spreadsheet program. Grain size evolution during the rod rolling of C-Mn steels was described in this way using previously developed physical models. The spreadsheet-type models have some important characteristics: (*i*) they are easy to run on personal computers; (*ii*) they are easy to modify without the need for new compilation; and (*iii*) they allow ready visualization of the pass-by-pass evolution of grain size, fractional softening and other parameters. In the above study [36], the occurrence of strain accumulation and DRX followed by MDRX was clearly characterized.

Siwecki [92] developed a model for the recrystallization controlled rolling of Ti-V-Nb steels. In his study, equations describing the kinetics of static recrystallization and the statically recrystallized grain size were derived. The model also includes equations to predict the ferrite grain size after transformation. The addition of Ti was fundamental for preventing grain growth after SRX, permitting some austenite grain refinement in RCR.

Using laboratory hot rolling experiments, Namba et al. [93] developed a model for through-thickness microstructure prediction, taking into account the effects of both SRX and DRX. With the aid of compression tests, the authors also derived equations that describe the microstructural evolution. However, the model displays discrepancies in the grain size distributions after large rolling reductions. These differences were attributed to the occurrence of DRX.

Various other microstructure models that are concerned with the entire or with specific sections of the process are available in the literature. However, at this point, we will turn our attention to models that work directly with industrial data. This permits the deformation conditions, especially the strain rates, to differ substantially from those of laboratory torsion simulations [94]. With the aid of this approach, it will be easier to affirm whether or not DRX+MDRX actually occur in hot strip rolling and why.

Chapter 3 - Experimental Materials and Methods

The present work combines the use of models developed from hot torsion test data and from the analysis of industrial mill logs. Various materials were tested; these were divided into 3 groups: Nb microalloyed (group A), multiply-alloyed (group B), and plain C-Mn (group C). Tables 3.1 and 3.2 list the grades studied here. In group A (Table 3.1), some steel chemistries have a "low Si" equivalent, with the same base composition (e.g. AD5, AD6 and AD7, AD8). Other types have different Mn contents, with the same base composition (e.g. AD9, AD10 and AD2, AD3, AD4). Those grades are used to study the influences of Mn and Si on the precipitation of Nb(C,N) and on the critical strain/peak strain ratio. Table 3.2 displays the chemical compositions of some of the multiply-alloyed and plain C-Mn grades studied here. The steels used for the torsion tests are marked with "TT".

Table 3.1 Chemical compositions of the niobium steels investigated (Group A).

Steel	Plant	C	Mn	Si	Nb	Ti	N*	Al	P	S
AA1TT	Algoma	.05	.35	.010	.035	-	.004	.043	.008	.006
AA2	Algoma	.05	.70	.100	.053	-	.005	.045	.007	.004
AA3	Algoma	.06	.70	.110	.058	-	.005	.045	.008	.004
AS1TT	Sumitomo	.07	1.12	.050	.023	.016	.000	.029	.019	.002
AS2TT	Sumitomo	.09	1.33	.060	.036	.016	.003	.019	.017	.020
AB	BHP	.11	1.05	.010	.031	-	.003	.040	.012	.012
AD1	Dofasco	.06	.65	.225	.020	-	.004	.035	.008	.005
AD2	Dofasco	.14	.65	.225	.020	-	.004	.035	.008	.005
AD3	Dofasco	.12	.85	.225	.020	-	.004	.035	.008	.005
AD4	Dofasco	.12	1.00	.225	.020	-	.004	.035	.008	.005
AD5	Dofasco	.06	.65	.115	.030	-	.004	.035	.008	.005
AD6	Dofasco	.06	.65	.010	.030	-	.004	.035	.008	.005
AD7	Dofasco	.06	.65	.115	.045	-	.004	.035	.008	.005
AD8	Dofasco	.06	.65	.010	.045	-	.004	.035	.008	.005
AD9	Dofasco	.06	.45	.010	.008	-	.004	.035	.008	.005
AD10	Dofasco	.06	.65	.010	.008	-	.004	.035	.008	.005
AD11	Dofasco	.06	1.25	.325	.075	.024	.004	.035	.008	.005
AD12	Dofasco	.06	1.25	.325	.080	-	.004	.035	.008	.005
AM1	"Davy"	.06	.70	.070	.050	-	.004	.051	.018	.013
AM2	"Davy"	.05	.45	.020	.020	-	.005	.047	.014	.008
AU	Usiminas	.11	.54	.002	.018	-	.004	.057	.014	.008

*For the Dofasco grades, a mean value of 40 ppm N is listed here. The actual values are taken into account in the spreadsheets.

Table 3.2 Chemical compositions of the multiply-alloyed and plain C-Mn steels.

Group	Steel	Plant	C	Mn	Si	Nb	Ti	Cr	Mo	V	Ni	N	Al	P	S
B	BCM	Sumitomo	.28	.52	.220	-	-	.83	.15	-	-	.005	.026	.016	.004
	BCMV	Sumitomo	.41	.63	.280	-	.015	1.38	.60	.27	.02	.006	.046	.013	.001
	BCMVN	Sumitomo	.47	.66	.170	.016	.016	.98	.87	.12	.46	.004	.042	.016	.004
C	CATT	Algoma	.03	.27	.010	-	-	-	-	-	-	.004	.042	.008	.010
	CS1TT	Sumitomo	.10	1.08	.060	-	-	-	-	-	-	.003	.020	.017	.003
	CS2	Sumitomo	.45	.76	.210	-	-	-	-	-	-	.005	.004	.017	.004
	CD	Dofasco	.06	.27	.000	-	-	-	-	-	-	.004	.035	.007	.005
	CM	"Davy"	.03	.24	.020	-	-	-	-	-	-	.004	.042	.009	.006
	CU	Usiminas	.05	.24	.002	-	-	-	-	-	-	.004	.030	.016	.010

3.1-Analysis of Mill Log Data

Logged data from five different hot strip mills were collected; these are listed below. Some 1300 logs were made available for analysis, of which about 300 were examined in detail.

Dofasco 7-stand HSM (Hamilton-Canada)
Algoma 6-stand-2.69 m wide HSM (Sault Ste. Marie-Canada)
Sumitomo 7-stand HSM (Kashima-Japan)
Sumitomo 7-stand HSM (Wakayama-Japan)
BHP 6-stand HSM (Port Kembla-Australia)

Data from other 2 hot strip mills were taken from the literature [66]. One is from the Usiminas 6-stand HSM in Brazil and the other is an unidentified 7-stand HSM referred to here as "Davy". The data that were employed consisted of:

Mill dimensions:

Interstand distances,

Work roll diameters,

Pyrometer locations.

For each strip:

Chemical composition,

Strip width

Thicknesses before and after all passes (H and h, respectively),

Work roll rotational speeds,

Roll forces,

Temperatures (mean values) for each pass according to a model or entry and exit temperatures.

The above parameters were then used to calculate the true strains and strain rates, interpass times and MFS's according to the Sims formulation, described in section 2.1.1.
The von Mises (effective) strain for each pass was calculated from the relation below:

$$\varepsilon = \frac{2}{\sqrt{3}} \ln\left(\frac{H}{h}\right) \tag{3.1}$$

The *average strain rate* during rolling can be defined as the effective strain divided by the time for the application of the strain:

$$\dot{\varepsilon} = \frac{\varepsilon}{t} = \frac{\varepsilon}{\left(\frac{\alpha \cdot 60}{2\pi U}\right)} \tag{3.2}$$

Here, U is the rotational speed in rpm and α is the arc of contact between the work roll and the strip, defined by:

$$\alpha = \arccos\left(1 - \frac{H-h}{2R'}\right) \tag{3.3}$$

where R' is the work roll flattened radius described in section 2.1.1.

3.2 - Redundant Strain Calculation in Strip Rolling

In addition to the nominal strain corresponding to the change in cross-sectional area during rolling, there is a "redundant" strain that arises from the finite length of the working zone. This can be thought of as the work done to change the direction of metal flow as it enters and leaves the deformation zone. Several numerical methods can be used to describe the redundant strain in rolling. These methods usually require considerable computation time and, for the sake of simplicity, a "geometrical method" is derived and employed here. The equation is based on a previous expression for the redundant strain in strip *drawing* [95]. The redundant strain factor ϕ defined in that work [95] was:

$$\phi = \frac{\varepsilon_r + \varepsilon_h}{\varepsilon_h} \tag{3.4}$$

where ε_r and ε_h are the redundant and homogenous strains, respectively. For plane strain conditions, the expression for the redundant strain factor as a function of the "die angle" ω is :

$$\phi = 1 + \frac{\frac{1}{2}\tan\omega}{\varepsilon_h} \tag{3.5}$$

Combining expressions (3.4) and (3.5):

$$\varepsilon_r = \frac{1}{2}\tan\omega \tag{3.6}$$

The roll and strip geometry for the case of strip *rolling* is shown in Fig. 3.1.

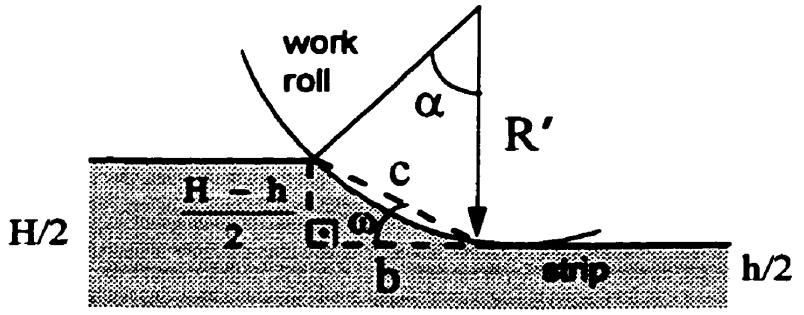

Figure 3.1 Geometry of roll/strip contact

The tangent of ω is defined by $\tan \omega = (H-h)/2b$. The value of b is first determined by calculating α and c. The angle α is given by Eq. 3.3 and the distance c can be deduced from α and R' as:

$$c = 2R'\sin(\alpha/2) \tag{3.7}$$

As a result, b is described by:

$$b = \sqrt{4R'^2 \sin^2(\alpha/2) - \frac{(H-h)^2}{4}} \tag{3.8}$$

Substituting $\tan \omega$ into Equation 3.6, the redundant strain pertaining to strip rolling is expressed as:

$$\varepsilon_r = \frac{H-h}{4\sqrt{4R'^2 \sin^2(\alpha/2) - \frac{(H-h)^2}{4}}} \tag{3.9}$$

Typical redundant strain factors fall in the range 1.07 to 1.16, so that the redundant strain itself is about 10% of (i.e. 0.07 to 0.16 times) the homogeneous strain. Note, however, that the larger the reduction, the larger is the redundant strain factor, so that the redundant strain increases more quickly than the nominal strain.

3.3 - Forward Slip Ratio Calculation

In order to have accurate values for the strain rates and interpass times, the strip speed at the exit of each pass must be estimated precisely. Between the entrance of the pass and the neutral axis, the strip speed is slower than the work roll tangential velocity, while beyond the neutral axis the strip speed is faster. Using mass flow equations [96], it is possible to derive the "forward slip" factor as a function of the neutral plane angle Φ_n, the roll radius R', the exit thickness, and the tangential velocity of the roll V_r (Fig. 3.2).

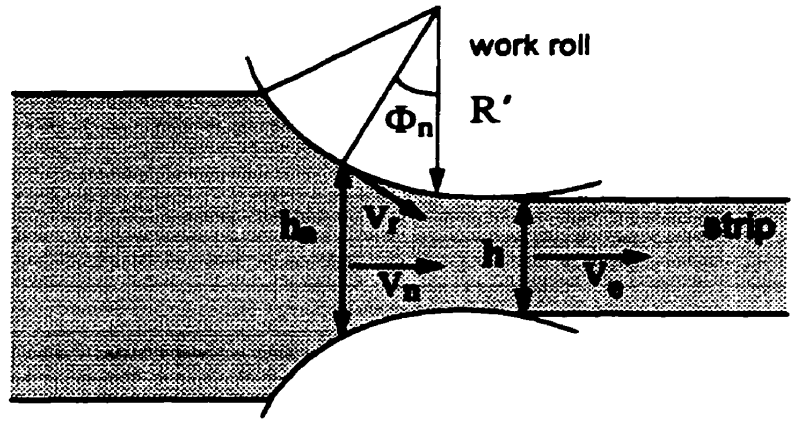

Figure 3.2 Neutral point geometry.

With reference to Figure 3.2, the strip speed at the neutral point is equal to the work roll tangential speed, given by:

$$V_r = 2\,\pi\,R' \cdot U \tag{3.10}$$

Considering the mass flow at the neutral and exit points, the following relation can be written:

$$V_e \cdot h \;=\; V_r \cdot h_n \cdot \cos\Phi_n \tag{3.11}$$

The thickness at the neutral point can be deduced as:

$$h_n \;=\; 2\left(R' - R'\cos\Phi_n\right) + h \;=\; 2R'\left(1 - \cos\Phi_n\right) + h \tag{3.12}$$

Substituting Equation 3.12 in Equation 3.11 and rearranging, results in:

$$V_e = V_r\left[1 + \left(\frac{2R'}{h}\cos\Phi_n - 1\right)\left(1 - \cos\Phi_n\right)\right] \tag{3.13}$$

Here, the neutral point angle, Φ_n, is obtained from the relation:

$$\Phi_n = \left(\frac{h}{R'}\right)^{1/2} \tan\left[\frac{\pi}{8}\left(\frac{h}{R'}\right)^{1/2} \ln(1-r) + \frac{1}{2}\tan^{-1}\left(\frac{r}{r-1}\right)^{1/2}\right] \quad (3.14)$$

where r is the reduction, defined by r = (H-h)/H and H and h are the initial and final thicknesses, respectively.

The expression for the exit strip speed V_e corrected for the forward slip ratio (λ) can be further simplified to:

$$V_e = V_r(1+\lambda) \quad (3.15)$$

Once the forward slip ratio is known, it is possible to calculate accurately the strip speed and, therefore, the interpass times can be calculated using:

$$t_{ip} = \frac{\text{interstand distance}}{V_e} \quad (3.16)$$

The flattened work roll radii were calculated according to the Hitchcock formulation, outlined in section 2.1.1 (Equations 2.8 and 2.9).

The equations described above were organized into a spreadsheet, using the Microsoft EXCEL ™ commercial software, which is widely used and available. Some typical spreadsheet inputs and outputs are shown in Figure 3.3.

INPUTS Data from mill logs

pass	Roll rad. (mm)	Roll spd (rpm)	Width (mm)	Gauge (mm)	Temp (°C)	Roll force (tonne)
				30.60		
F1	394	33.9	1264	17.33	987	2157
F2	391	54.5	1264	10.79	951	2223
F3	381	79.2	1264	7.42	915	2116
F4	365	119.0	1264	5.10	907	1691
F5	363	147.1	1264	3.90	896	1357
F6	376	167.2	1264	3.14	884	1264
F7	378	172.0	1264	2.61	872	1627

OUTPUTS

pass	Hitchcock R'(mm)	Forward slip factor	Nominal strain	Total strain*	Strn Rte (s-1)	Interpass time (s)	1000/T (K-1)	Sims MFS (MPa)
F1	403	1.10	0.66	0.75	12.9	3.48	0.79	116
F2	412	1.09	0.55	0.61	25.2	2.14	0.82	151
F3	416	1.08	0.43	0.48	41.3	1.48	0.84	179
F4	402	1.08	0.43	0.47	72.7	1.01	0.85	151
F5	428	1.06	0.31	0.34	94.2	0.79	0.86	178
F6	472	1.05	0.25	0.27	115	0.63	0.86	185
F7	561	1.04	0.21	0.23	131	–	0.87	250

*Includes the redundant strain.

Figure 3.3 Example of the spreadsheet calculations carried out using the mill data.

The same spreadsheet was used for the plain C-Mn, multiply alloyed and Nb grades; this is because it does not take into account any microstructural but only mechanical parameters. The MFS calculations were done according to the Sims method, described in section 2.1.1.*

3.4-Torsion Tests

The use of torsion tests permits the application of high strains when compared to the capabilities of other mechanical testing equipment. Numerous investigations have been performed on torsion machines during the past decades, especially in hot rolling studies. The simulation of hot rolling schedules is easily performed on

* An example of a full calculation of the Sims MFS is given in the Appendix on page 164 for the AS2 grade

3.4.1-McGill Torsion Machine

The stress-strain data analysed in this work were obtained from tests carried out on the servo-hydraulic computer-controlled MTS torsion machine at McGill. This device is equipped with a Research Inc. radiant furnace driven by a Leeds and Northrup controller. The motor is powered by an MTS hydraulic power supply, developing a maximum torque of 100 N-m and 628 rpm as its maximum rotational speed. A schematic representation of the torsion machine is given in Figure 3.4.

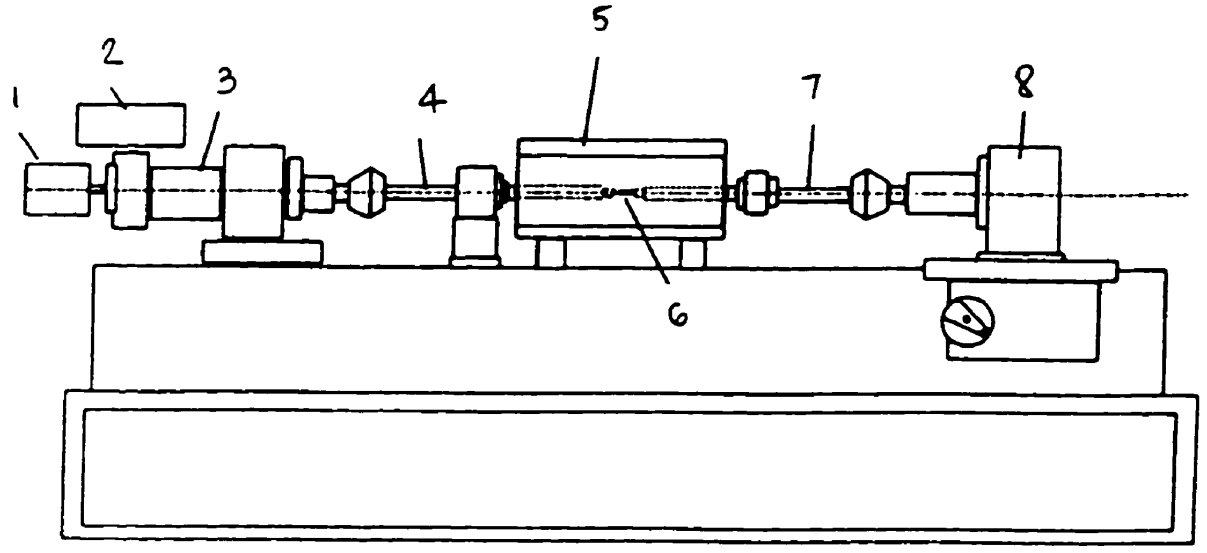

Figure 3.4 The McGill torsion machine. (1) potentiometer, (2) hydraulic servovalve, (3) hydraulic motor, (4) rotating torsion bar, (5) furnace, (6) specimen, (7) stationary grip, (8) torque cell.

The specimen is held by nickel-based superalloy grips, connected to the motor (4) and torque cell (7). A fused quartz tube encloses the grips and specimen in a flow of high purity argon passing inside the tube to avoid oxidation at high temperatures. The specimen is screwed into the stationary grip and fits into a slot on the rotating grip, where the torque is applied. The motor shaft twists the specimen through a programmed displacement angle, controlled and recorded by the potentiometer. The torque is read by the torque cell connected to the stationary grip. The control system consists of an MTS TestStar interface and a suitable program installed in a personal

computer. The association of the two devices permits "Windows - type" digital control for any desired stress-strain schedule.

Heat in the furnace is provided by four radiant elements focused on the specimen and the enclosure is water cooled. This configuration allows specimen temperatures of up to 1650°C to be reached. The Leeds and Northrup controller is connected to the programmer and to a thermocouple placed in contact with the specimen surface.

The recorded output from each test include: elapsed time, angle, torque and temperature.

3.4.2-Torsion Specimen

All samples were machined from the ends of transfer bars, cut in the shear crop, before entry into the HSM. The sample longitudinal directions were aligned parallel to the direction of rolling. The specimen geometry is displayed below.

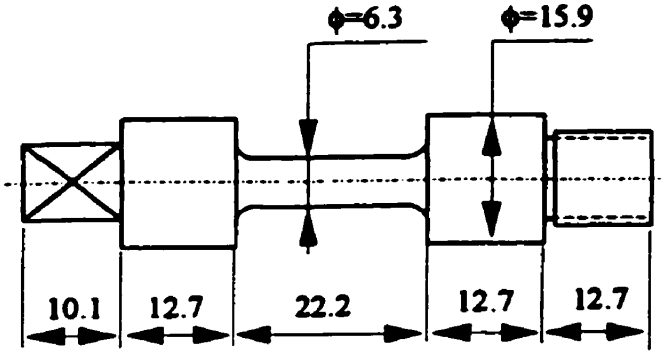

Figure 3.5 Geometry of the torsion specimen (in mm).

3.4.3-Calculation of Equivalent Stress, Strain and MFS

From the torque and angle readings, it is possible to calculate the equivalent (true) stress and equivalent (true) strain using appropriate relations. The equivalent stress varies along the specimen radius. At the surface the latter is given by the following equation, proposed by Fields and Backofen [97]:

$$\sigma_{eq} = \frac{\sqrt{3} \cdot T \cdot (3 + m + n)}{2\pi r^3} \tag{3.17}$$

Here T is the torque, r is the specimen radius, and m and n are defined by:

$$m = \partial \ln T / \partial \ln \dot{\Theta} \tag{3.18}$$

$$n = \partial \ln T / \partial \ln \Theta \tag{3.19}$$

where Θ and $\dot{\Theta}$ are the angle and angular velocity, respectively. Although both m and n vary with strain, for the sake of simplicity, the following constant values were employed: m = 0.17 and n = 0.13. As m+n values are generally in the range 0.1 to 0.5 and therefore significantly less than 3 (the mean value of the multiplier), there is an uncertainty of about 5% [98]. With m+n = 0.3, Equation 3.15 can be simplified down to:

$$\sigma_{eq} = \frac{3.3 \cdot \sqrt{3} \cdot T}{2\pi r^3} \tag{3.20}$$

The equivalent strain is calculated as follows:

$$\varepsilon_{eq} = \frac{r\Theta}{L\sqrt{3}} \tag{3.21}$$

where L is the specimen gage length.

3.4.4 - Test Schedules

For the grades tested in torsion, the austenitization temperature prior to deformation was 1200°C for all the steels tested here. A conditioning deformation was carried out at this temperature. With reference to the Nb grades, this temperature was selected after calculating the solution temperature, using the equation of Irvine et al. [53] given by:

$$\log[Nb]\cdot\left[C+\frac{12}{14}N\right]=2.26-\frac{6770}{T} \qquad (3.22)$$

This equation does not allow for the effects of Mn and Si on Nb(C,N) solubility, but gives a good approximation. According to Equation 3.22, the solution temperatures for the Nb grades tested in torsion vary from 1071 to 1156°C.

A) Single-pass tests

In order to estimate the MFS and peak strain behavior under DRX conditions, single pass torsion tests were performed for some of the grades. The deformation schedule is shown in Figure 3.6

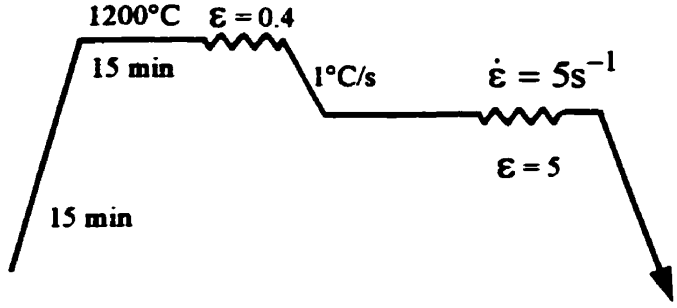

Figure 3.6 Deformation schedule for the single pass torsion test.

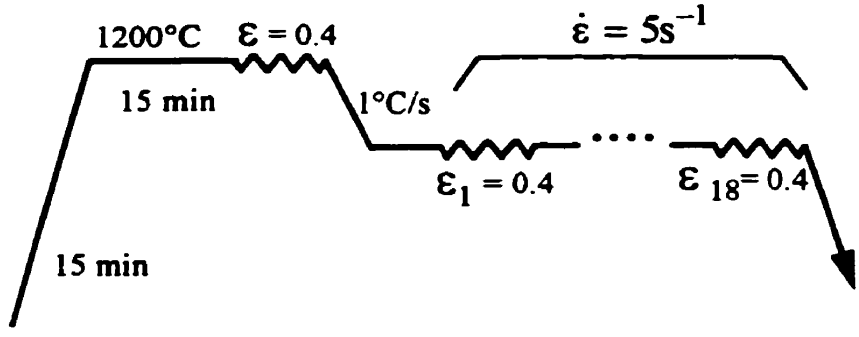

Figure 3.7 Deformation schedule for the 18-pass torsion test.

B) 18-pass continuous cooling tests

Torsion specimens were subjected to a series of 18 deformations each of 0.4 strain at a strain rate of 5/s. The deformation schedule can be visualized from Figure 3.7. The time interval between each pass was 3s and the initial and final temperatures were 1050 and 850°C, resulting in a mean cooling rate of 2°C/s. These tests were performed in order to obtain MFS vs. 1/T information under continuous cooling conditions.

Calculation of the MFS from stress-strain data was done by evaluating the area under the curve by numerical integration. Over the strain range ε_a to ε_b, the average stress, σ_{av}, is calculated over each small increment of strain $\Delta\varepsilon$. Employing n strain increments of size $\Delta\varepsilon$, the MFS is given by:

$$MFS = \frac{\sum_{i=1}^{n} \sigma_{av} \Delta\varepsilon}{\varepsilon_a - \varepsilon_b} \tag{3.23}$$

Graphically, the integration parameters are displayed in Figure 3.8. Here, the strain increment used for MFS calculation was 0.05.

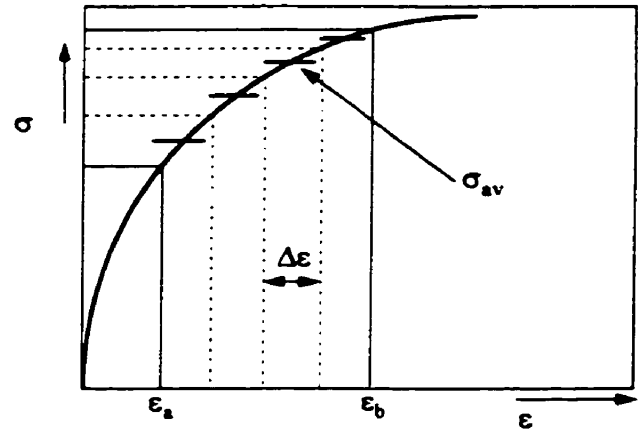

Figure 3.8 Parameters used in the numerical integration for the MFS calculation.

Chapter 4 - The Mean Flow Stress Prediction Model

For plain C-Mn steels, the MFS depends strongly on the temperature, strain, strain rate and carbon content and, to a small extent, on the presence of other alloying elements, such as Mn. The Misaka equation, discussed in Chapter 2, gives good MFS predictions for C-Mn grades if full SRX occurs between passes. However, there is no allowance for the increase in MFS due to the presence of other alloying elements nor for the occurrence of strain accumulation and DRX, both of which lead to departures from true "Misaka behavior". The latter effects cause increases and drops in the MFS, respectively, which are not predicted by Misaka's equation. These deficiences led to the derivation of the new MFS formulation described below, which uses Misaka's as the "base equation". The improvements are designed to cover different chemical compositions as well as the occurrence of DRX.

4.1 - MFS Equation Based Only on SRX

Misaka's equation has often been used to specify the MFS for C-Mn steels during hot strip rolling and was used here as the basis for a modified equation that takes into account the effects of alloying elements such as Mn, Nb, Ti, as well as other elements applicable to the group B grades.

The method used here calculates the MFS for several strips according to Sims' formulation, described in section 2.1.1, after which the results are plotted versus 1000/T. However, the derived MFS's are "normalised" because, in strip rolling, the reductions are applied at various strains and strain rates; this makes it difficult to compare MFS values from one stand to the next. It is therefore useful, particularly in the present type of work, to "correct" them to constant values of strain and strain rate (e.g. $\varepsilon = 0.4$, $\dot{\varepsilon} = 5s^{-1}$) by using the expression:

$$MFS_{corr} = MFS_{Sims} \times \left(\frac{0.4}{\varepsilon_{pass}}\right)^{0.21} \times \left(\frac{5}{\dot{\varepsilon}_{pass}}\right)^{0.13} \qquad (4.1)$$

The exponents 0.21 and 0.13 are the strain sensitivity and strain rate sensitivity, respectively. The strain exponent 0.21 differs from the value used in Equation 3.17 because here the MFS's will be compared directly to Misaka MFS's. For this reason, the strain exponent appearing in Misaka's equation is employed in Equation 4.1. When the values of MFS_{corr} calculated in this way are plotted vs. 1/T, the temperature and "history" dependence of the MFS during strip rolling can be seen more clearly. By plotting the normalised MFS's versus 1000/T for several strips, the "mean" MFS value can be determined in the high temperature region, i.e. where SRX occurs. This region is represented in Figure 4.1 for a Dofasco grade. Correction factors can be derived for each group of steels.

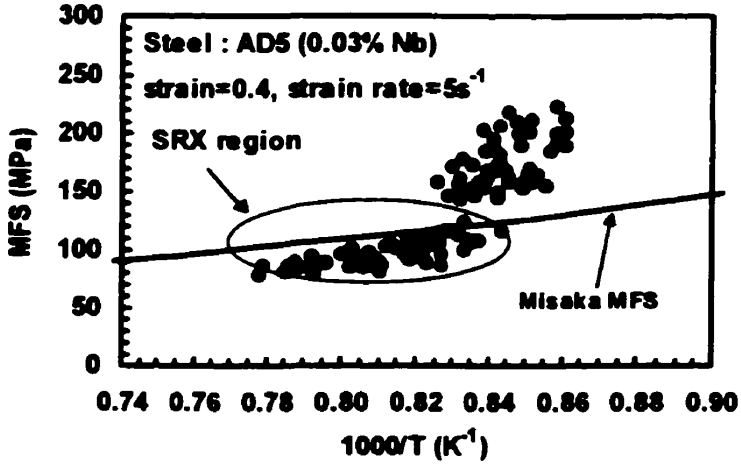

Figure 4.1 MFS vs. 1000/T calculated from mill logs for grade AD5 (0.03%Nb), corrected to a constant strain (0.4) and strain rate ($5s^{-1}$).

Here it is assumed that full SRX takes place between passes. Three MFS formulations are derived here: for Nb , C-Mn and multiply alloyed steels.

4.1.1 - Nb Steels

The fit between the mill log and Misaka values in the SRX region can be improved by allowing for the solution strengthening effects of Nb, Mn and Ti. The corrected values, as established for grades AA1, AS1, AS2, AB, AD5 and AD11 in the SRX region, are represented by MFS* in the following modified version of Misaka's equation:

$$MFS^* = MFS_{Misaka}(0.768 + 0.51[Nb] + 0.137[Mn] + 4.217[Ti]) \qquad (4.2)$$

Equation 4.2 is valid over the following concentration ranges: Nb:[0.020-0.080%], Mn:[0.35-1.33%], Ti:[0-0.024%]. The Sims data derived from the mill logs are compared to the Misaka and MFS* equations (all normalized to a strain of 0.4 and a strain rate of $5s^{-1}$) in Figures 4.2 to 4.7. For grades AS1 and AS2, the results obtained in the 18-pass torsion tests are also shown (Figures 4.3 and 4.4); here, the interpass times were 3s.

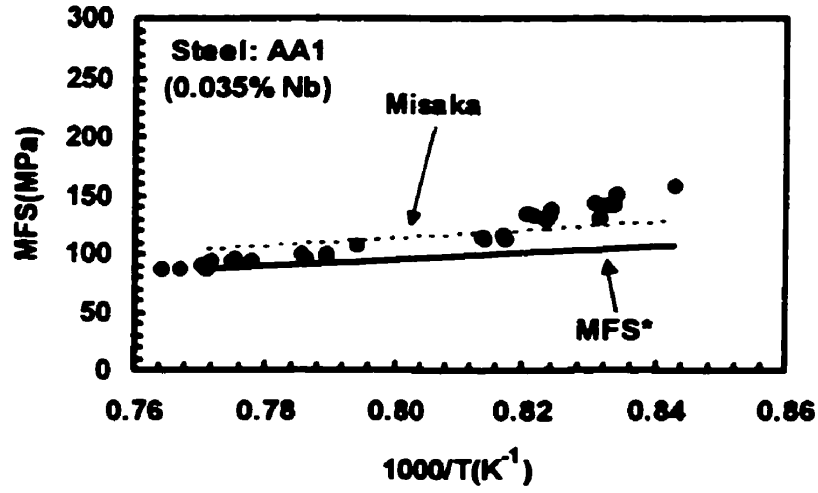

Figure 4.2 The Misaka equation and the present modified expression for MFS* are compared with the Sims MFS values calculated from mill logs. Here, the MFS is plotted vs. 1000/T for grade AA1 (0.035%Nb), after correction to a constant strain of 0.4 and to a constant strain rate of $5s^{-1}$.

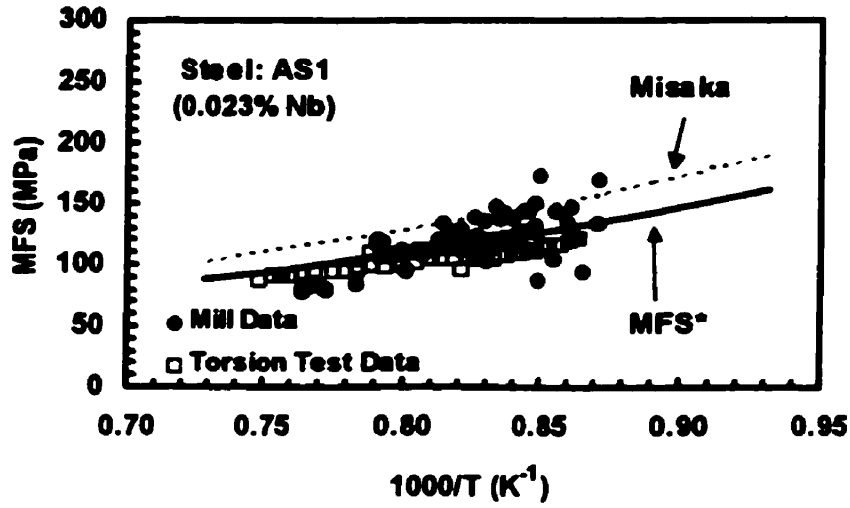

Figure 4.3 The Misaka equation and the present modified expression for MFS* are compared with the Sims MFS values calculated from mill logs. Here, the MFS is plotted vs. 1000/T for grade AS1 (0.023%Nb), after correction to a constant strain of 0.4 and to a constant strain rate of $5s^{-1}$. The results obtained from 18-pass torsion tests are also shown.

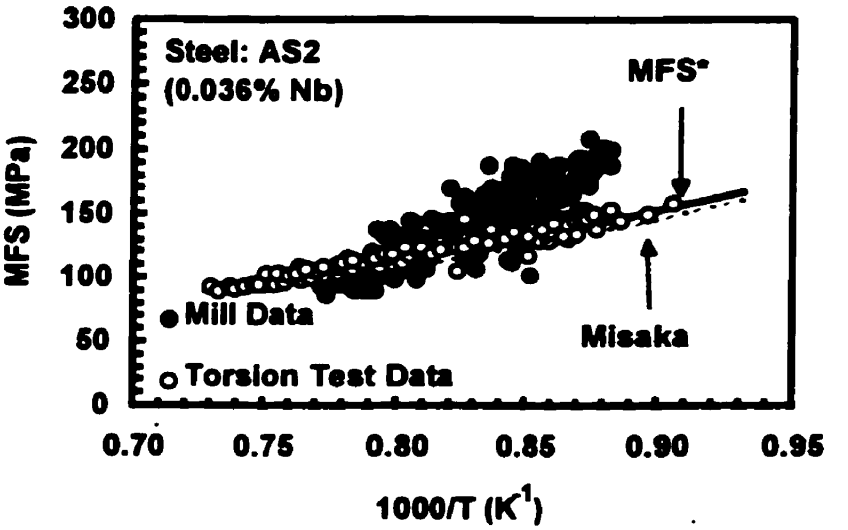

Figure 4.4 The Misaka equation and the present modified expression for MFS* are compared with the Sims MFS values calculated from mill logs. Here, the MFS is plotted vs. 1000/T for grade AS2 (0.036%Nb), after correction to a constant strain of 0.4 and to a constant strain rate of $5s^{-1}$. The results obtained from 18-pass torsion tests are also shown.

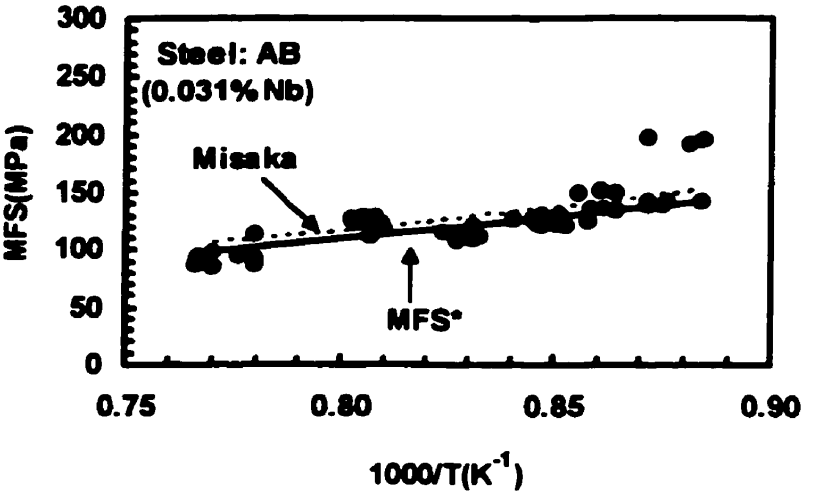

Figure 4.5 The Misaka equation and the present modified expression for MFS* are compared with the Sims MFS values calculated from mill logs. Here, the MFS is plotted vs. 1000/T for grade AB (0.031%Nb), after correction to a constant strain of 0.4 and to a constant strain rate of $5s^{-1}$.

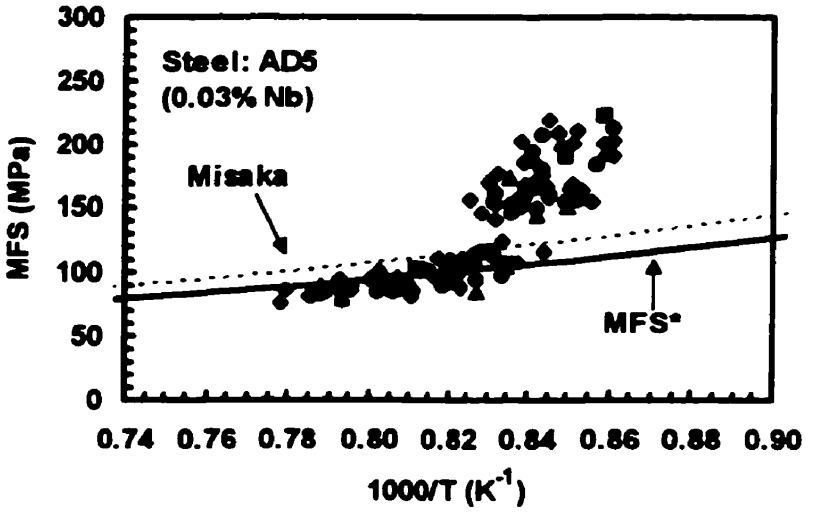

Figure 4.6 The Misaka equation and the present modified expression for MFS* are compared with the Sims MFS values calculated from mill logs. Here, the MFS is plotted vs. 1000/T for grade AD5 (0.03%Nb), after correction to a constant strain of 0.4 and to a constant strain rate of $5s^{-1}$.

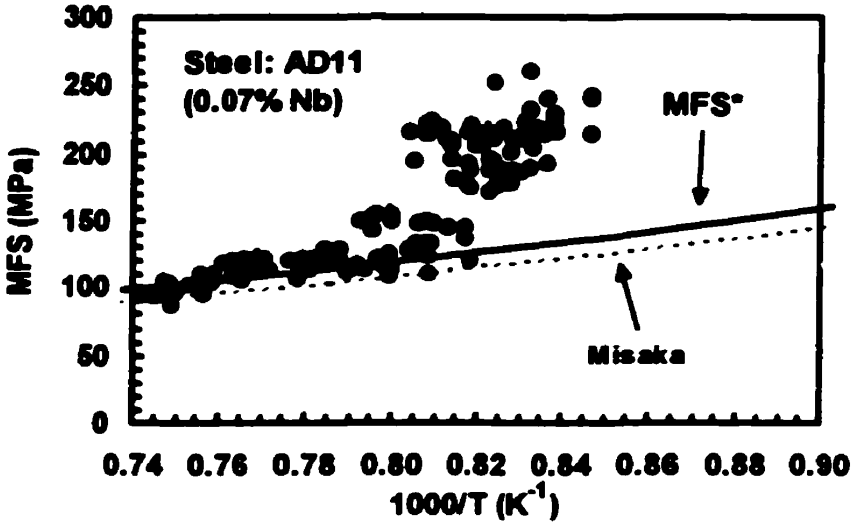

Figure 4.7 The Misaka equation and the present modified expression for MFS* are compared with the Sims MFS values calculated from mill logs. Here, the MFS is plotted vs. 1000/T for grade AD11 (0.07%Nb), after correction to a constant strain of 0.4 and to a constant strain rate of $5s^{-1}$.

It can be seen that Misaka's equation *overpredicts* the MFS's obtained from the mill logs of a Nb steel containing 0.03%Nb. On the other hand, it *underpredicts* the MFS values for the higher Nb grades. It is also clear that the slope of the Misaka equation agrees reasonably well with the mill log values in the region where the former is quite shallow (i.e. at low 1/T or high T). This indicates that full SRX is occurring between the passes in this region.

Regarding the Ti solution strengthening factor of 4.21, there is a possible reason why this value is much higher than for Nb (beyond experimental error): as Ti combines with most of the C and N at elevated temperatures, this will help to keep the Nb in solid solution and therefore avoid Nb(C,N) precipitation during finishing. The Nb can then contribute its own solute hardening effect, thereby increasing the MFS. During the derivation of the equation, this "indirect" mechanism of strengthening may be responsible for the high value of the Ti coefficient.

The addition of solution strengthening factors allows Misaka's equation to fit all grades well. For grades AS1, AS2 and AB, the solution strengthening is due to the high Mn content (1.12, 1.33 and 1.08 %, respectively). The changes described above lead to good agreement between the modified Misaka equation (MFS*) and the mill values.

4.1.2 - Plain C-Mn Steels

It is common to find Mn levels varying from 0.2 to 1.5% in plain C-Mn steels. Therefore, the solution strengthening effect due to Mn described above is also taken into account here. The MFS* equation obtained for the plain C-Mn grades in this way is shown below:

$$MFS^* = MFS_{Misaka}(0.768 + 0.137[Mn]) \tag{4.3}$$

The Mn concentrations studied ranged from 0.27 to 1.08%. Figures 4.8 to 4.10 display the MFS data obtained from the mill logs using the Sims formulation, as well as the Misaka and MFS* equations, all normalized to a constant strain (0.4) and strain rate ($5s^{-1}$). Torsion test data for the CS grade obtained in the 18-pass torsion tests are included in Figure 4.9.

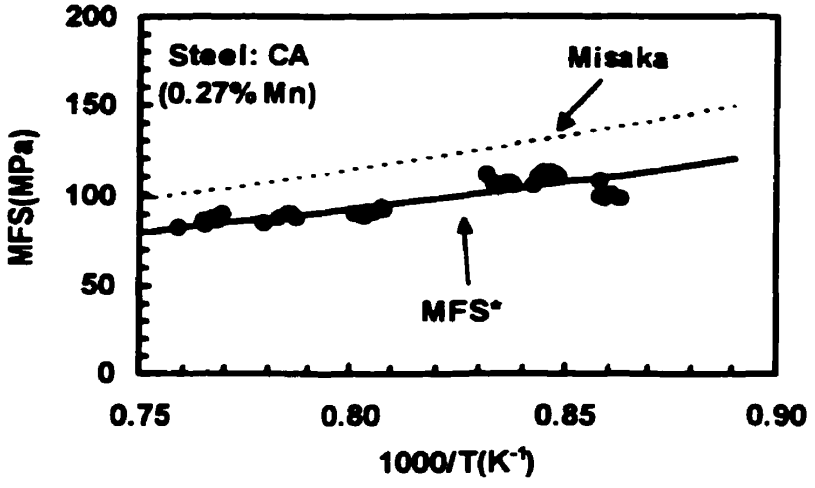

Figure 4.8 The Misaka equation and the present modified expression for MFS* are compared with the Sims MFS values calculated from mill logs. Here, the MFS is plotted vs. 1000/T for grade CA, after correction to a constant strain of 0.4 and to a constant strain rate of $5s^{-1}$.

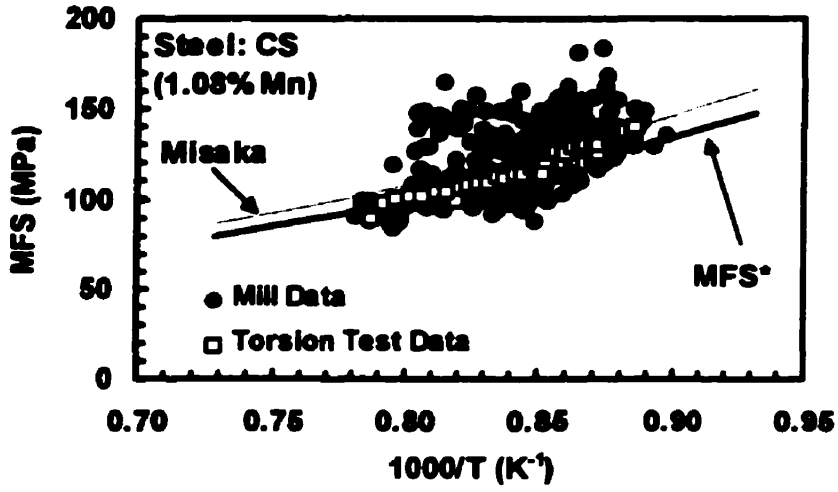

Figure 4.9 The Misaka equation and the present modified expression for MFS* are compared with the Sims MFS values calculated from mill logs. Here, the MFS is plotted vs. 1000/T for grade CS, after correction to a constant strain of 0.4 and to a constant strain rate of $5s^{-1}$. The results obtained from 18-pass torsion tests are also shown.

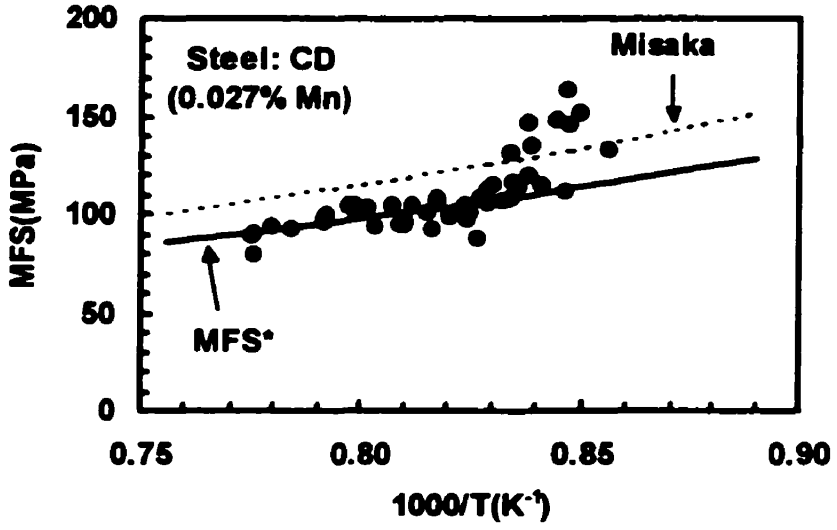

Figure 4.10 The Misaka equation and the present modified expression for MFS* are compared with the Sims MFS values calculated from mill logs. Here, the MFS is plotted vs. 1000/T for grade CD, after correction to a constant strain of 0.4 and to a constant strain rate of $5s^{-1}$.

In these cases, the Misaka equation always overpredicts the Sims MFS values calculated from the mill logs. In a similar analysis made for the Nb steels, the high

Mn level (1.08%) in the CS grade compensated for the difference. Thus, the present analysis suggests that the Misaka equation was determined for steels with Mn concentrations of about 1.6%, the level at which the two relations coincide. With respect to Misaka's equation, it was formulated using steels containing different Mn contents, the mean concentration of which was about 1%. The overprediction can therefore be attributed to other factors, such as the type of mechanical test used, the concentration of Si, and other variables. The influence of these factors will be analysed later on in this section.

4.1.3 - Multiply-Alloyed Steels

The same approach was used to derive the MFS* equations for the group C steels. The mill log analysis led to the equation shown below, which takes into account the solution hardening effects due to Mn, Nb, Cr, Mo, V and Ni. In order to include all these elements, some steel compositions pertaining to the other groups were used.

$$MFS^* = MFS_{Misaka}(0.835 + 0.098\,[Mn] + 0.51\,[Nb] + 0.128\,[Cr]^{0.8} + \\ + 0.144\,[Mo]^{0.3} + 0.175\,[V] + 0.01\,[Ni]) \qquad (4.4)$$

Equation 4.4 is considered to apply to the following composition ranges: Mn:[0.52-0.66%], Nb:[0-0.08%], Cr:[0.83-1.38%], Ni:[0-0.46%], Mo:[0.15-0.97%], V:[0-0.27%]. Due to high maximum concentrations of Cr and Mo, the solution effects approached "saturation", which is why exponents were employed in the model. The effects of the other elements are considered to be linear over their concentration intervals.

Here, a brief comment on the differences between the "intercept" and Mn coefficients in Equations 4.2 and 4.4 is called for. Comparison of Tables 3.1 and 3.2 indicates that the Equation 4.2 (Group A) steels, Table 3.1, have only *half* the average Si levels (about 0.11) compared to the Equation 4.4 (Group B) steels of Table 3.2 (about 0.22% Si). At the time this analysis was carried out, no account was taken of the Si levels on the MFS, and therefore on the rolling load. In retrospect, however, this would have been desirable, as it appears from a study of

the above relations that the introduction of such a term may have permitted the use of a *single* set of coefficients.

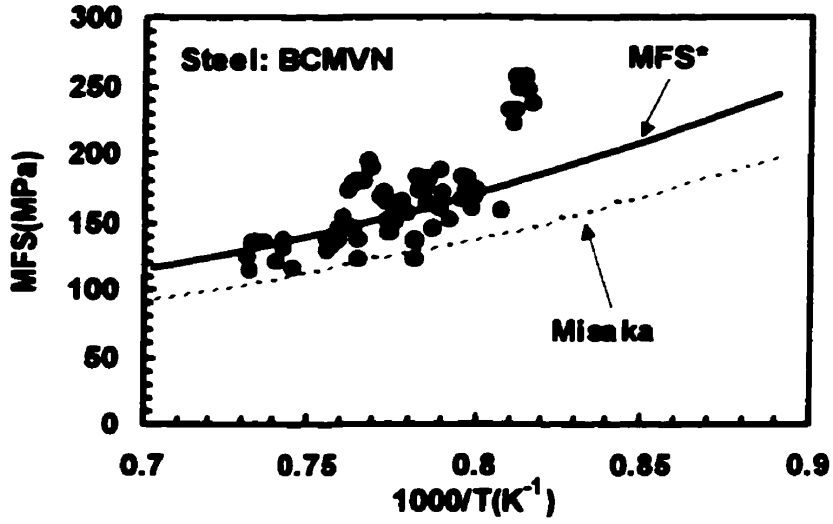

Figure 4.11 The Misaka equation and the present modified expression for MFS* are compared with the Sims MFS values calculated from mill logs. Here, the MFS is plotted vs. 1000/T for grade BCMVN, after correction to a constant strain of 0.4 and to a constant strain rate of $5s^{-1}$.

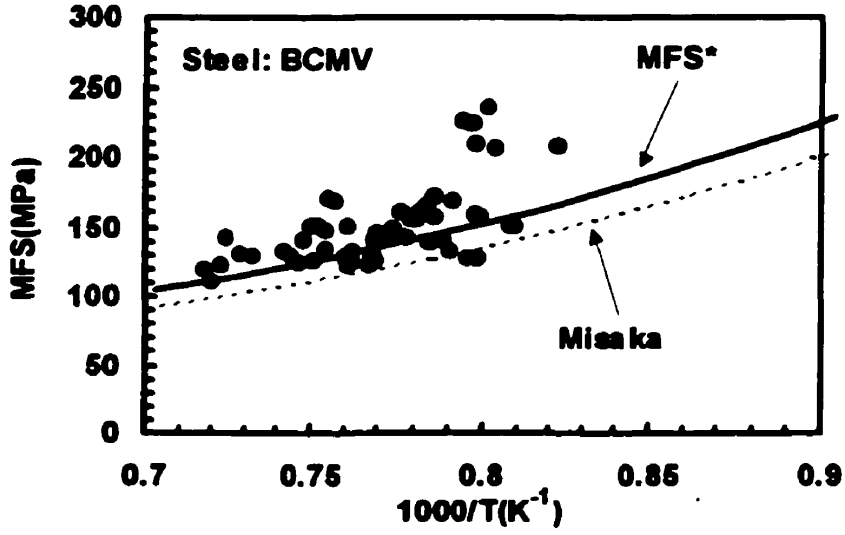

Figure 4.12 The Misaka equation and the present modified expression for MFS* are compared with the Sims MFS values calculated from mill logs. Here, the MFS is plotted vs. 1000/T for grade BCMV, after correction to a constant strain of 0.4 and to a constant strain rate of $5s^{-1}$.

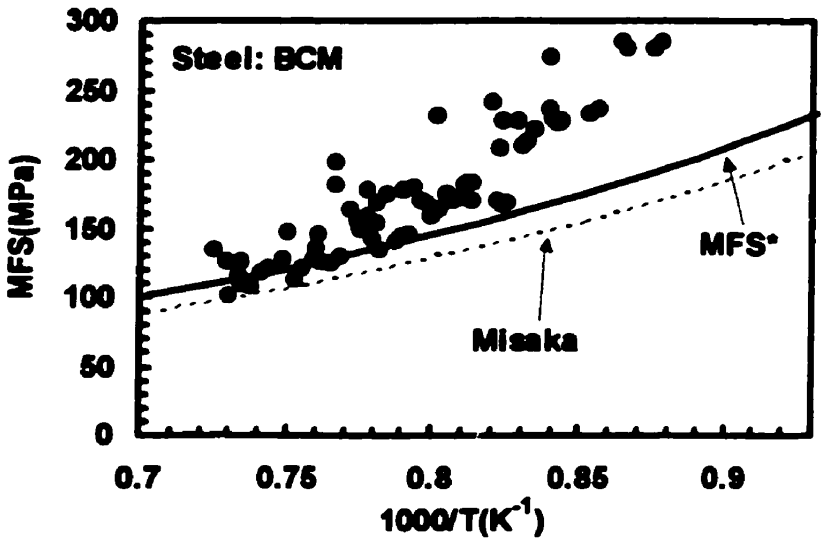

Figure 4.13 The Misaka equation and the present modified expression for MFS* are compared with the Sims MFS values calculated from mill logs. Here, the MFS is plotted vs. 1000/T for grade BCM, after correction to a constant strain of 0.4 and to a constant strain rate of $5s^{-1}$.

It is apparent from Figures 4.11 to 4.13 that the original Misaka equation calls for MFS values that are too low. This is simply because the unmodified equation applies solely to C-Mn steels and does not take the presence of any additional alloying elements into account. However, even the present improved Misaka equation is unable to specify the MFS behaviour in the "high slope" regions; i.e. in the last few passes of rolling. This behaviour can be attributed to incomplete SRX, leading to strain accumulation. This effect occurs even in the plain C-Mn grades, but to a lesser extent.

It should be noted that the original Misaka relation slightly overpredicts the MFS even in the "low Nb" (less than about 0.04% Nb) grades studied here. This overprediction is also observed in the plain C-Mn steels. The difference in load behaviour during rolling and in the drop hammer test (used by Misaka and Yoshimoto) can be considered responsible for this overestimation; this can be associated with the very high strain rates associated with the latter type of test.. This overprediction is compensated for in the "high Nb" grades (above about 0.04 % Nb) because of the extensive Nb solution strengthening effect at rolling temperatures.

The same effect is observed in the multiply-alloyed grades, due to the strong solution strengthening brought about by adding Mo, Cr and V.

It should be noted that, if sufficient data are available for a wide range of chemistries, terms can be added to the MFS formulation, allowing for the effects of other alloying elements (as already indicated above for the case of Si).

4.2 - An MFS Equation That Takes DRX Into Account

The experimental data from the 18-pass torsion testing of Sumitomo Nb grades AS1 and AS2 is also well described by Equation 4.2, as illustrated in Figures 4.3 and 4.4 above (particularly in the early, high temperature, passes). The interpass time used in these tests is 3s, long enough to allow considerable softening. Also, the identical applied strains of 0.4 did not exceed the critical strain for the initiation of DRX. Misaka's equation, as well as the current MFS* equation, assume that full static recrystallization takes place between passes. However, in Nb-containing steels, recrystallization is frequently incomplete when the interpass times are short, particularly during the later passes of strip rolling, when the temperature is relatively low. This leads to strain accumulation, which may in turn cause the initiation of dynamic recrystallization followed by metadynamic recrystallization. These three microstructural processes can be expected to contribute to the departures from the Misaka and present equations evident in Figures 4.2 to 4.7.

Because MFS* is based on a simple power-law expression, it is evident that it cannot characterise the flow curve appropriately in the high strain range within which DRX becomes important. The MFS* equations were therefore modified by taking the effects of DRX into account. For this purpose, the DRX steady-state stress (σ_{ss}) was first described as follows [29]:

$$\sigma_{ss} = A\,\dot{\varepsilon}\exp\left(\frac{Q_{def}}{RT}\right)^{q} \qquad (4.5)$$

where A and q are parameters that depend on composition, and Q_{def} is the activation energy for deformation. The values of this parameters are listed in Table 4.1.

Table 4.1 Parameters for the steady-state stress equation

Steel	A	Q_{def} (kJ/mol)	q	reference
Nb	4.2	375	0.09	[30]
C-Mn	7.2	300	0.09	[30]
Multiply-alloyed	1.18	330	0.15	[99]

Following the approach of Senuma et al. [17,18,55], allowance was made for the fractional softening attributable to DRX (when $\varepsilon > \varepsilon_c$) as follows:

$$X_{dyn} = 1 - \exp\left[-0.693\left(\frac{\varepsilon - \varepsilon_c}{\varepsilon_{0.5}}\right)^2\right] \tag{4.6}$$

and

$$\varepsilon_{0.5} = 1.144 \times 10^{-3} d_0^{0.25} \dot{\varepsilon}^{0.05} \exp(6420/T) \tag{4.7}$$

Here X_{dyn} is the fractional softening attributable to DRX, ε_c is the DRX critical strain, $\varepsilon_{0.5}$ is the strain for 50% recrystallization, and d_0 is the initial grain size for each pass. Although these relations were originally proposed for C-Mn steels, their use will be extended here to the Nb and multiply-alloyed grades, by modifying the expression for ε_c as well as for the initial constant of Eq. (4.7). The latter change is necessary because of the slower DRX kinetics in alloyed steels. The final MFS equation is obtained by combining the MFS* formulations with Equations 4.5 to 4.7:

$$MFS^+ = MFS^* \ (1 - X_{dyn}) + K\sigma_{ss}X_{dyn} \tag{4.8}$$

where the coefficient K = 1.14 is a fitting parameter required to convert from stress to *mean* flow stress. This coefficient has nothing to do with converting from von Mises to plane strain. Instead, it is related to converting from a stress value (σ_{ss}) to an MFS value. At large strains, this coefficient approaches 1. Analysis of this equation shows that when $\varepsilon < \varepsilon_c$, X_{dyn} is zero and nothing changes (i.e. MFS^+ is equal to MFS*). When X_{dyn} is equal to 1, MFS^+ is equal to the "steady-state *mean flow stress*", a situation that applies under full DRX softening conditions. The results of some large-strain torsion tests on the AS2 (0.036 % Nb), AA1 (0.035% Nb), BCMVN, CS and CA grades are compared with the MFS^+ and MFS*

predictions in Figures 4.14 to 4.18. Note that, while the output of a torsion test is usually given in terms of stress vs. strain, the present analysis is expressed in terms of *mean flow stress* vs. strain. The experimental flow stresses were therefore converted into MFS^+ values by evaluating Equation 3.21 over increments of $\Delta\varepsilon = 0.02$. The MFS behaviour described by Equations 4.2 to 4.8 provides a good fit to the experimental results from the single pass torsion tests.

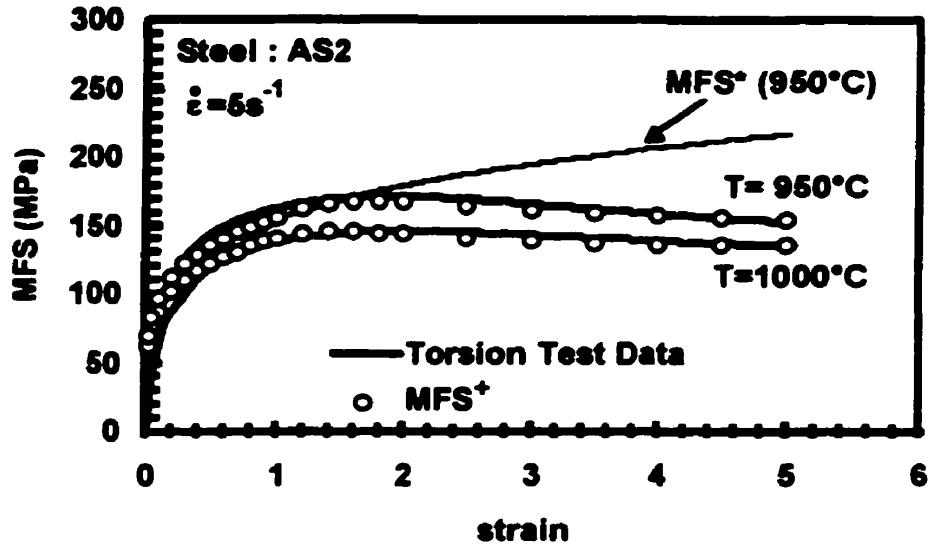

Figure 4.14 Comparison between the MFS* and MFS^+ equations, the MFS prediction and the results of torsion tests on the AS2 grade (0.036% Nb).

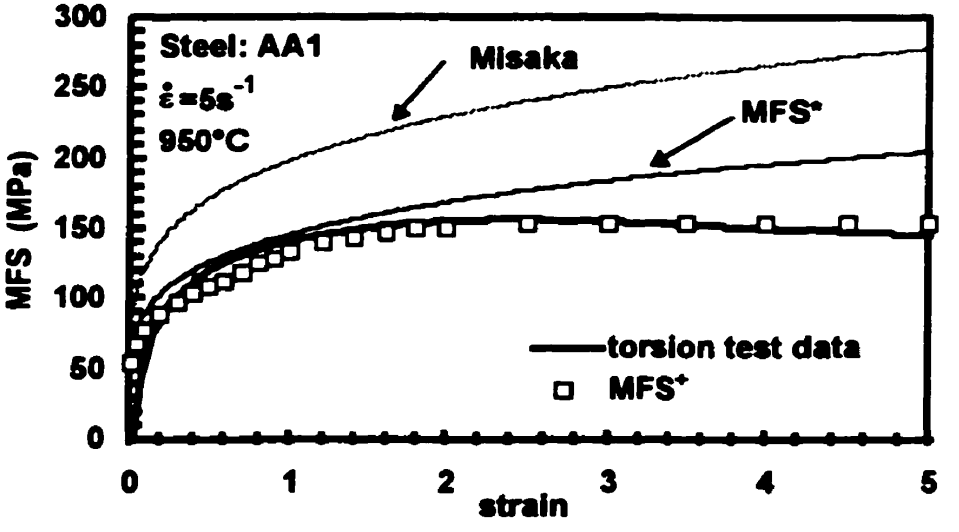

Figure 4.15 Comparison between the Misaka, MFS* and MFS^+ equations and the results of torsion tests on the AA1 grade (0.035% Nb).

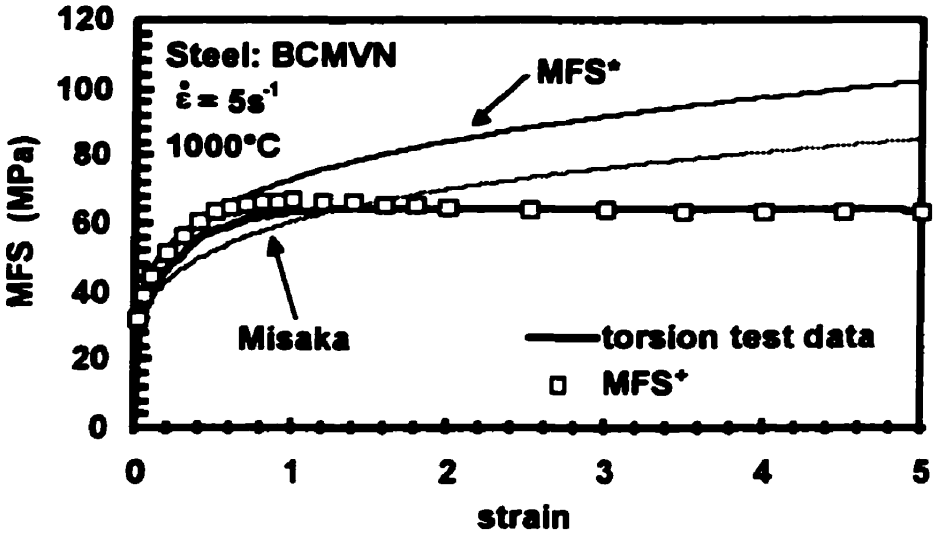

Figure 4.16 Comparison between the Misaka, MFS* and MFS$^+$ equations and the results of torsion tests on the BCMVN grade (multiply-alloyed).

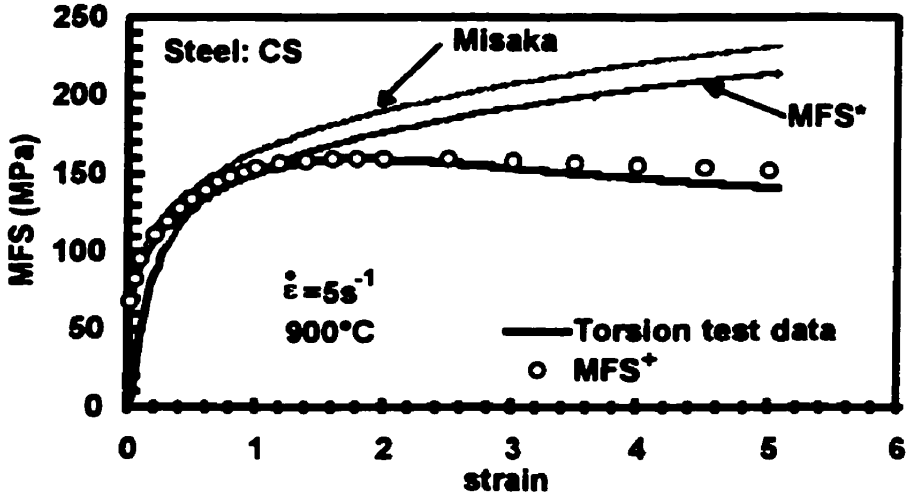

Figure 4.17 Comparison between the Misaka, MFS* and MFS$^+$ equations and the results of torsion tests on the the CS grade (1.08% Mn).

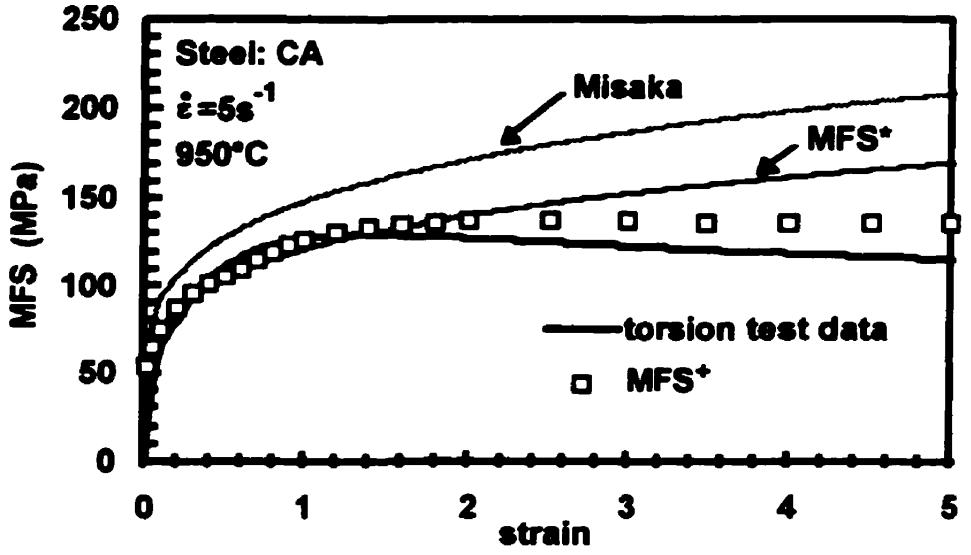

Figure 4.18 Comparison between the Misaka, MFS* and MFS$^+$ equations and the results of torsion tests on the the CA grade (0.27% Mn).

The method developed here first requires that a steel be classified as belonging to group A, B or C. The appropriate MFS*, σ_{ss}, $\varepsilon_{0.5}$ and ε_c equations are then selected. These parameters are used to calculate MFS$^+$ with the aid of equation 4.8. This equation will be used later on to predict MFS values under industrial rolling conditions.

Chapter 5 - Modeling Fractional Softening and Grain Size During Hot Strip Rolling

During a particular pass of a rolling schedule, the sum of the retained and applied strains will determine which softening mechanism (SRX or DRX+MDRX) will operate. Depending on the type of softening, different equations are then employed that specify the grain size and fractional softening. In this chapter, a method is described that can be used to follow the microstructural evolution during multi-pass rolling; it is based on equations found in the literature.

For now, no attention will be paid to the exact onset of DRX and the critical strain will be taken simply as a fixed fraction of the peak strain. The example given in the present chapter involves modeling microstructural evolution in a plain C-Mn grade and the critical strain is considered to be $0.8\varepsilon_p$. The onset of DRX in Nb steels will be discussed later on in Chapter 6.

During rolling, the temperature decreases continuously. Thus, the temperature adopted for each interpass interval is taken as the average temperature between the prior and subsequent pass. This assumption is employed because the present equations were derived for isothermal conditions and the interpass times are short enough to allow the use of a single temperature value.

In the present work, the recrystallization and grain size models described below were incorporated into the Microsoft EXCEL™ spreadsheet software, as

shown in more detail at the end of this chapter. The sub-models involved here were assembled by following a method developed for rod rolling [36].

The recrystallization kinetic equations used here are adaptations of the AJMK equation, with different parameters. As each equation was derived under particular conditions of testing, theoretical justifications for the choice of a particular equation become impractical. The equation that best fitted the mill data was therefore used.

5.1 - Softening Between Passes

The use of mechanical testing led to the term "mechanical metallography", an approach that permits the direct association of softening and recrystallization. This is particularly true for low SFE metals such as austenite, as discussed in Chapter 2. A softening model uses parameters such as strain, strain rate, initial grain size and temperature to decide upon the mechanism and calculate the extent of softening. In a hot strip mill, the softening between passes can be calculated with the aid of an MFS equation and temperature corrections. In the present work, the microstructural evolution equations were tested directly in the spreadsheet for the three groups of steels. The $t_{50\%}$ equation selected for each group (most of these were already displayed in Chapter 2) is shown in Table 5.1.

Table 5.1 Equations describing the softening kinetics.

Group	Type	Equation	Ref.
A	SRX	Eq. 2.27 and 2.29	[20]
	DRX	Eq. 2.53 and 2.54	[30,31]
B	SRX	$t_{0.5} = 1.57 \times 10^{-14} \cdot d_0^2 \cdot \varepsilon^{-2.9} \exp\left(\frac{271000}{RT}\right)$ (5.1)	[99]
	DRX	$t_{0.5} = 1.84 \times \left[\dot{\varepsilon} \cdot \exp\left(\frac{330000}{RT}\right)\right]^{-0.86} \exp\left(\frac{271000}{RT}\right)$ (5.2)	[99]
C	SRX	Eq. 2.27 and 2.28	[20,21]
	DRX	Eq. 2.55 and 2.56	[33]

Note that Equation 2.54 is the only one available for the DRX kinetics of Nb steels. The same expression is employed for the multiply-alloyed grades, as derived in a recent study. For the C-Mn steels, several equations are available; however, the ones developed by Hodgson et al. [20,21] provided the best fit to the mill logs.

5.2 - Strain Accumulation Between Passes

Partial recrystallization between passes results in retained strain, which must be added to the strain applied in the subsequent stand. The accumulated strain in pass *i* ($i > 1$) then becomes [100]:

$$\varepsilon_i^a = \varepsilon_i + K \cdot (1 - X_{i-1}) \cdot \varepsilon_{i-1} \tag{5.3}$$

where X is the fractional softening and K is a constant. K was reported in the literature as falling between 0.5 and 1 [36,100]. The parameter K can be related to the rate of recovery. High rates of recovery result in less accumulated strain. This is clear in the work by Gibbs et al. [100], where longer interpass times led to $K = 0.5$ and shorter interpass times (less recovery) to $K = 1$. In the present hot strip model, the K constant is assumed to be 1 and the accumulated strain is used in all the calculations; this is because it represents the actual amount of strain present within the material.

5.3 - Grain Size Evolution

The incorporation of grain size equations into any mathematical model relies on some assumptions regarding incomplete recrystallization. How is the grain size of a partially recrystallized material to be defined? What about growth of the recrystallized grains while other regions are still work hardened? These questions will be answered in the following sections.

5.3.1 - Recrystallized Grain Size

This calculation simply takes into account the initial grain size, strain and/or strain rate. The grain size after SRX is well known to be strongly dependent on the prior strain and only depends on the strain rate to a minor extent. On the other hand, the grain sizes after MDRX are strongly dependent on the strain rate [1,21,29-31,33,35,73,101]. The equations used here, already displayed in Chapter 2 as well, are listed in Table 5.2.

Table 5.2 Equations describing the recrystallized grain size.

Group	Type	Equation	Ref.
A	SRX	Eq. 2.37	[16]
	DRX	Eq. 2.58	[30]
B	SRX	Eq. 2.37	[16]
	DRX	Eq. 2.58	[31]
C	SRX	Eq. 2.35	[20,21]
	DRX	Eq. 2.57	[20,21]

The grain size pertaining to the entrance of a given pass is considered as the "initial" grain size d_0. Note that the equations used to model the recrystallized grain sizes for the steels pertaining to groups A and B are the same; this is due to the lack of appropriate equations for the multiply-alloyed steels.

In the case of incomplete recrystallization, the initial grain size for the following pass, $d_{0\ i+1}$, can be calculated using the following relation [36,37,88] which determines a kind of "average" from the freshly formed and original grain sizes:

$$d_{0_{i+1}} = d_{rex_i} \cdot X_i^{4/3} + d_{0_i}(1 - X_i)^2 \qquad (5.2)$$

With this formulation, when X_i is close to 1, the "initial" grain size for the following pass is $d_{rex\ i}$. On the other hand, if X_i is small, $d_{0\ i+1}$ will be close to the original grain size, $d_{0\ i}$; it only changes its shape because of the applied strain [36].

5.3.2 - Grain Growth After Recrystallization

After complete recrystallization, the microstructure is subjected to grain growth; this is driven by the decrease in free energy associated with the grain boundaries. The simplistic situation described above, however, is not applicable in some cases. Take a microstructure consisting of 90% recrystallized grains and 10% work hardened grains. The freshly formed grains will experience grain growth while the work hardened regions will still not be recrystallizing. Microstructures of this type are very common in rolled materials; thus, they must be treated in such a way as to provide a reasonable approximation of the overall behavior. For this reason, fractional softening equal to or greater than 95% is rounded to 100%; this can be considered to allow for grain growth [88].

For the group A and B steels, one single equation (Equation 2.69) was employed to describe grain growth. Although the above equation was derived for Nb steels, it is used here to describe grain growth in the multiply-alloyed steels as well. This is due to the lack of an equation for the multiply-alloyed grades and because the alloying elements present in the group B grades make it more reasonable to adopt an equation derived for Nb steels than one derived for the C-Mn grades. The grain growth kinetics in Nb and multiply-alloyed steels are of course expected to be slower than in plain C-Mn compositions due to solute drag. For the group C (C-Mn) steels, however, a group of equations is available to describe the grain growth. The method used here was proposed by Hodgson et al. [21,36,37] and is a "pragmatic" one, based on both laboratory [37] and industrial [36] observations.

It should be noted that there is a large difference between the rate of growth during the first second of the interpass interval and the remaining time. This difference may arise because of the large driving force for grain growth present in the initially fine grained structure; this is probably associated with the absence of strong microalloying element segregation, which later acts to retard grain boundary migration. Another possible effect concerns the presence of "deformation" vacancies immediately after rolling, which could accelerate growth [102]. This transition was handled by adopting different grain growth exponents for each stage [36]. However, the best solution would be to express the grain growth exponent as a function of time. From the analysis of hot strip rolling

schedules, there is another factor to be considered: when the interpass times are short (t_{ip}<1s and rapid growth occurs), the temperatures are low, a factor that retards grain growth. Of course, the grain growth equations have a temperature-dependent term, which compensates for this effect in the final passes.

The other interesting point for the C-Mn steels concerns the difference in behavior depending on whether SRX or MDRX softening precedes grain growth [37]. According to Hodgson et al. [21,37], after MDRX, the grain growth rate is slower compared to the growth rate after SRX. This effect is associated with the apparent activation energy for growth, which seems to depend on the previous recrystallization process. Although the effect is not clear from a physical point of view, some comments can nevertheless be made here. In the SRX process, grain growth begins at the nucleation stage and continues until impingement occurs at some point during the interpass time. Thus, during SRX, the grains are *initially* very small. When the nuclei are formed *during* deformation, however, the grains have already attained a certain size at the time MDRX takes place. Texture differences between the statically and dynamically-formed grains may also contribute to the growth rate difference. Certainly, further studies appear to be necessary to clarify this point.

The above analysis justifies the use of Equations 2.61 to 2.64 to describe grain growth in the C-Mn grades, at rates that depend on the interpass time and the mechanism of softening.

5.4 - Design of the Microstructure Prediction Spreadsheet

The above equations describing the microstructural events can now be organized into a spreadsheet. Basically, the spreadsheet parameters displayed in Figure 3.3 are used as input data to simulate the microstructural changes taking place during hot rolling, in a pass-by-pass analysis. The starting grain size (after roughing and before strip rolling) is adopted as 100μm for the C-Mn grades and 80μm for the others. The further grain sizes are calculated after recrystallization and grain growth, and the results constitute the input data for the next pass. Both the accumulated strain as well as the redundant strain are employed throughout the calculations. Some typical inputs and outputs of the microstructure evolution

spreadsheet are displayed in Figure 5.1. The example below uses data from the Dofasco HSM, grade CD.

INPUTS		Steel: CD			
pass	d_0* (μm)	T (°C)	$\dot{\varepsilon}$ (s^{-1})	t_{ip} (s)	ε**
F 1	100	1003	11.8	3.27	0.60
F 2	--	975	19.0	2.25	0.47
F 3	--	959	30.0	1.62	0.43
F 4	--	941	41.3	1.24	0.34
F 5	--	926	61.1	0.93	0.33
F 6	--	909	82.4	0.73	0.28
F 7	--	895	88.7	--	0.19

* estimated ** Includes the redundant strain.

OUTPUTS		Steel: CD									
pass	d_0 (μm)	ε_a	ε_c	$\varepsilon_a>\varepsilon_c$?	$\varepsilon_{0.5}$	X_{dyn}	$t_{0.5}$ (s)	X	d if X>0.95 (μm)	d after. t_{ip} (μm)	1000/T (K^{-1})
F1	100.0	0.60	0.44	Y	0.61	0.17	0.06	1.00	20.5	26.2	0.78
F2	26.2	0.47	0.35	Y	0.50	0.16	0.04	1.00	16.3	22.3	0.80
F3	22.3	0.43	0.38	Y	0.53	0.06	0.03	1.00	13.4	19.6	0.81
F4	19.6	0.34	0.42	--	--	--	0.12	1.00	21.8	29.0	0.82
F5	29.0	0.33	0.54	--	--	--	0.39	0.81	24.4	19.4	0.83
F6	19.4	0.34	0.54	--	--	--	0.22	0.9	19.2	16.9	0.85
F7	16.9	0.22	0.54	--	--	--	0.54	--	21.8	--	0.86

Figure 5.1 Spreadsheet calculation of grain size and fractional softening in steel CD, containing 0.06% C, 0.27% Mn, 0.007% P and 0.035% Al.

In C-Mn steels, mechanisms such as carbonitride precipitation followed by strain accumulation do not take place, so only DRX+MDRX effects are considered here. The observed MFS is calculated using the Sims formulation (from the mill data) Then, predictions are made using Equation 4.3, based on the Misaka equation. The observed and predicted MFS's are compared in Table 5.3, where the differences between the three sets of MFS's are also shown (in %).

Table 5.3 Comparison between the mill (Sims) MFS and the MFS values predicted according to the present modified Misaka equation (MFS^+) and the original equation. Steel: CD.

Pass	Temp (°C)	1000/T (K^{-1})	Sims MFS (MPa)	MFS^+ (MPa)	Difference (%)	Misaka MFS (MPa)	Difference (%)
F1	1003	0.78	113	118	4.8	134	18.6
F2	975	0.80	128	126	-1.1	143	11.5
F3	959	0.81	134	133	-0.3	154	14.8
F4	941	0.82	133	136	2.5	158	19.2
F5	926	0.83	143	147	2.3	171	19.4
F6	909	0.85	148	159	7.3	178	20.1
F7	895	0.86	165	152	-7.8	171	4.1

Finally, the mill (Sims) MFS, Misaka MFS and present modified MFS^+ are plotted versus 1000/T and compared in Figure 5.2. It can be seen that Misaka's equation clearly overpredicts the MFS, as already discussed above. By contrast, when the Mn correction is employed together with the allowance for DRX+MDRX, an excellent fit is observed.

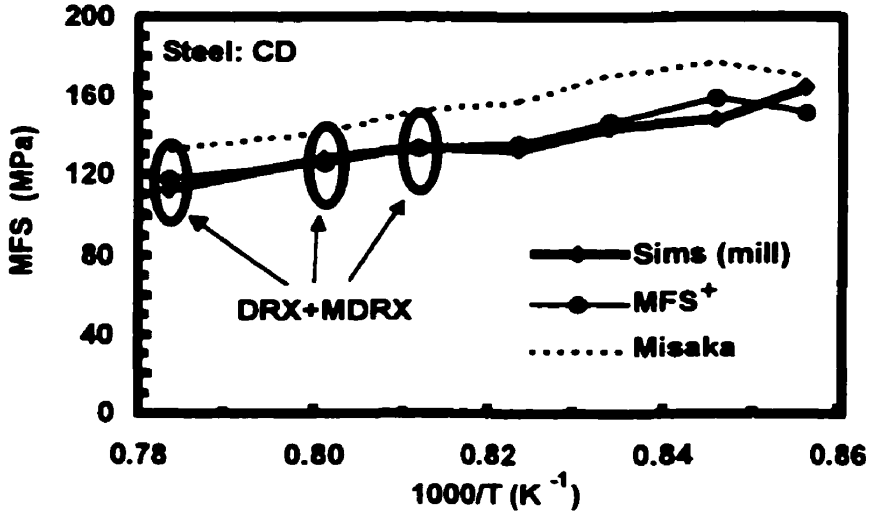

Figure 5.2 Two sets of MFS predictions compared with the mill log-based values for grade CD.

Note that, even with postdynamic softening occurring subsequent to passes 1 to 3, the MFS slope is still positive because of the decreasing temperature. The present modified Misaka equation (labeled as MFS^+) has a considerably better

overall fit to the mill MFS curve than the original Misaka relation. Nevertheless, in the last pass, MFS^+ is somewhat lower than the Sims MFS. This trend was observed in most of the mill logs analyzed here and has been reported and discussed in the literature [103]. The discrepancy has been attributed to an overestimation of the MFS by the Sims equation when small reductions are involved. This is because the steady-state stress was employed in the derivation of the relationship. The steady-state stress does not apply to small reductions because of the limited contribution of work hardening. As the last pass usually involves a light reduction (especially the last two passes), they are subject to this effect.

The "basic" version of the prediction spreadsheet described above, allowing for strain accumulation and DRX+MDRX, is considered to be fully applicable to the group C (C-Mn) grades. However, for Nb steels, the critical strain for the initiation of DRX must be accurately known, and the evolution of this quantity seems to be quite controversial in the literature. The determination of the precipitation-start time during hot strip rolling is another point of discussion as well. Therefore, in the next two chapters, some improved methods for the estimation of these two parameters will be proposed and described for the Nb grades.

Chapter 6 - Modeling the Critical Strain for the Initiation of DRX in Nb Steels

During the hot strip rolling of steels, the rapid softening and intense grain refinement caused by DRX in a particular pass can considerably modify the load behavior in the following stand. Furthermore, once DRX is initiated, softening by means of metadynamic recrystallization (MDRX) will also take place during the interpass interval, as long as sufficient time is available for this mechanism to make a contribution as well.

The critical strain for the onset of dynamic recrystallization is an important parameter employed in the mathematical modeling of microstructure evolution and of rolling load. Knowledge of the critical strain for the initiation of DRX is a requirement for prediction of the operating softening mechanisms in hot working processes.

For the present purpose, it is useful to express the critical strain for DRX (ε_c) as a function of the peak strain (ε_p), as determined from a stress-strain curve. This is because some equations are already available to specify the peak strain as a function of the initial grain size, temperature and strain rate for Nb steels [25,30,104]. Such an approach can then be used to predict the operating recrystallization mechanism, which can be SRX, or DRX followed by MDRX, or some combination of these two static softening mechanisms.

The peak strain ε_p usually increases with the Zener-Hollomon parameter [15] and so does ε_c. At high Z values, the stress peak that characterizes DRX softening becomes less sharp. By continuously increasing Z, ε_c may approach ε_p, leading to the

absence of a peak; if ε_c reaches ε_p, there will be no DRX [105]. In the case of a HSM, the Z values are kept roughly constant by increasing the strain rates and decreasing the temperatures. The $\varepsilon_c/\varepsilon_p$ ratio can therefore be considered to be approximately constant throughout the schedule.

The $\varepsilon_c/\varepsilon_p$ ratio is usually taken as 0.8 for plain C-Mn steels. However, previous workers have reported lower values for Nb steels, as mentioned in section 2.2.4. In the present work, the ratio is considered to be a function of Nb content and was determined from the hot strip mill logs as follows. This led to an equation that expresses the critical strain for Nb steels as a function of the peak strain. The grades studied in the present chapter cover the composition range from 0.008 to 0.058% Nb, which represents most of the conventional Nb level range (see Table 6.1).

Table 6.1- Chemical compositions of the steels.

Steel	C	Mn	Si	Nb
AD9	0.06	0.45	0.01	0.008
AD10	0.06	0.65	0.01	0.008
AD1	0.06	0.65	0.12	0.020
AD2	0.14	0.65	0.23	0.020
AD3	0.12	0.85	0.23	0.020
AD4	0.12	1.0	0.23	0.020
AS1	0.07	1.12	0.05	0.023
AD5	0.06	0.65	0.12	0.030
AD6	0.06	0.65	0.01	0.030
AB	0.11	1.05	0.01	0.031
AA1	0.05	0.35	0.01	0.035
AS2	0.09	1.33	0.06	0.036
AD7	0.06	0.65	0.12	0.045
AD8	0.06	0.65	0.01	0.045
AA2	0.05	0.70	0.10	0.053
AA3	0.06	0.70	0.11	0.058

For each pass, ε_c was compared to the accumulated strain and a decision was made concerning the operative softening mechanism (if $\varepsilon_a > \varepsilon_c$, DRX occurs; if $\varepsilon_a < \varepsilon_c$, SRX occurs). In this analysis, the critical strain ratio, $\varepsilon_c/\varepsilon_p$, was adjusted to provide the best fit between the MFS's calculated from the mill forces and the ones predicted by the model. Note that, at the present stage, this model does not take into account the

occurrence of strain-induced precipitation. The equation used to describe the critical strain is shown below:

$$\varepsilon_c = C\,\varepsilon_p \tag{6.1}$$

6.1 - The Peak Strain Equation

The peak strain equation for a steel containing 0.039% Nb was taken from Reference [30]. It takes into account the effects of strain rate, initial grain size and temperature:

$$\varepsilon_p = 2.8\times10^{-4} d_0^{0.5}\left[\dot{\varepsilon}\cdot\exp\left(\frac{375000}{RT}\right)\right]^{0.17} \tag{6.2}$$

Additional torsion tests were performed in this investigation in order to take the Nb content into account. For this purpose, grades AS1, AS2 and AA1 were tested under single pass conditions, at $5s^{-1}$ and 850 to 1000°C, according to the method illustrated in Figure 3.5. The results are displayed in Figures 6.1 to 6.3. From these data, a correction factor for the effect of Nb solute drag on the peak strain permitted Equation 6.2 to be modified as follows:

$$\varepsilon_p = \frac{(1+20\,[Nb])}{1.78}\times 2.8\times10^{-4} d_0^{0.5}\left[\dot{\varepsilon}\cdot\exp\left(\frac{375000}{RT}\right)\right]^{0.17} \tag{6.3}$$

The dependence of the peak strain on temperature is shown in Figure 6.4, together with two curves based on Equation 6.3 and data from Roucoules et al. [30].

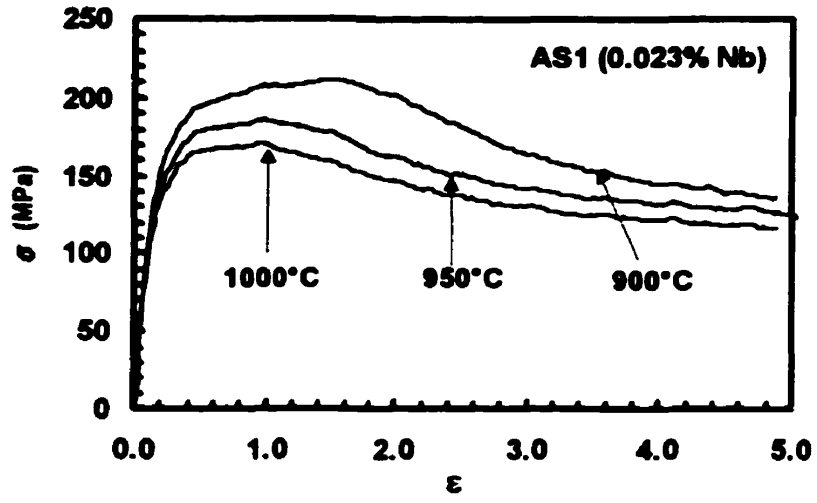

Figure 6.1 Single-pass torsion tests at 900, 950 and 1000°C and a strain rate of $5s^{-1}$; grade AS1 .

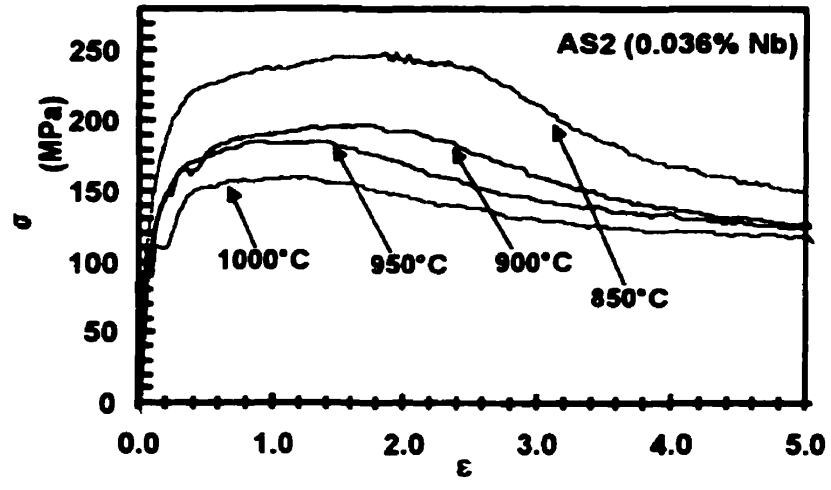

Figure 6.2 Single-pass torsion tests at 900, 950 and 1000°C and a strain rate of $5s^{-1}$; grade AS2 .

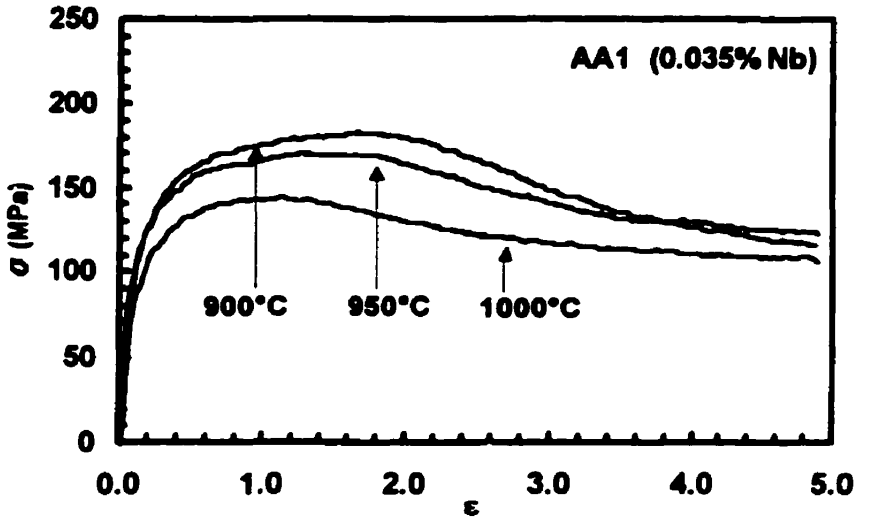

Figure 6.3 Single-pass torsion tests at 900, 950 and 1000°C and a strain rate of $5s^{-1}$; grade AA1 .

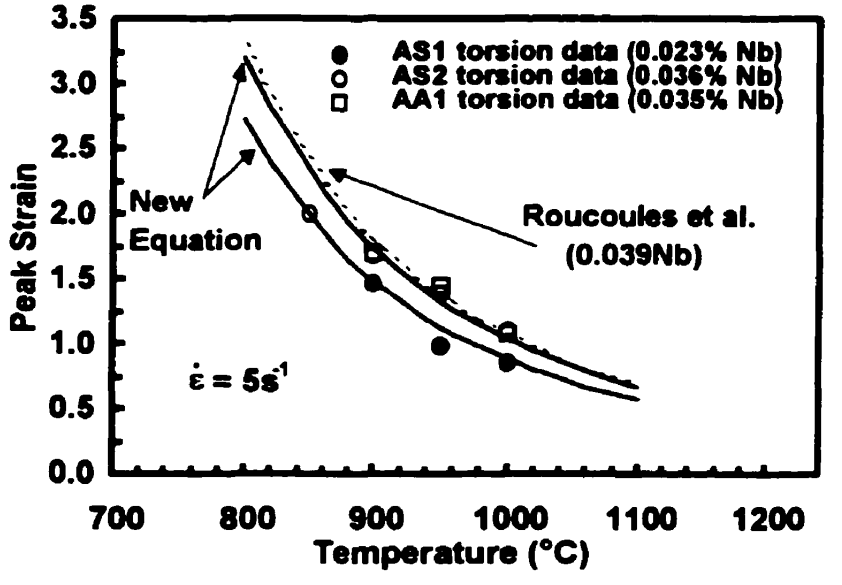

Figure 6.4 Dependence of the peak strain on temperature for steels AA1, AS1 and AS2 as well as data from Roucoules et al. [30].

6.2 - Modeling the $\varepsilon_c/\varepsilon_p$ Ratio

Each mill log analysis resulted in an MFS figure, with the "measured" and "predicted" MFS's plotted as functions of the inverse absolute temperature. There is a corresponding optimum C value, where $C = \varepsilon_c/\varepsilon_p$, for each strip analyzed. The following plots are examples of this type of MFS modeling. The AD4 grade (0.020% Nb) MFS curve is illustrated in Figure 6.5; this fit was obtained by adopting a value of C = 0.66. No load drops were observed, suggesting that DRX+MDRX did not take place in this case. In Figure 6.6, however, the AB grade (0.031% Nb) MFS curve was fitted with C = 0.58, and both load drops, observed after passes 2 and 4, are now predicted by the microstructure model (based on MFS$^+$) presented in Chapter 5. This observation provides strong evidence for the view that DRX+MDRX has occurred. These C values, found by testing several alternative possibilities, were then plotted in Figure 6.7 as a function of Nb content for the whole range available. It can be seen that the higher the Nb content, the lower the $\varepsilon_c/\varepsilon_p$ ratio. Beyond 0.05% Nb, the C factor approaches a value of around 0.4 according to this analysis. This approach was applied to more than 100 mill logs for the finish rolling of the compositions listed in Table 6.1. The method described above can, however, be repeated and employed on other families of steels, using peak strain equations that can readily be found in the literature.

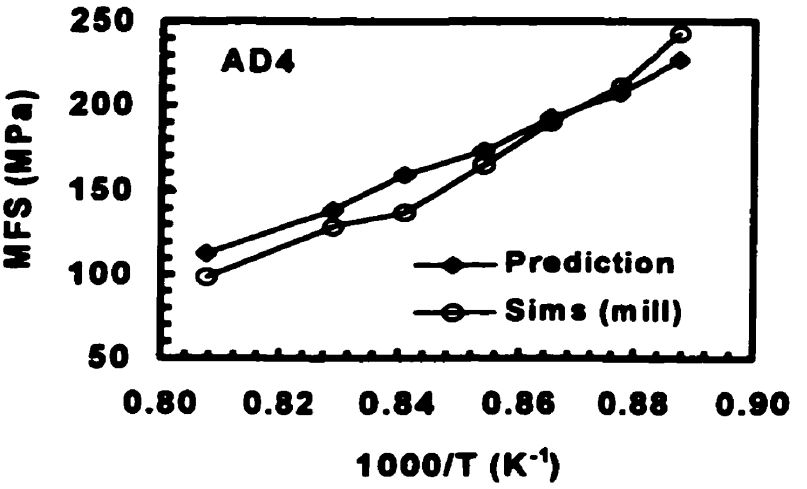

Figure 6.5 MFS predictions for the Dofasco AD4 grade, showing no evidence for DRX.

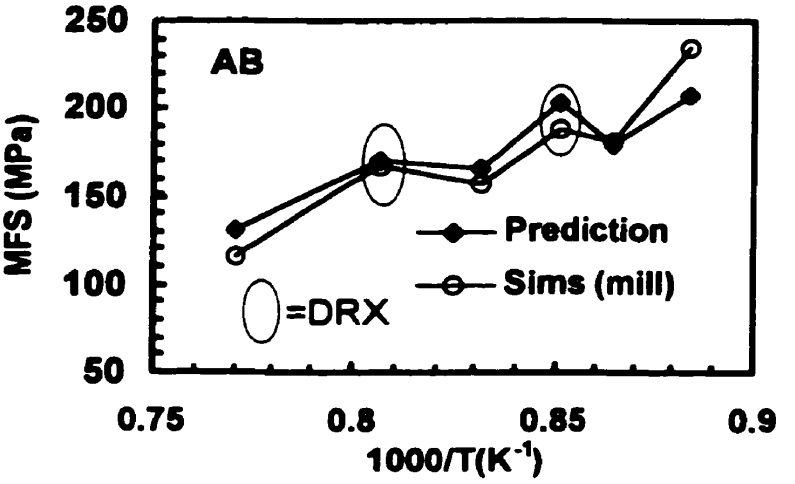

Figure 6.6 MFS predictions for the B1 grade. Here DRX is considered to occur in passes 2 and 4, followed by MDRX.

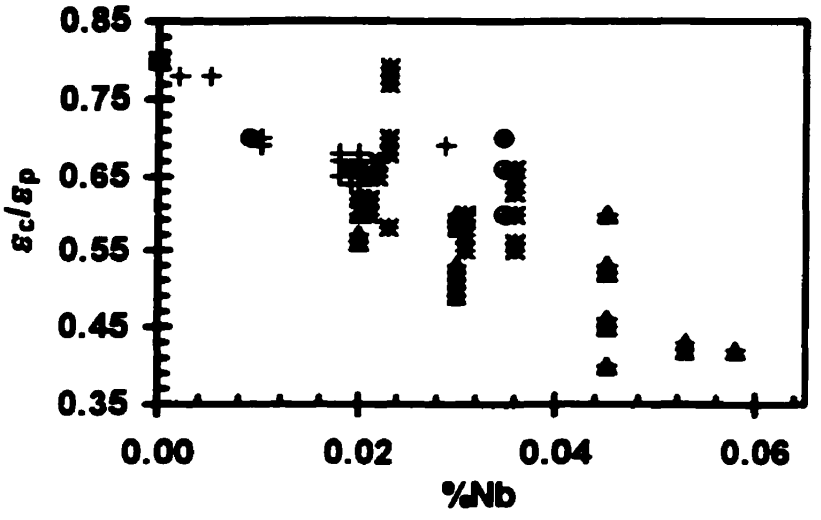

Fig. 6.7 Initial diagram of the dependence of $\varepsilon_c/\varepsilon_p$ on Nb concentration.

The effect of Nb on the stress-strain curve is to increase the stress at a particular strain. Concurrently, the peak strain is moved to higher values. Experimental stress-strain curves derived from torsion tests show this effect, see Fig. 6.8. In this case, the AA1 (0.035%Nb) and CA grades were tested together. Both steels have the same base composition, except for Nb. The peak strain increases with Nb addition more rapidly than the critical strain, as a result of which the $\varepsilon_c/\varepsilon_p$ ratio decreases when the Nb concentration is increased. This suggests that the solute drag due to the presence of Nb has less influence on ε_c than on ε_p (and therefore on nucleation as opposed to growth). According to this analysis, the critical strain appears to be almost independent of the alloying element concentration. It does not change abruptly for different chemical compositions of the most common carbon steels. The peak strain, on the other hand, is strongly influenced by the presence of alloying elements, because it is determined by the softening kinetics associated with DRX; this mechanism first balances and then overcomes the work hardening. As DRX basically involves the migration of grain boundaries, the addition of Nb, which has a strong solute drag effect, retards the rate of grain boundary motion, shifting the peak to the right hand side (higher strains). To a lesser extent, other elements, such as Mn and Si, also have their drag effects.

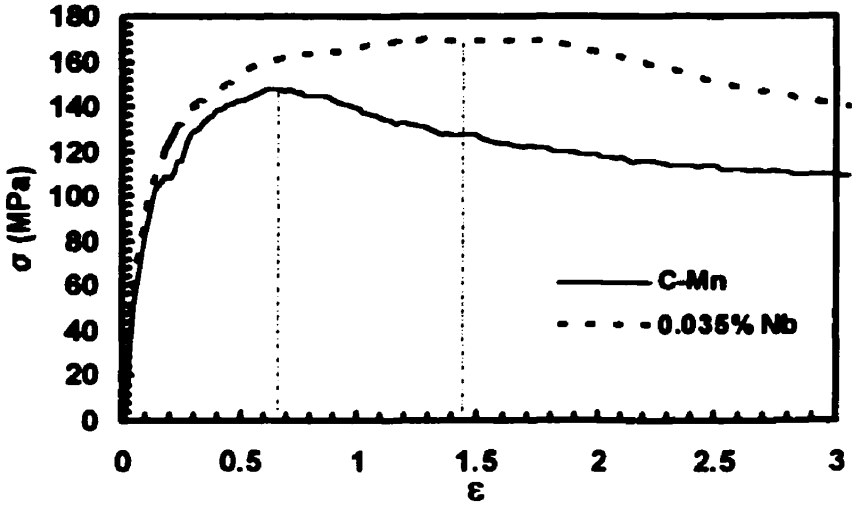

Fig. 6.8 Effect of Nb addition on the stress-strain curve of a low carbon steel at 950°C and a strain rate of $5s^{-1}$ (grades AA1 and CA tested under the same conditions).

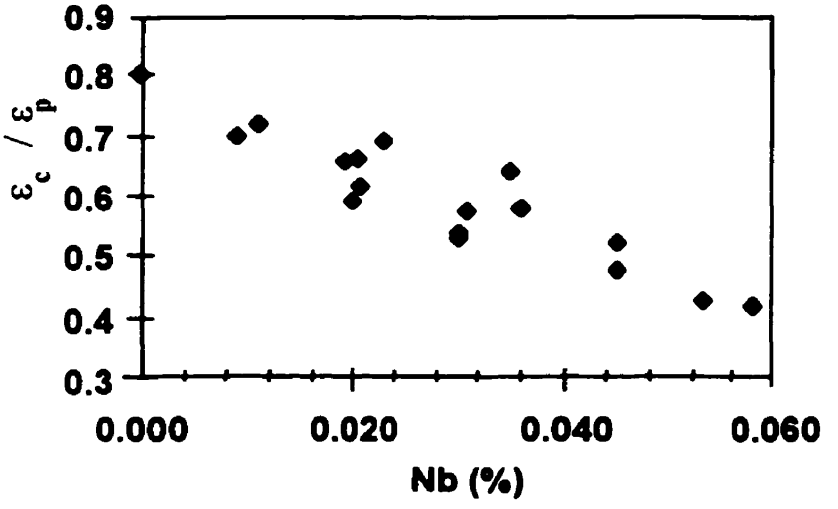

Fig. 6.9 Mean values of the $\varepsilon_c/\varepsilon_p$ ratio (obtained from mill logs) plotted against the Nb content.

In order to minimize the spread associated with industrial data, the $\varepsilon_c/\varepsilon_p$ values were averaged for each grade before plotting, see Fig. 6.9. This diagram illustrates more clearly the dependence of the $\varepsilon_c/\varepsilon_p$ ratio on Nb content. These points, however, still display some scatter. The effects of Mn and Si addition were therefore included in the analysis and the following equation was derived [106]:

$$\varepsilon_c / \varepsilon_p = 0.8 - 13\,[Nb_{eff}] + 112\,[Nb_{eff}]^2 \tag{6.3}$$

where:

$$Nb_{eff} = [Nb] - \frac{[Mn]}{120} + \frac{[Si]}{94} \tag{6.4}$$

When the data of Fig. 6.9 are replotted with the aid of this equation, the relationship between $\varepsilon_c/\varepsilon_p$ and the concentrations of Nb, Mn and Si becomes more evident, as shown in Fig. 6.10. The original uncorrected points are represented by the open squares. Plotting the $\varepsilon_c/\varepsilon_p$ ratio against the *effective* Nb concentration (Equation 6.4) results in a clear relationship. Eqs. 6.3 and 6.4 are considered to apply over the following composition ranges: [Nb] 0.010 to 0.058%, [Mn] 0.35 to 1.33% and [Si] 0.01 to 0.23%. They describe the progressive decrease in $\varepsilon_c/\varepsilon_p$ ratio represented by the line in Fig. 6.10.

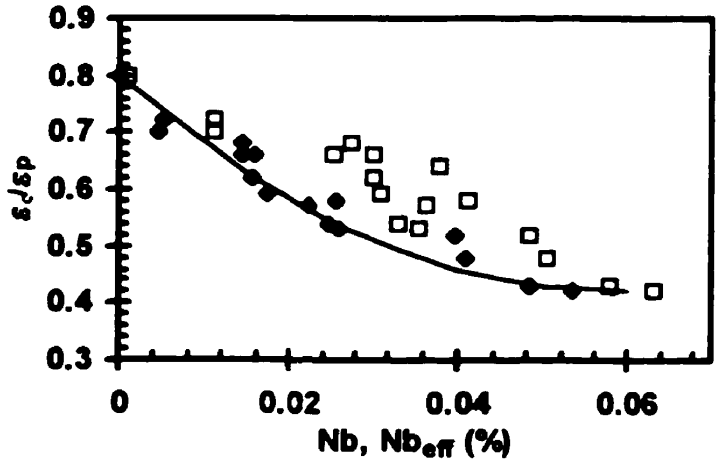

Fig. 6.10 Dependence of $\varepsilon_c/\varepsilon_p$ ratio on *effective* Nb concentration as calculated from Equations (6.3) and (6.4). The unmodified points are represented by the open squares and plotted solely against [Nb].

6.3 - Discussion

The drag force due to solute elements is usually associated with differences in atomic radius between solute and solvent. The stress fields generated when a "strange" atom is located at a grain boundary are lower than when the same atom is located in the matrix. In order to keep the stress fields as low as possible, solute atoms tend to follow a moving grain boundary, exerting a drag force on its migration. The larger the atom, the stronger the drag force. In the present case, the atomic radius ratios of the elements involved are: $R_{Nb}/R_{Fe} = 1.15$, $R_{Mn}/R_{Fe} = 0.90$ and $R_{Si}/R_{Fe} = 0.94$. Nb is the most effective among the three elements analyzed here because other considerations, such as modulus differences and electronic interactions, also play a role.

At the start of this analysis, the solute effects were expected to be all positive, i.e. all additions were expected to increase ε_p. However, it can be seen from Eq. 6.4 that the influence of Mn addition is opposite in sign to that of Nb and Si. This indicates that Mn is not making a *direct* contribution to solute drag, but may be exerting, with Si, an indirect effect. A rationalization for the present observations can be based on the report that Mn addition *decreases* the diffusivity of Nb in austenite while the addition of Si *accelerates* Nb diffusivity [107]. Furthermore, it has been shown that Mn in solution has an almost negligible direct solute drag effect on the migration of grain boundaries [108].

The explanation proposed here can be understood more clearly by referring to Fig. 6.11. Here, the dependence of the solute drag force on grain boundary velocity attributable to Nb diffusion (in Fe) is represented by the full line. When the diffusivity of Nb is increased, as occurs in the presence of Si, the Nb solute drag curve shifts to the right, as indicated by the thin line. By contrast, when the diffusivity of Nb is decreased, as attributable to the addition of Mn, the Nb solute drag curve shifts to the left, as illustrated by the broken line.

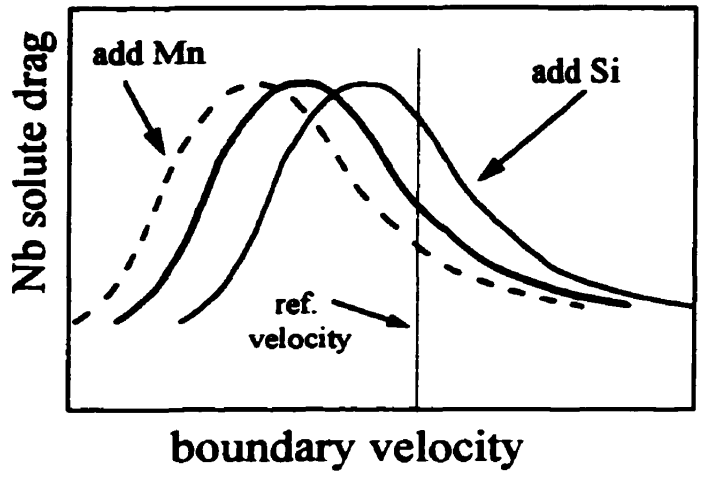

Fig. 6.11 Effect of boundary velocity on the Nb solute drag exerted on a boundary. The indirect influences of Mn and Si addition are shown schematically.

The influence of adding Si and Mn on the solute drag *attributable to the presence of Nb* can now be deduced with reference to the vertical line that represents a particular grain boundary velocity to the right of the peak, i.e. higher than that associated with the maximum in the drag force. (Most practical examples of solute drag are found to the right of the peak, after normalization of the curve for the diffusivity [108].) It can be seen that the addition of Si *increases* the solute drag with respect to the single addition of Nb, while the addition of Mn has the contrary effect.

According to the above scenario, the decrease in the Nb diffusivity and Nb solute drag associated with Mn addition decreases ε_p (and consequently increases $\varepsilon_c/\varepsilon_p$). On the other hand, when unusually low concentrations of Mn are present, the Nb diffusivity and solute drag are increased, slowing down the rate of softening by DRX and increasing ε_p (i.e. decreasing the $\varepsilon_c/\varepsilon_p$ ratio). This phenomenon can be observed in the work of Akben et al. [48], where a Nb HSLA steel containing 1.90%Mn displayed a lower peak strain than a similar grade that only contained 1.25%Mn. It is important to note here that the influence of Mn addition is only a secondary effect compared to that of Nb and is only observed because it appears to moderate that of Nb.

With regard to the *relative* effects, that of Nb is clearly the greatest, followed by that of Si and then by Mn, in a ratio of 120:1.3:1, respectively. However, due to the relatively high concentrations of Mn and Si generally employed compared to Nb, the *practical* effects on $\varepsilon_c/\varepsilon_p$ are represented by the ratio 13.5:1:2.6, for example, for a steel containing 0.03% Nb, 0.2% Si and 0.7% Mn. The weak effects of Mn and Si on ε_p as well as on austenite strengthening are due to the similarities in their atomic diameters in comparison with Fe.

Chapter 7 - Modeling the Precipitation Behavior of Niobium Steels

A mathematical model that simulates the occurrence of strain-induced precipitation during the hot strip rolling of Nb microalloyed steels is described in this chapter. This model was derived from the rolling schedule data on the basis of the type of mean flow stress analysis reviewed above. Nb microalloyed grades containing Si levels ranging from 0.01 to 0.23 wt% and Mn levels ranging from 0.35 to 1.33% were considered. The aim of this work was first to determine whether strain-induced precipitation does indeed influence the MFS behaviour under industrial strip (as opposed to plate) rolling conditions. The occurrence of precipitation can preclude both static and dynamic recrystallization; in this way, it can also prevent metadynamic softening from taking place [20]. A second objective was to estimate the influence of Mn and Si concentration on the kinetics of Nb(C,N) precipitation. In order to test these hypotheses, the Sims mean flow stresses pertaining to each pass were compared with the predictions obtained from the mathematical model for the MFS in Nb steels presented in Chapters 4, 5 and 6. Here, these relations are modified to take the precipitation kinetics into account.

7.1-Selecting a Precipitation Model

Here the view is taken that the rolling force during hot strip rolling can be affected by the occurrence of strain-induced precipitation, which can play an important role in Nb steels. It is well known that recrystallization can be suppressed by the

formation of such precipitates. In Chapter 2, two of the models available in the literature were presented. Both of these predict the precipitation-start time in the austenite phase. The Dutta and Sellars [49] model was employed in the present study because all the coefficients are available; also, because of its simplicity, it is relatively easy to perform modifications. The need for accurate physical parameters in the Park and Jonas model [54], which change when the chemistry is changed, made its use impractical for the present study.

As mentioned in section 2.2.9, the DS model was derived by fitting experimental data published by various authors, who used a wide range of chemical compositions. The effects of Mn and Si on precipitation were not taken into account in the DS model, although the influences of Mn and Si on the solubility of NbC and NbN [46-47], on Nb diffusion in austenite [107], and on the precipitation of Nb(C,N) [48] (the effect of Mn only) had already been published. According to the studies mentioned above, Mn increases the solubility of NbC and NbN, decreases Nb diffusivity and retards the rate of precipitation of Nb(C,N). On the other hand, Si decreases the solubility of NbC and NbN, increases the carbon activity in austenite (a well-known effect in cast irons), and increases the diffusivity of Nb in austenite. Thus, Si *accelerates* the precipitation kinetics of Nb(C,N).

Other precipitation models are available in the literature [109,110], but none of them was considered suitable for this study.

7.2-Modification of the Spreadsheet to Permit Prediction of the Precipitation-Start Time

The computer spreadsheet described in Chapter 5 was used to calculate the precipitation-start times, using the additivity rule presented in section 2.2.9. The procedure employed can be deduced from the spreadsheet displayed in Figure 7.1. This approach assumes that no further softening takes place once precipitation has begun, neither by SRX nor by DRX+MDRX; i.e. that the situation is comparable to the cessation of recrystallization when plate rolling is carried out below the T_{nr}. The short time that the steel stays in the hot strip mill (usually about 6 to 7 seconds for all passes) makes this assumption reasonable.

The method simply calculates the precipitation-start times by inputting the

A	B	C	D	E	F	G	H	I	J	K	L	M
pass	d_0 (mm)	T(°C)	$\dot{\varepsilon}$ (s^{-1})	t_{ip} (s)	Z	k_s	t_{ps} (s)	Sum tip/tps	PPTN?	ε_a	ε_c	DRX? $\varepsilon_a>\varepsilon_c$?
F1	80.0	1008	16.4	3.26	3.28E+16	5.44	11.131	0.29	No	0.92	1.03	–
F2	66.0	976	35.0	1.85	1.72E+17	7.42	2.780	0.96	No	1.28	1.24	Y
F3	15.9	960	63.1	1.18	4.95E+17	8.73	3.680	1.28	Y	0.55	0.73	–
F4	15.9	948	113.2	0.76	1.27E+18	9.88	1.228	1.90	Y	1.05	0.85	–
F5	15.9	930	148.7	0.50	2.91E+18	11.96	0.706	2.61	Y	1.32	0.98	–
F6	15.9	915	194.5	0.39	6.10E+18	14.09	0.464	3.44	Y	1.56	1.12	–
F7	15.9	901	225.6		1.11E+19	16.48	0.333	3.44	Y	1.72	1.24	–

Figure 7.1 Section of the spreadsheet modified to take the effect of precipitation on the microstructure into account (see text for details).

data available into the DS equation. Once the t_{ip} and t_{ps} times are known (columns E and H, respectively), the additivity rule is applied, according to Equation 2.78. This is shown in the column identified by the heading "Sum" (column I). Precipitation is considered to start once the sum of all the t_{ip}/t_{ps} ratios reaches 1. In order to calculate the *exact* precipitation start time, P_s, the total time elapsed up to pass n-1 is added to the *fractional* interpass time associated with pass n, $t_*^{ip(n)}$, that permits the sum of the ratios to attain a value of 1. It is therefore defined by the three relations that follow:

$$P_s = (\text{total time up to pass } n-1) + t_*^{ip(n)} \tag{7.1}$$

According to the additivity rule, precipitation occurs when Equation 2.78 is satisfied:

$$\sum_{i=1}^{n-1} \frac{t_i^{ip}}{t_i^{ps}} + \frac{t_*^{ip(n)}}{t_n^{ps}} = 1 \tag{7.2}$$

The time required to complete the summation is therefore described by:

$$t_*^{ip} = \left(1 - \sum_{i=1}^{n-1} \frac{t_i^{ip}}{t_i^{ps}}\right) \cdot t_n^{ps} \tag{7.3}$$

Softening is allowed to take place after pass n up to the precipitation-start time defined by $t_*^{ip(n)}$, where it should be noted that $t_*^{ip(n)}$ is less than t_n^{ip}.

In the spreadsheet displayed in Figure 7.1, precipitation occurred after the third pass. The occurrence of DRX (column M), however, depends not only on the critical (column L) and accumulated (column K) strains, but also on the absence of strain-induced precipitation. Note that in the final passes, the critical strain is less than the accumulated strain, but, according to the assumptions of the present model, the presence of precipitates does not allow any type of recrystallization to occur. With the aid of this approach, the modifications that were required to allow for the occurrence of strain-induced precipitation, as well as for the influence of the Mn and Si levels on the kinetics of precipitation, were investigated as described below. It should be added that the occurrence of austenite strengthening by strain-induced precipitation is not considered here, firstly because the precipitates are subject to coarsening at hot rolling temperatures and secondly because they are not as fine as the precipitates formed in ferrite during coiling, which have a significant strengthening effect at low temperatures.

7.3-The Solubility Product of Nb Carbonitrides

The solubility of Nb carbonitride (referred to here as Nb(C,N)) is a key factor determining the chemical driving force for precipitation. The parameter K_S, displayed in Eq. 2.70, represents the "supersaturation ratio" for precipitation. Basically, it indicates the ratio between amounts of Nb, C and N in solution at the reheating temperature and at the pass temperature. The solubility equation derived by Irvine et al. [53], which has been used in several applications, is shown below. Note that the equation is written for the "equivalent carbon content" = C + $^{12}/_{14}$ N.

$$\log[Nb]\cdot\left[C+{}^{12}\!/_{14}N\right]=2.26-\frac{6770}{T} \qquad (7.4)$$

This equation was derived for a steel containing 0.6% Mn and 0.3% Si. As discussed above, the separate influences of Mn and Si will now be deduced from the published data listed in Table 7.1:

Table 7.1 **Published data for the solution temperature of Nb carbonitride.**

Author	C	Mn	Nb	Si	T_{sol} (°C)
Irvine et al. [53]	0.10	0.60	0.03	0.30	1098
Meyer [111]	0.06	1.20	0.035	0.07	926
Akben et al. [48]	0.05	0.42	0.035	0.25	1026
	0.05	1.25	0.035	0.27	996
	0.06	1.90	0.035	0.26	990
Johansen et al.[112]	0.06	0.01	0.035	0.01	1045
Kazinsky et al. [113]	0.06	1.00	0.035	0.35	1072

By using Equation 7.4 as a standard and the published data of Table 7.1, the following improvement was derived. It takes the effects of the Mn and Si concentrations into account:

$$\log [Nb]\cdot[C+{}^{12}/_{14}N] = 2.26 + \frac{838\,[Mn]^{0.246} - 1730\,[Si]^{0.594} - 6440}{T} \qquad (7.5)$$

The measured solution temperatures are compared against those predicted by the above relation in Figure 7.2. Here, it can be seen that the points follow the trend that takes the effects of Mn and Si into account (the one point off the line is due to Johansen et al. [112] and was essentially for a pure iron and not a steel). The above equation will therefore be employed in all the calculations that follow.

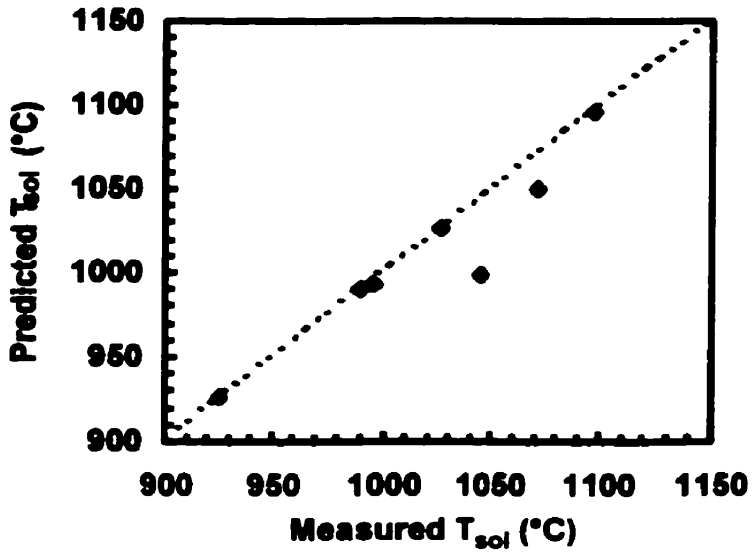

Figure 7.2 Comparison of predicted (Equation 7.5) and published solution temperatures for the steels listed in Table 7.1.

7.4-Modification to the DS Model

An important modification suggested by Bai [41] concerns the constants A and B of the DS equation. In the present work, the expression for the constant A suggested by Bai will be modified to allow for the effects of Mn and Si. Although the constant A has no physical meaning, it does depend on the chemical composition, or at least on the presence of elements that influence Nb mobility (i.e. the diffusivity) in austenite. As already discussed above, Si and Mn affect the diffusivity of Nb and, therefore, the critical number of nuclei per unit volume (N_C^*). This latter is included in the A constant according to the derivation of the DS equation.

The best overall fit was obtained by incorporating the dependence on exp(Nb/C) suggested by Bai together with a multiplying factor that depends on the Mn/Si ratio. The correlation found, with considerable spread, is illustrated in Figure 7.3. The expression that describes this behaviour follows:

$$A = \frac{\left(\frac{Mn}{Si}\right)^{0.42} \exp\left(\frac{0.42Nb}{C}\right)}{169400} \qquad (7.6)$$

The accuracy of the above expression is illustrated in Figure 7.4, where the "observed" values are taken from the mill log analysis.

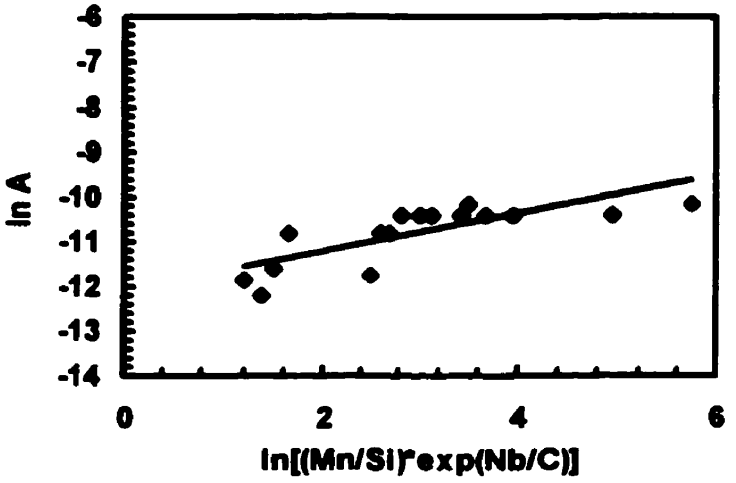

Figure 7.3 Correlation between the coefficient A and the C, Mn, Si and Nb contents.

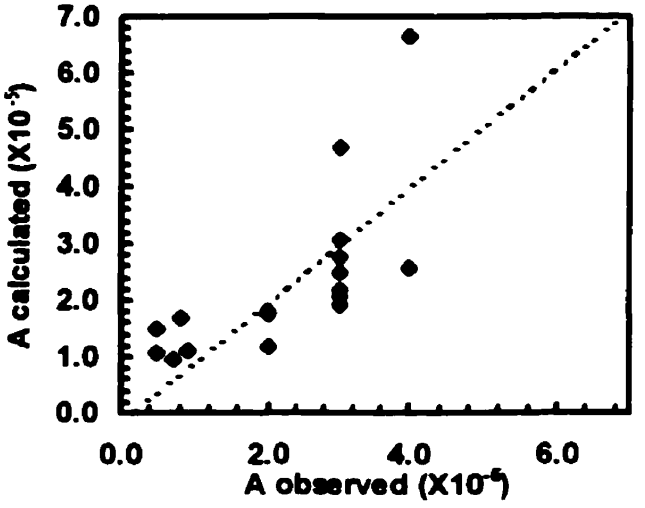

Figure 7.4 Accuracy of Equation 7.6.

In addition to the chemical composition, the previous processing history will also influence t_{ps}, according to the study of Valdez and Sellars [51]. The occurrence of strain-induced precipitation during roughing will decrease the driving force during

finishing, delaying precipitation. This factor can explain part of the large spreads observed during the analysis of strip mill logs. These spreads are minimized if the data from a single hot strip mill are used, suggesting that roughing has considerable influence on the t_{ps}.

The precipitation kinetics depend not only on the parameters of finish rolling, but also on the reheat temperature and the characteristics of the roughing schedule. These two factors were not analyzed in the present study and a more detailed survey will be necessary to take these further factors into account. The improvements described here can nevertheless be considered a good starting point for future work on these problems.

7.5-Application of the Precipitation Model to the Analysis of Strip Mill Logs

In the following pages, the mill logs pertaining to the group A grades will be tested with the improved DS equation. The precipitation start point will be indicated with an arrow on the plots of MFS as a function of inverse absolute temperature. Some grades, such as the ones that contain high levels of Mn, show no evidence for the occurrence of precipitation.

The results pertaining to the AS1 and AS2 grades (low Si and high Mn) are illustrated in Figures 7.5 and 7.6, respectively. According to the present model, precipitation is suppressed during strip rolling in this case, because it is significantly delayed by the high Mn content. The conditions for the initiation of strain-induced precipitation were not reached during passage through the mill. In Figure 7.6, MFS drops are observed at passes 4 and 6, indicating the occurrence of DRX in passes 3 and 5, followed by MDRX. If no allowance is made for DRX (and MDRX) in the model (broken line), the predicted MFS values are clearly too high. Similar remarks apply to the data for the AB grade (also low Si and high Mn), as can be seen in Figure 7.7. The retardation of strain-induced precipitation permitted DRX to occur in passes 2 and 4, followed by load drops in passes 3 and 5.

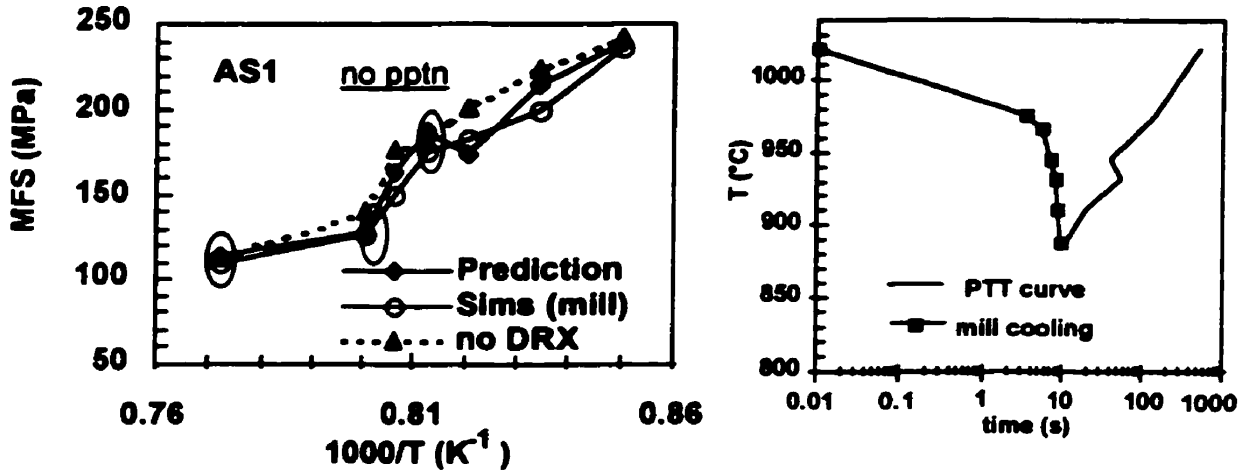

Figure 7.5 (a) Comparison of MFS predictions and observations for the AS1 grade. The prediction indicates that precipitation does not take place during the schedule. As a result, DRX is considered to occur during the first, second and fourth passes, followed by MDRX. (b) Comparison of precipitation-start curve with mill cooling curve. According to the present analysis, precipitation does not occur.

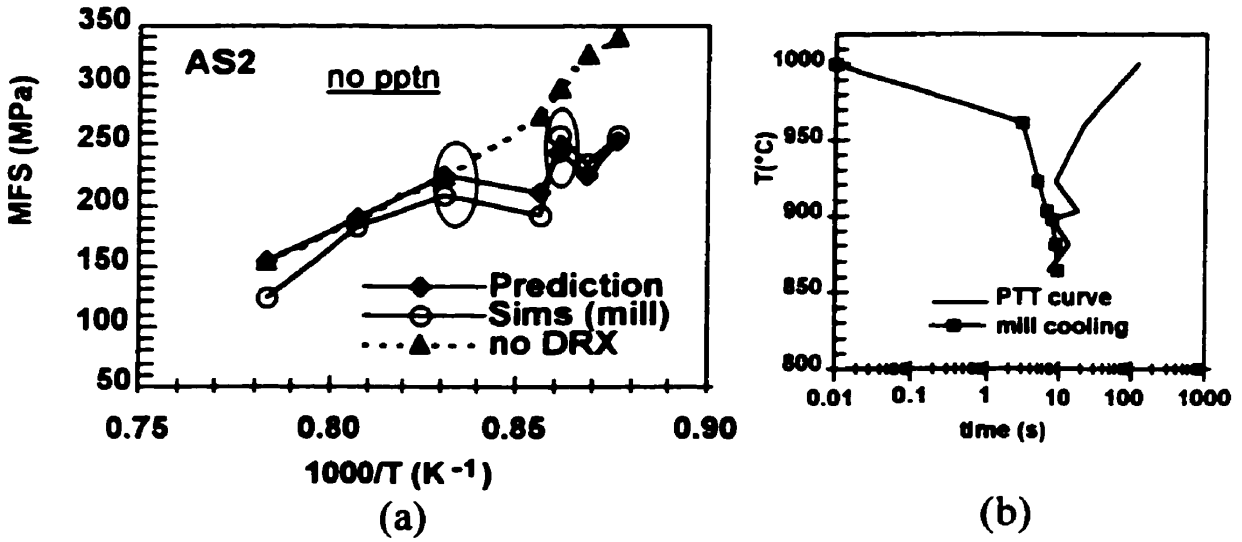

Figure 7.6 (a) Comparison of MFS predictions and observations for the AS2 grade. The prediction indicates that precipitation does not take place during the schedule. As a result, DRX is considered to occur during the third and fifth passes, followed by MDRX. (b) Comparison of precipitation-start curve with mill cooling curve. According to the present analysis, precipitation does not occur.

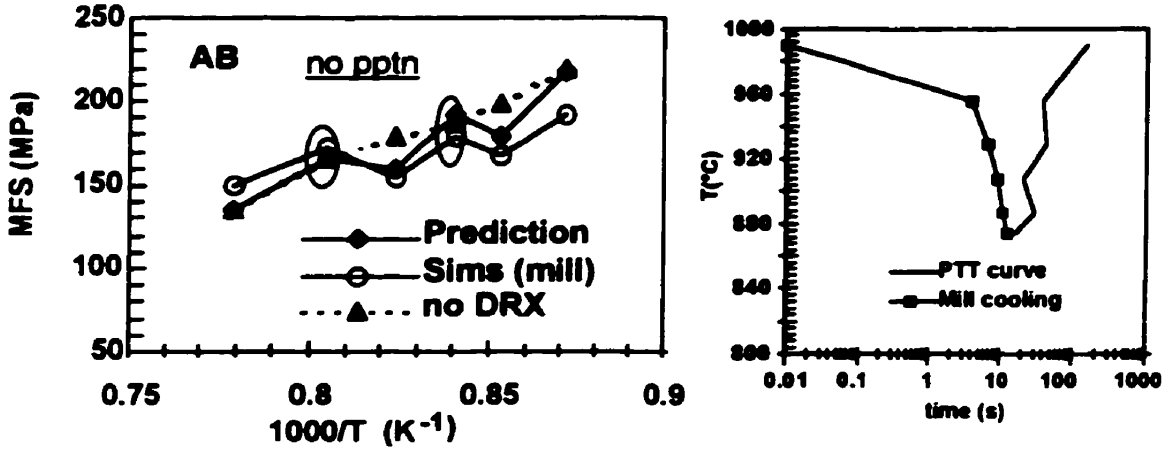

(a) (b)

Figure 7.7 (a) Comparison of MFS predictions and observations for the AB grade. The prediction indicates that precipitation does not take place during the schedule. As a result, DRX is considered to occur during the second and fourth passes, followed by MDRX. (b) Comparison of precipitation-start curve with mill cooling curve. According to the present analysis, precipitation does not occur.

The results pertaining to the AD5 (high Si, medium Mn) grade are illustrated in Figure 7.8. The drop in measured MFS after the second pass is consistent with the initiation of DRX during the second pass, followed by MDRX, as predicted by the model. If no allowance is made for DRX and MDRX (broken line), the predicted MFS values are clearly too high. The occurrence of strain-induced precipitation between passes 2 and 3 leads to an increase in the MFS values. The behaviour of a lower Si version of this steel, AD6, is presented in Figure 7.9. This grade displays a shallower MFS curve, where the drop in MFS after the second pass is again predicted by the model as resulting from DRX. However, in contrast to the previous case, precipitation is delayed slightly due to the lower Si content, occurring between passes 3 and 4.

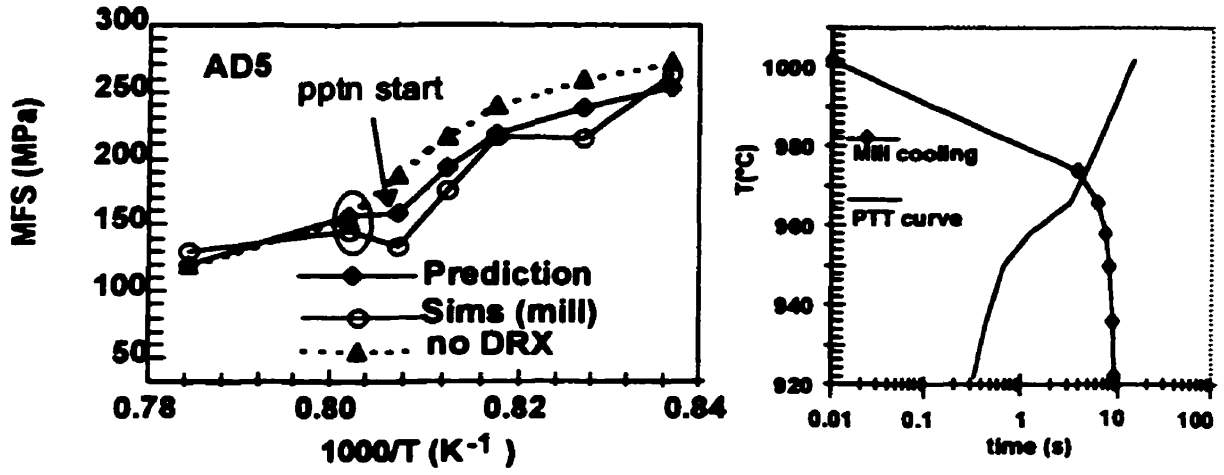

Figure 7.8 (a) Comparison of MFS predictions and observations for the AD5 grade. The arrow indicates the precipitation start point. As a result, DRX is considered to occur during the second pass, followed by MDRX. (b) Comparison of precipitation-start curve with mill cooling curve. The point of intersection indicates the moment when precipitation starts.

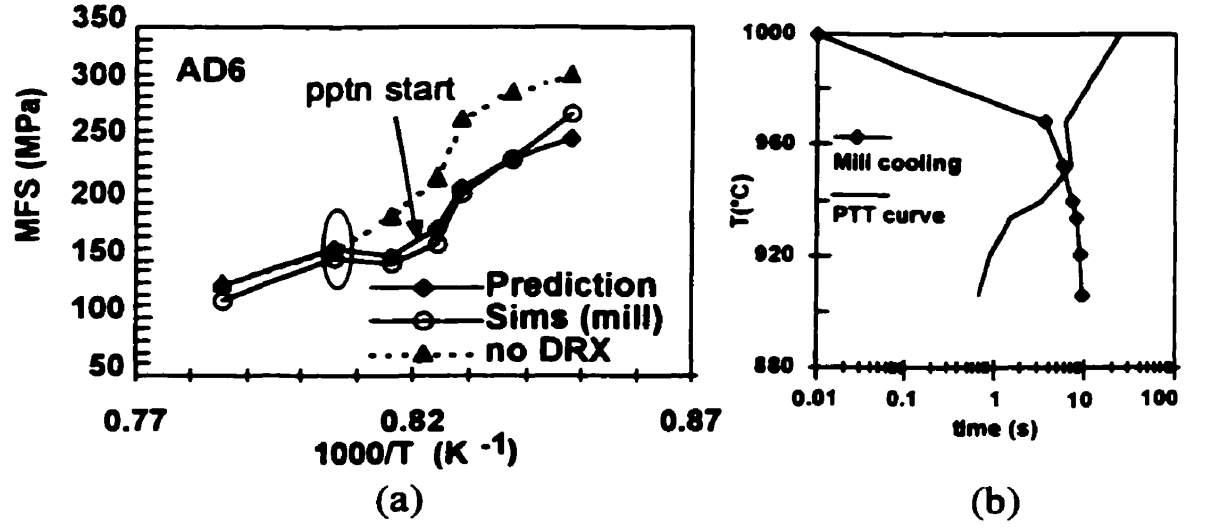

Figure 7.9 (a) Comparison of MFS predictions and observations for the AD6 grade. The arrow indicates the precipitation start point. As a result, DRX is considered to occur during the second pass, followed by MDRX. (b) Comparison of precipitation-start curve with mill cooling curve. The point of intersection indicates the moment when precipitation starts.

Figures 7.10 and 7.11 show the effect of Mn in steels AD2 and AD4, which contained 0.020% Nb and 0.225% Si. Considering grade AD2 first, which contained 0.65% Mn, according to the mill data, precipitation was initiated between passes 3 and 4. In the same way, in grade AD4, with the same base composition but containing 1 % Mn, the start of precipitation was delayed (to between passes 5 and 6) and the modified predictions again fitted the MFS values calculated using the mill data. In both cases, according to the present model, no DRX was initiated.

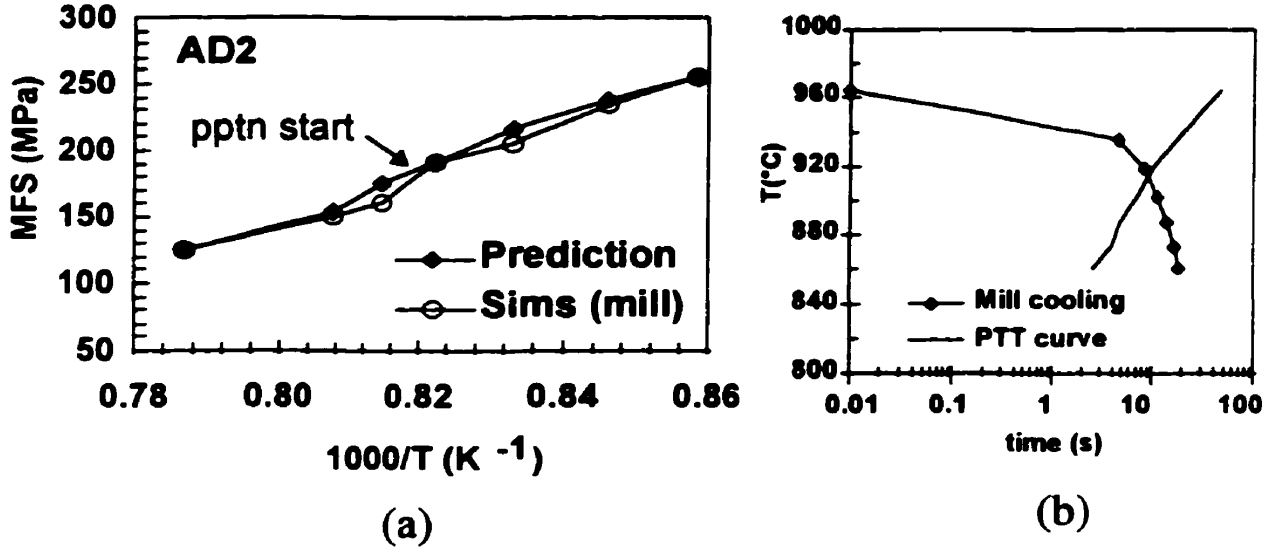

Figure 7.10 (a) Comparison of MFS predictions and observations for the AD2 grade. The arrow indicates the precipitation start point. (b) Comparison of precipitation-start curve with mill cooling curve. The point of intersection indicates the moment when precipitation starts.

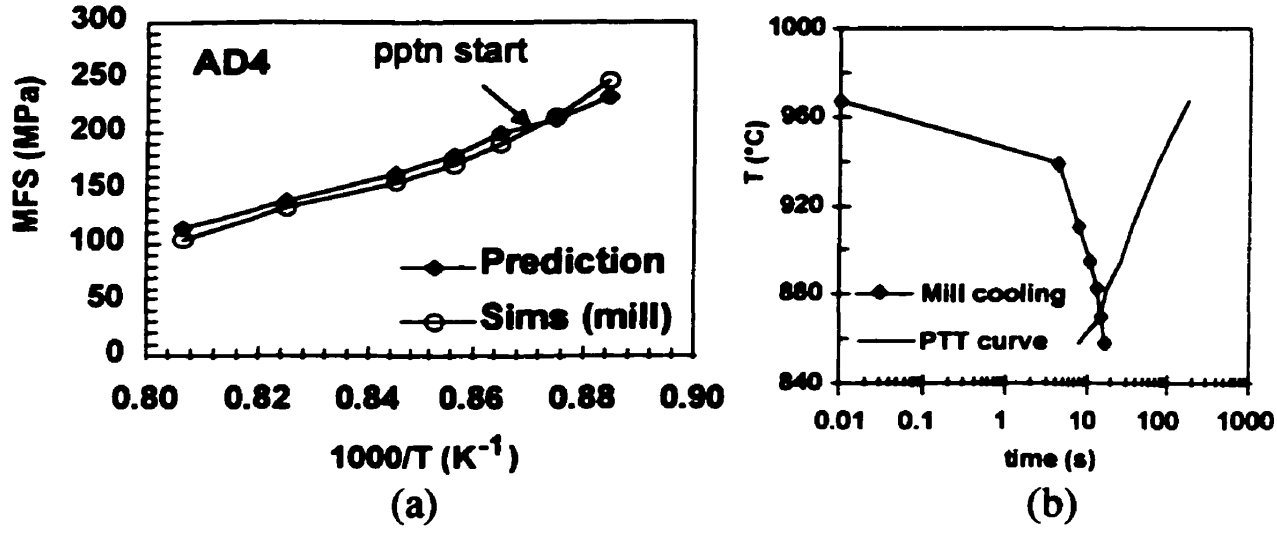

Figure 7.11 (a) Comparison of MFS predictions and observations for the AD4 grade. The arrow indicates the precipitation start point. (b) Comparison of precipitation-start curve with mill cooling curve. The point of intersection indicates the moment when precipitation starts.

As discussed in section 7.3, it is not common to observe hardening due to Nb(C,N) precipitation in the austenite region. This is because the high temperatures involved are not amenable to formation of the fine precipitates necessary to cause strengthening. Nonetheless, the MFS values derived from the mill logs for the last one or two passes are frequently somewhat higher than the model predictions. Similar underestimates of the rolling force (and consequently of the MFS) in the later rolling passes have been reported by Samarasekera et al. [103].

The present study leads to the conclusion that Mn addition retards the strain-induced precipitation of Nb(C,N), an effect that must be taken into account even during the relatively short times involved in strip rolling. On the other hand, Si addition has an *accelerating* effect on Nb(C,N) precipitation. It has also been shown that the precipitation start times applicable to strip mill rolling conditions can be predicted by modifying the DS equation so as to take the Mn and Si levels into account. This relation can then be incorporated into a model of the MFS behaviour. The predictions obtained from the model described here are in good agreement with mill observations.

Ideally, a systematic study should be made of the DS equation, involving all the constants and parameters (such as the activation energy for diffusion, chemical driving forces, reheating temperatures, roughing practice, etc...). Then the effects of Mn and Si addition should be introduced into these parameters. In this way, single values could be found, for example, for the constants A and B. For practical purposes, however, simple correlations between A (or B) and the other parameters can be employed (as was done here) to predict the precipitation-start times correctly.

Chapter 8 - Application of the Model and Improving Hot Strip Rolling Schedules

The prediction of rolling force during finish rolling is an important tool for the improvement of rolling schedules and of mill setups. It can also help to obtain better gauge control and to reduce the generation of scrap. The aim of this work was therefore to establish a method of predicting the MFS and grain size based on physical phenomena. Several papers were published based on the present study. The modeling of MFS, grain size and fractional softening was investigated in C-Mn [114], Nb [115] and multiply-alloyed steels [99]. Publications have also appeared dealing with the precipitation kinetics [116] and the critical strain for DRX [106] in Nb steels. Two additional papers have been published on the approach of the present model as a whole [117,118].

It is useful to distinguish here between conventional controlled rolling, where the aim is to produce work hardened austenite, and DRX (+MDRX) controlled rolling, where the main purpose is to refine the austenite grain size. This work shows that both strategies are applicable to industrial strip rolling and that both intense grain refinement and strain accumulation can take place. Recent publications [119,120] indicate that DRX (+MDRX) can be used to design schedules for the thermomechanical processing of steels when particular mechanical properties are desired.

In the following pages, the mean flow stress (MFS) and grain size developed in each pass are calculated from the mill logs. Here, corrections are used for the

forward-slip ratio and the redundant strain, according to the spreadsheet shown in Chapter 3. The MFS's are predicted using the MFS model described in Chapter 4, which takes into account the chemical composition as well as the occurrence of DRX+MDRX. The microstructure model of Chapter 5 is employed, together with the model that predicts the critical strain for the initiation of dynamic recrystallization (Chapter 6). All the MFS calculations are based on the total strain (nominal + residual from the previous pass). For the Nb grades, the precipitation behavior during hot rolling is simulated using the model outlined in Chapter 7. Examples will be presented of each steel type starting from the C-Mn, followed by the Cr-Mo, and finally, the Nb-microalloyed grades.

For the plain C-Mn and Cr-Mo steels, the model predicts the MFS, grain size, amount of softening and extent of DRX during the schedule, in a pass-by-pass analysis. For the Nb grades, the precipitation of niobium carbonitrides is first predicted, which generally changes the behaviour of the steel during rolling by preventing any further softening.

The Sims (i.e. mill) and predicted MFS$^+$ values are plotted together with Misaka's MFS for all grades. However, the **accumulated strains** (calculated using the spreadsheet) are always employed to feed the Misaka equation. This allows the latter to fit the MFS curve more closely, especially when only small amounts of softening have taken place (common in the final passes, where the temperature is relatively low). The use of the original Misaka formulation with the *nominal* strain of the pass led to poorer fits.

The measured and predicted MFS's are plotted together and compared for each strip tested in this investigation.

8.1 - Plain C-Mn Steels

The analysis of the rolling schedules of plain C-Mn grades is straightforward. In any particular pass, a strain is applied that results in softening during the interpass time and a characteristic grain size; the latter quantities act as inputs for the subsequent pass. The total strain is considered in the calculation of the MFS, according to Equations 4.3 and 4.8. The equations that describe the microstructures were presented in Chapter 5.

The plain C-Mn grades display a single type of behaviour, one where MDRX occurs in the first passes. This is exemplified in Spreadsheets and Figures 8.1 to 8.6. The high temperatures and low strain rates involved decrease the peak strain, so that the critical strain for DRX is attained. Because no solute drag elements (such as Nb) are present, the SRX and MDRX kinetics are rapid, as displayed in Spreadsheets 8.1-8.6. The fractional softening during the interpass interval (X) is always close to 1, for both the SRX and DRX+MDRX softening mechanisms. Nevertheless the spreadsheet indicates that there is a small amount of strain accumulation in the final passes, due to the relatively low temperatures.

As shown in the corresponding MFS charts, the Misaka equation always overpredicts the MFS. This is due to the low Mn content of these grades (with the exception of steel CS1, which contained 1.08% Mn, Spreadsheet and Figure 8.3). In this case, the Misaka curve is closer to the predicted MFS, calculated according to Equations 4.3 and 4.8. Note that the model MFS$^+$ fits the Sims (mill) curve more closely, which demonstrates the effectiveness of the compositional term. There is no precipitation and DRCR is occurring in the initial passes in all the strips analyzed here, causing most of the grain refinement to occur in this part of the schedule (see the columns headed "d (μm)"). After the last pass, the grain size obtained was about 15μm for all grades.

The abrupt drop in MFS that occurs in the last stand of the Algoma grade (see Figure 8.1) appears to be associated with the start of the austenite-to-ferrite transformation. The temperature of the last pass, 887°C is near the Ar_3 temperature, 879°C, calculated using the equation of Ouchi et al. [121]. According to Boratto et al. [60], however, deviations of up to 17°C can be observed from the Ouchi et al. predictions. Note that the present model does not actually take the possibility of the austenite-to-ferrite transformation into account; thus, the MFS value "predicted" for the last stand is arbitrarily taken here as the actual prediction reduced by 15%, to allow for the beginning of the transformation. The CS1 and CS2 grades were also rolled at low temperatures during the final passes; however, due to chemical factors (especially the higher carbon), the Ar_3 was decreased drastically when compared to the CA grade. This assured that the steel was fully austenitic during the last finishing passes.

Spreadsheet 8.1 - Grain size, fractional softening and MFS predictions for the CA grade.

Grade: CA

strip ID
201100

C	0.03
Mn	0.27
Si	0.010

pass	d (μm)	T (°C)	$\dot{\varepsilon}$ (s^{-1})	i.p.time (s)	ε	ε_a	ε_c	DRX ?	$\varepsilon_{0.5}$	X_{dyn}	$t_{0.5}$ (s)	X
F 1	100.0	1029	15.3	3.45	0.78	0.78	0.50	Y	0.56	0.29	0.05	1.00
F 2	29.2	999	29.1	2.13	0.63	0.63	0.43	Y	0.48	0.26	0.03	1.00
F 3	23.6	966	55.1	1.35	0.57	0.57	0.41	Y	0.53	0.19	0.02	1.00
F 4	18.4	921	89.3	0.94	0.43	0.43	0.49	--	0.62	0.00	0.09	1.00
F 5	23.3	907	121.9	0.71	0.35	0.35	0.59	--	0.72	0.00	0.32	0.78
F 6	15.4	887	143.4		0.25	0.33	0.59	--	0.72	0.00	0.20	

pass	d if X >0.95		growth. after		1000/T	MFS +	Sims	Misaka
	MRX	SRX	MRX	SRX	(K^{-1})	(MPa)	(MPa)	(MPa)
F 1	21.9	36.5	29.2	44.9	0.77	116	114	136
F 2	16.1	22.3	23.6	35.4	0.79	127	124	149
F 3	11.2	18.7	18.4	27.9	0.81	143	137	170
F 4	8.5	17.5	12.7	23.3	0.84	152	157	187
F 5	7.1	19.9	6.2	15.4	0.85	157	164	192
F 6	6.4	16.7	15.4	15.4	0.86	131	138	166

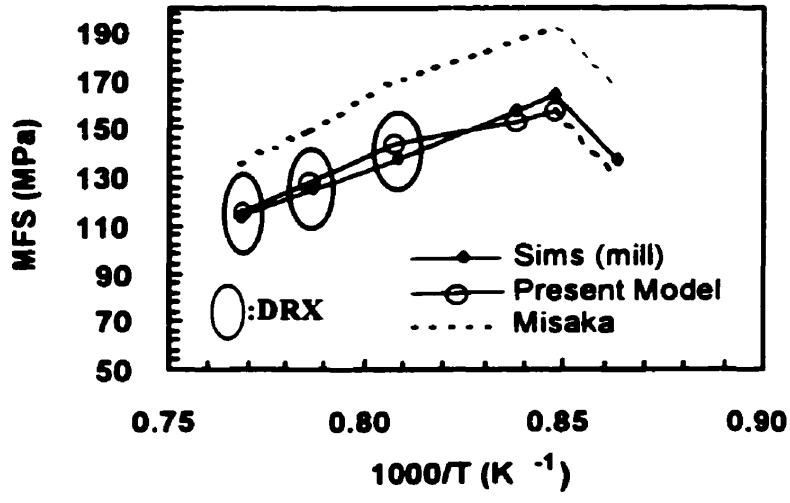

Figure 8.1 - MFS chart for grade CA.

Spreadsheet 8.2 - Grain size, fractional softening and MFS predictions for the CD grade.

Grade: CD

C	0.06
Mn	0.27

strip ID
T93519

pass	d (μm)	T (°C)	$\dot{\varepsilon}$ (s^{-1})	i.p.time (s)	ε	ε_a	ε_c	DRX ?	$\varepsilon_{0.5}$	X_{dyn}	$t_{0.5}$ (s)	X
F 1	100.0	1003	11.83	3.27	0.60	0.60	0.44	Y	0.61	0.17	0.06	1.00
F 2	26.2	975	19.04	2.25	0.47	0.47	0.35	Y	0.50	0.16	0.04	1.00
F 3	22.3	959	30.06	1.62	0.43	0.43	0.38	Y	0.53	0.06	0.03	1.00
F 4	19.6	941	41.29	1.24	0.34	0.34	0.42	--	0.56	0.00	0.12	1.00
F 5	29.0	926	61.08	0.93	0.33	0.33	0.54	--	0.67	0.00	0.39	0.81
F 6	19.4	909	82.36	0.73	0.28	0.34	0.54	--	0.67	0.00	0.22	0.90
F 7	16.9	895	88.74		0.19	0.22	0.54	--	0.69	0.00	0.54	

pass	d if X >0.95		growth. after		1000/T	MFS +	Sims	Misaka
	MRX	SRX	MRX	SRX	(K^{-1})	(MPa)	(MPa)	(MPa)
F 1	20.5	38.1	26.2	42.3	0.78	112	113	134
F 2	16.3	23.4	22.3	33.5	0.80	120	128	143
F 3	13.4	21.7	19.6	29.7	0.81	125	134	153
F 4	11.3	21.8	16.4	29.0	0.82	127	133	158
F 5	9.4	24.4	8.2	19.4	0.83	137	143	170
F 6	8.0	19.2	7.2	16.9	0.85	149	148	185
F 7	7.6	21.8	16.9	16.9	0.86	142	165	176

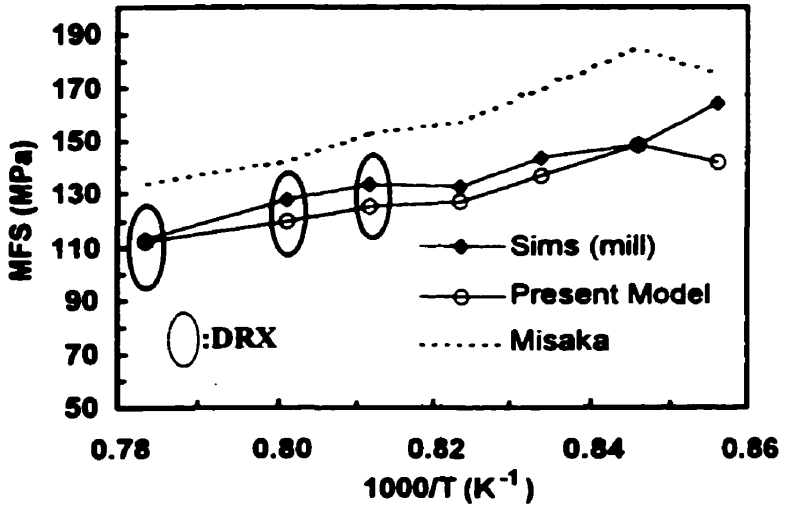

Figure 8.2 - MFS chart for grade CD.

Spreadsheet 8.3 - Grain size, fractional softening and MFS predictions for the CS1 grade.

Grade: CS1

C	0.10
Mn	1.08
Si	0.060

strip ID
255733

pass	d (μm)	T (°C)	$\dot{\varepsilon}$ (s^{-1})	i.p.time (s)	ε	ε_a	ε_c	DRX ?	$\varepsilon_{0.5}$	X_{dyn}	$t_{0.5}$ (s)	X
F 1	100.0	958	9.6	3.63	0.62	0.62	0.48	Y	0.73	0.12	0.1	1.00
F 2	21.5	927	15.4	2.52	0.48	0.48	0.37	Y	0.58	0.13	0.0	1.00
F 3	17.5	897	26.7	1.76	0.46	0.46	0.44	Y	0.65	0.03	0.0	1.00
F 4	15.1	892	52.4	1.16	0.52	0.52	0.48	Y	0.66	0.04	0.0	1.00
F 5	13.8	885	72.3	0.87	0.37	0.37	0.51	--	0.68	0	0.1	1.00
F 6	17.5	877	99.5	0.67	0.32	0.32	0.60	--	0.76	0	0.4	0.82
F 7	13.4	867	110.6		0.23	0.29	0.59	--	0.75	0	0.3	

pass	d if X >0.95		growth. after		1000/T	MFS +	Sims	Misaka
	MRX	SRX	MRX	SRX	(K^{-1})	(MPa)	(MPa)	(MPa)
F 1	16.7	32.0	21.5	35.1	0.81	134	122	145
F 2	12.6	17.4	17.5	26.2	0.83	146	154	157
F 3	10.0	15.3	15.1	22.8	0.85	164	161	179
F 4	8.2	13.3	13.8	20.9	0.86	185	162	202
F 5	7.3	14.8	10.0	17.5	0.86	183	189	199
F 6	6.4	16.7	5.5	13.4	0.87	189	193	206
F 7	6.1	15.6	13.4	13.4	0.88	191	209	209

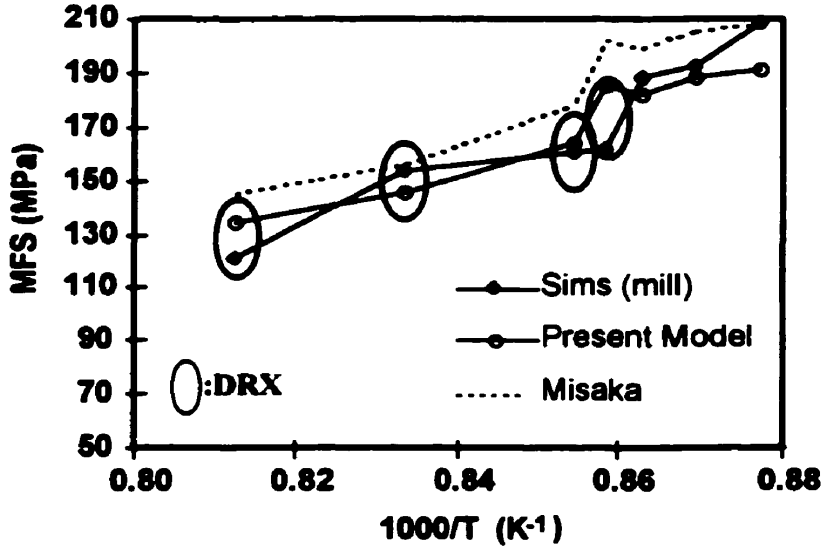

Figure 8.3 - MFS chart for grade CS1.

Spreadsheet 8.4 - Grain size, fractional softening and MFS predictions for the CS2 grade.

Grade: CS2

strip ID
523692

C	0.45
Mn	0.76
Si	0.210

pass	d (μm)	T (°C)	$\dot{\varepsilon}$ (s^{-1})	i.p.time (s)	ε	ε_a	ε_c	DRX ?	$\varepsilon_{0.5}$	X_{dyn}	$t_{0.5}$ (s)	X
F 1	100.0	1043	4.5	8.60	0.95	0.95	0.30	Y	0.5	0.59	0.1	1.00
F 2	35.5	1000	12.0	4.45	0.83	0.83	0.31	Y	0.48	0.53	0.1	1.00
F 3	27.5	983	26.6	2.51	0.66	0.66	0.35	Y	0.50	0.35	0.0	1.00
F 4	22.8	957	49.5	1.56	0.54	0.54	0.41	Y	0.55	0.15	0.0	1.00
F 5	18.8	930	79.7	1.01	0.41	0.41	0.47	--	0.60	0	0.1	1.00
F 6	24.4	903	122.6	0.72	0.35	0.35	0.61	--	0.74	0	0.4	0.80
F 7	15.6	877	128.5	0.00	0.19	0.26	0.60	--	0.75	0	0.5	

pass	d if X >0.95		growth. after		1000/T (K^{-1})	MFS + (MPa)	Sims (MPa)	Misaka (MPa)
	MRX	SRX	MRX	SRX				
F 1	30.2	33.8	35.5	51.1	0.76	115	99	139
F 2	20.7	21.6	27.5	40.8	0.79	139	129	170
F 3	15.4	20.4	22.8	34.3	0.80	157	168	187
F 4	11.5	19.0	18.8	28.5	0.81	179	180	208
F 5	8.8	18.2	13.3	24.4	0.83	196	209	225
F 6	6.8	19.8	6.0	15.6	0.85	216	206	247
F 7	6.2	18.2	15.6	15.6	0.87	221	226	253

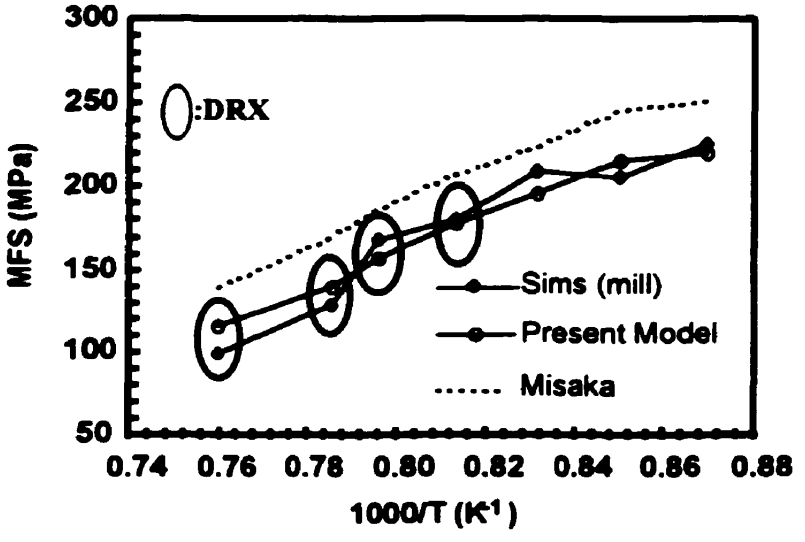

Figure 8.4 - MFS chart for grade CS2.

Spreadsheet 8.5 - Grain size, fractional softening and MFS predictions for the CM grade.

Grade: CM

strip ID (reference)

C	0.03
Mn	0.24
Si	0.020

pass	d (μm)	T (°C)	$\dot{\varepsilon}$ (s^{-1})	i.p.time (s)	ε	ε_a	ε_c	DRX ?	$\varepsilon_{0.5}$	X_{dyn}	$t_{0.5}$ (s)	X
F 1	100.0	1015	8.1	4.7	0.65	0.65	0.39	Y	0.57	0.27	0.08	1.00
F 2	29.9	996	18.9	2.64	0.66	0.66	0.34	Y	0.48	0.37	0.04	1.00
F 3	24.5	971	38.6	1.55	0.59	0.59	0.41	Y	0.52	0.22	0.02	1.00
F 4	19.6	933	67.3	1.02	0.47	0.47	0.46	Y	0.59	0.01	0.01	1.00
F 5	15.5	923	99.3	0.74	0.35	0.35	0.48	--	0.60	0.00	0.09	1.00
F 6	22.3	916	136.9	0.56	0.31	0.31	0.58	--	0.68	0.00	0.29	0.73
F 7	16.3	910	178.5		0.26	0.35	0.56	--	0.66	0.00	0.13	

pass	d if X >0.95		growth. after		1000/T	MFS +	Sims	Misaka
	MRX	SRX	MRX	SRX	(K^{-1})	(MPa)	(MPa)	(MPa)
F 1	24.3	38.8	29.9	45.8	0.78	107	100	119
F 2	17.8	22.0	24.5	36.5	0.79	125	116	138
F 3	12.7	19.2	19.6	29.5	0.80	136	135	157
F 4	9.8	18.0	15.5	28.1	0.83	145	145	173
F 5	8.6	18.5	11.9	22.3	0.84	145	135	174
F 6	7.6	22.2	6.6	16.3	0.84	150	137	181
F 7	7.1	18.3	16.3	16.3	0.85	161	163	184

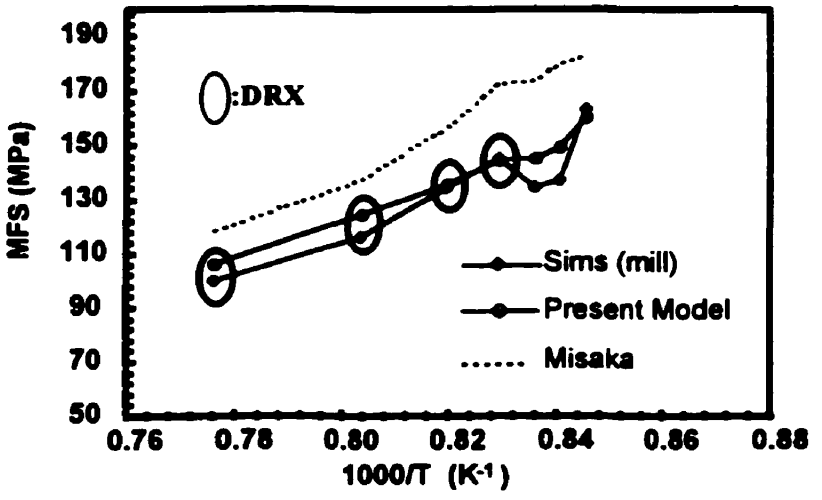

Figure 8.5 - MFS chart for grade CM.

Spreadsheet 8.6 - Grain size, fractional softening and MFS predictions for the CU grade.

Grade: CU

strip ID (reference)

C	0.05
Mn	0.24
Si	0.002

pass	d (μm)	T (°C)	$\dot{\varepsilon}$ (s^{-1})	i.p.time (s)	ε	ε_a	ε_c	DRX ?	$\varepsilon_{0.5}$	X_{dyn}	$t_{0.5}$ (s)	X
F 1	100.0	980	15.2	3.87	0.58	0.58	0.56	Y	0.68	0.02	0.05	1.00
F 2	23.6	945	32.2	2.34	0.63	0.63	0.45	Y	0.57	0.19	0.03	1.00
F 3	19.1	923	48.9	1.55	0.40	0.40	0.44	--	0.61	0.00	0.10	1.00
F 4	24.3	909	88.9	1.13	0.45	0.45	0.56	--	0.71	0.00	0.16	0.99
F 5	22.4	899	108.4	0.88	0.29	0.30	0.59	--	0.73	0.00	0.47	0.72
F 6	15.4	890	111.0	0	0.18	0.26	0.55	--	0.70	0.00	0.35	

pass	d if X >0.95		growth. after		1000/T	MFS +	Sims	Misaka
	MRX	SRX	MRX	SRX	(K^{-1})	(MPa)	(MPa)	(MPa)
F 1	16.7	35.5	23.6	39.0	0.80	115	115	142
F 2	12.0	17.3	19.1	28.8	0.82	142	140	170
F 3	9.9	18.5	16.1	24.3	0.84	138	142	171
F 4	8.0	18.4	12.0	22.4	0.85	158	150	195
F 5	7.2	21.1	6.4	15.4	0.85	151	153	188
F 6	7.0	19.2	15.4	15.4	0.86	150	146	186

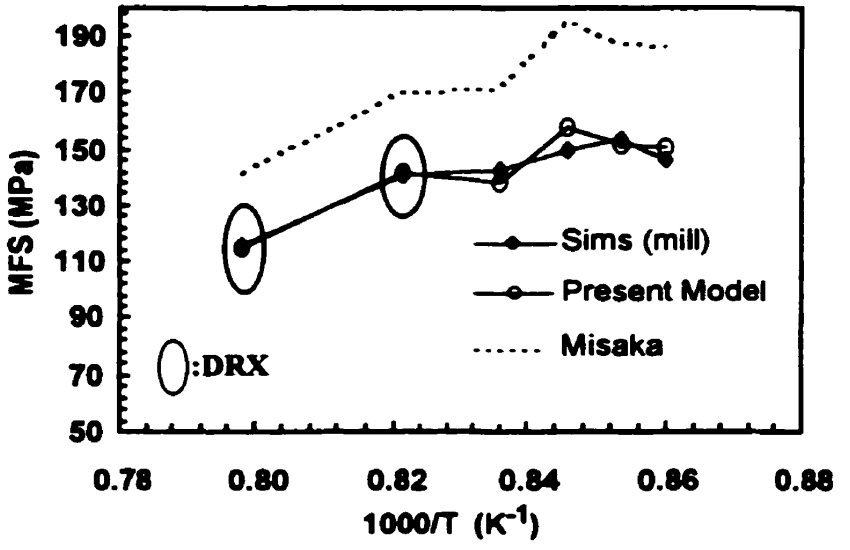

Figure 8.6 - MFS chart for grade CU.

8.2 - Cr-Mo Steels

The Cr-Mo steels displayed MFS behaviors that were similar to those of the C-Mn steels. This is shown in Spreadsheets and Figures 8.7 and 8.8, for grades BCM and BCMVN. The predicted MFS's are in excellent agreement with the MFS values calculated from the mill logs. For the present multiply-alloyed grades, the ratio $\varepsilon_c/\varepsilon_p$ was set equal to 0.8, which was the ratio employed for the C-Mn steels.

The BCM grade is only lightly alloyed with Cr and Mo and therefore displays considerable softening during all the interpass intervals. These elements are not considered as severe recrystallization inhibitors, although they do have an effect on the kinetics [48,99,122]. The latter is taken into account via the $t_{0.5}$ equation. Additionally, DRX+MDRX takes place in the third pass, where the accumulated strain overcomes the critical strain for DRX. Compared with the plain C-Mn steels, the kinetics of recrystallization in the present multiply-alloyed steels are about 10 times slower during static recrystallization (compare the $t_{0.5}$ columns for the C-Mn and Cr-Mo grades). Figure 8.7 shows that the present model fits the Sims (mill) MFS data very well. This grade was rolled at relatively high temperatures and the kinetics of SRX decrease with temperature. The steel does not soften completely and some strain remains for the next pass, adding the residual to the newly applied strain. This seemed to occur during passes 1 and 2 and the MFS drop between passes 3 and 4 is successfully predicted and attributed to the occurrence of DRX+MDRX, due to strain accumulation. During the rest of the schedule, considerable strain is accumulated; however, the critical strain increases proportionally, due to the higher strain rates and lower temperatures in the last passes, thus avoiding the occurrence of DRX a second time.

With reference to Spreadsheet and Figure 8.8, the rolling simulations indicate that, during processing of the relatively highly alloyed, BCMVN (C-Mn-Cr-Mo-V-Nb-Ni) steel, dynamic recrystallization occurred in each of the first three stands as well as in the fifth stand. It is evident that dynamic recrystallization takes place in the present material because:

Spreadsheet 8.7 - Grain size, fractional softening and MFS predictions for the BCM grade.

Grade: BCM

	C	0.28	V	Tr.
	Mn	0.52	Nb	Tr.
strip ID	Cr	0.83	N	0.0047
513624	Ni	Tr.	Mo	0.15

pass	d (μm)	T (°C)	$\dot{\varepsilon}$ (s^{-1})	i.p.time (s)	ε	ε_a	ε_c	DRX ?	$\varepsilon_{0.5}$	X_{dyn}	$t_{0.5}$ (s)	X
F 1	100.0	1098	5.24	18.53	0.83	0.83	1.00	--	4.46	0	8.80	0.77
F 2	44.3	1052	10.43	4.39	0.61	0.80	0.86	--	6.96	0	3.61	0.57
F 3	28.3	1028	22.77	2.55	0.65	0.99	0.85	Y	10.12	0.01	0.42	0.99
F 4	20.2	1006	37.72	1.72	0.48	0.49	0.84	--	13.69	0	7.52	0.15
F 5	19.2	983	57.72	1.17	0.39	0.81	0.95	--	19.74	0	2.59	0.27
F 6	16.5	959	78.75	0.88	0.30	0.89	1.01	--	27.31	0	2.48	0.22
F 7	14.6	934	81.83		0.18	0.87	1.05	--	35.67	0	2.69	

pass	d if X >0.95		growth. after		1000/T	MFS +	Sims	Misaka
	MRX	SRX	MRX	SRX	(K^{-1})	(MPa)	(MPa)	(MPa)
F 1	14.5	27.4	15.6	44.3	0.73	126	120	125
F 2	11.8	16.2	13.8	28.3	0.75	150	145	142
F 3	9.9	10.4	20.2	20.2	0.77	183	175	169
F 4	8.5	13.3	15.4	19.2	0.78	176	181	179
F 5	7.4	9.2	11.5	16.5	0.80	218	232	192
F 6	6.5	7.8	10.9	14.6	0.81	245	247	202
F 7	6.1	7.3	14.6	14.6	0.83	260	276	196

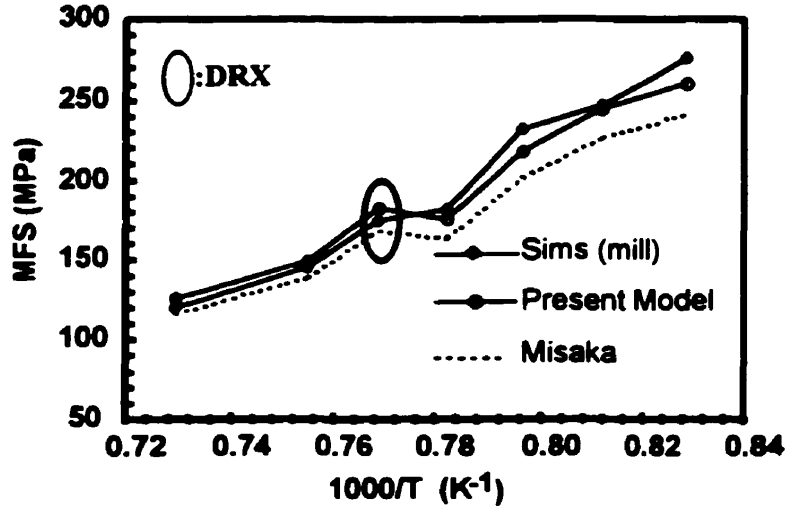

Figure 8.7 - MFS chart for grade BCM.

Spreadsheet 8.8 - Grain size, fractional softening and MFS predictions for the BCMVN grade.

Grade: BCMVN

	C	0.47	V	0.12
	Mn	0.66	Nb	0.016
strip ID	Cr	0.98	N	0.0042
523671	Ni	0.46	Mo	0.97

pass	d (μm)	T (°C)	$\dot{\varepsilon}$ (s^{-1})	i.p.time (s)	ε	ε_a	ε_c	DRX ?	$\varepsilon_{0.5}$	X_{dyn}	$t_{0.5}$ (s)	X
F 1	100	1094	6.09	16.62	0.96	0.96	0.66	Y	4.8	0.0416	0.12	1.00
F 2	56.2	1043	13.6	3.67	0.68	0.68	0.65	Y	8.8	0.0022	0.06	1.00
F 3	32.2	1029	26.7	2.23	0.58	0.58	0.58	Y	11	5E-05	0.03	1.00
F 4	25.9	1012	49	1.43	0.52	0.52	0.61	--	15	0	20.41	0.05
F 5	25.4	995	78.6	0.94	0.42	0.92	0.68	Y	21	0.0078	0.01	1.00
F 6	16.9	978	129	0.66	0.38	0.38	0.64	--	26	0	102.40	0.00
F 7	16.8	960	136		0.20	0.58	0.68	--	32	0	37.51	

pass	d if X >0.95		growth. after		1000/T	MFS +	Sims	Misaka
	MRX	SRX	MRX	SRX	(K^{-1})	(MPa)	(MPa)	(MPa)
F 1	13.96	24.73	56.19	56.19	0.73	155	155	130
F 2	11.29	21.14	32.16	32.16	0.76	180	185	150
F 3	9.80	16.23	25.92	25.92	0.77	196	262	163
F 4	8.52	15.02	23.67	25.40	0.78	216	236	180
F 5	7.53	10.19	16.85	16.85	0.79	269	272	224
F 6	6.61	13.87	16.71	16.84	0.80	249	257	208
F 7	6.34	10.52	16.84	16.84	0.81	287	296	239

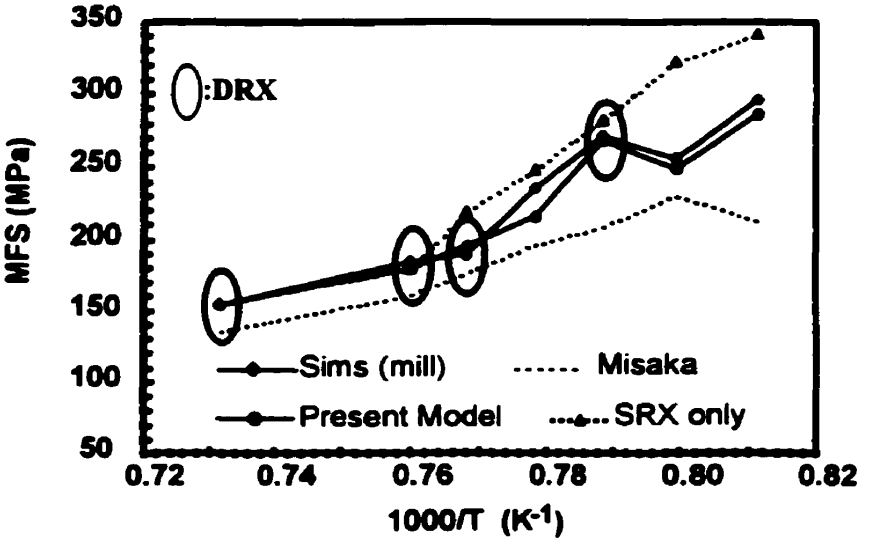

Figure 8.8 - MFS chart for grade BCMVN.

i) Of all the alloying elements used in this work, Nb is the most effective with respect to the retardation of recrystallization [35,123] and the present steel only contains 0.016%, whereas the usual Nb content is 0.03-0.08%.

ii) By contrast, as Nb is likely to precipitate when rolling is carried out below 1000°C, dynamic recrystallization is normally likely to be impeded at low finish rolling temperatures in the Nb-bearing grades investigated.

iii) The rolling temperatures employed for these steels are higher than in the other materials, where finish rolling was initiated below 1000°C. By contrast, in this schedule, the rolling temperature remained above 1000°C within the first four or five stands.

iv) The strains employed in these particular schedules are higher than those used for the usual C-Mn and Nb steels, a condition that also promotes the occurrence of dynamic recrystallization.

It should be noted that, according to the spreadsheet analysis, dynamic recrystallization occurs at the fifth stand as a result of strain accumulation in the fourth and fifth stands. By contrast, no strain accumulation is required for DRX to occur in the earlier stands. Finally, it should be pointed out that, when no allowance is made for DRX and MRX in the model, i.e. when the only softening mechanism that can operate is SRX, the predicted MFS's are clearly too high.

8.3 - Nb Steels

Analysis of the Nb steel mill data was by far the most complex. This is because it involves mechanisms such as SRX and DRX+MDRX and the precipitation of Nb carbonitrides. The occurrence of DRX+MDRX was mainly in the initial passes or after strain accumulation due to incomplete softening.

The Nb steel displayed a variety of rolling behaviors. For this reason, the grades are presented according to the operational softening mechanism (SRX or MDRX) and the occurrence or not of precipitation. Four basic behaviors were

observed in the group A steels: i) SRX only and no precipitation; ii) SRX and DRX+MDRX and no precipitation; iii) SRX and DRX+MDRX and precipitation in the last passes; iv) SRX and precipitation The results for each type observed are introduced in the following sections.

8.3.1 - SRX only and no Precipitation

Among all the bars analyzed, only two grades displayed SRX only and no precipitation: AD9 and AD10. These are low C, low Nb (0.008% Nb) grades and the spreadsheets and MFS charts are presented in Figures 8.9 and 8.10. They have the same base composition with the exception of the Mn content. In both cases, the low Nb contents are responsible for this particular behavior. Firstly, the critical strains are close to the ones applicable to C-Mn steels and the total strains (nominal plus accumulated) are less than the critical strain for a given pass, thus avoiding the occurrence of DRX. According to the points discussed in Chapter 6, the presence of Nb in solid solution at higher levels has a retarding effect on softening, increasing the peak strain and therefore, increasing the critical strain. Secondly, no precipitation was predicted by the model. At this particular level of Nb, there is only a small driving force for precipitation, and it was not reached even in the final passes. The simulated MFS curves shown in Figures 8.9 and 8.10 are of the ascending type. Both display fairly good fits to the Sims curves. Note that the original Misaka equation overpredicts the MFS's in both cases. For the alloying levels used, this overprediction was expected.

Finally, it should be noted that there is little grain refinement, because softening occurs only by SRX, which refines the grain size less than DRX+MDRX. The final grain sizes obtained in the two cases were about 30μm.

Spreadsheet 8.9 - Microstructural and MFS predictions for the AD9 grade.

Grade: AD9

strip ID
E15045

C	0.060
Mn	0.443
Nb	0.009
Si	0.010
Reheat T(°C) =	1215

pass	d (μm)	T (°C)	$\dot{\varepsilon}$ (s^{-1})	i.p.time (s)	time (s)	Z (s^{-1})	K_s	t_{ps} (s)	Sum t_p/t_{ss}	PPTN?	ε	ε_a	ε_c	DRX
F 1	80.0	1002	12.7	3.64	0.01	2.9E+16	5.37	335.6	0.01	No	0.70	0.70	0.77	--
F 2	45.7	968	23.4	2.33	3.65	1.4E+17	6.67	149.8	0.03	No	0.57	0.57	0.76	--
F 3	36.1	953	43.4	1.54	5.98	4.2E+17	7.72	89.1	0.04	No	0.54	0.54	0.81	--
F 4	31.9	936	69.9	1.07	7.52	1.1E+18	8.96	64.4	0.06	No	0.44	0.47	0.90	--
F 5	32.0	921	99.4	0.76	8.58	2.5E+18	10.25	44.1	0.08	No	0.33	0.49	1.04	--
F 6	31.6	908	139.4	0.55	9.34	5.4E+18	11.76	29.7	0.10	No	0.30	0.56	1.17	--
F 7	30.3	893	155.6		9.89	1.0E+19	12.68	24.1	0.10	No	0.20	0.56	1.27	--

pass	$\varepsilon_{0.5}$	X_{dyn}	$t_{0.5}$ (s)	X	d if X >0.95 MRX	d if X >0.95 SRX	growth after MRX	growth after SRX	1000/T (K^{-1})	MFS + (MPa)	Sims (MPa)	Misaka (MPa)
F 1	0.60	0	0.27	1.00	9.5	45.4	45.7	45.7	0.78	116	121	139
F 2	0.61	0	0.32	0.99	8.0	36.0	36.1	36.1	0.81	128	126	154
F 3	0.64	0	0.36	0.95	6.9	31.7	6.5	31.9	0.82	141	134	170
F 4	0.68	0	0.68	0.66	6.1	32.0	7.2	32.0	0.83	151	157	182
F 5	0.74	0	0.87	0.46	5.5	31.1	11.4	31.6	0.84	165	184	198
F 6	0.80	0	0.82	0.37	5.0	28.1	13.8	30.3	0.85	182	191	219
F 7	0.85	0	0.99		4.7	27.7	30.3	30.3	0.86	191	199	229

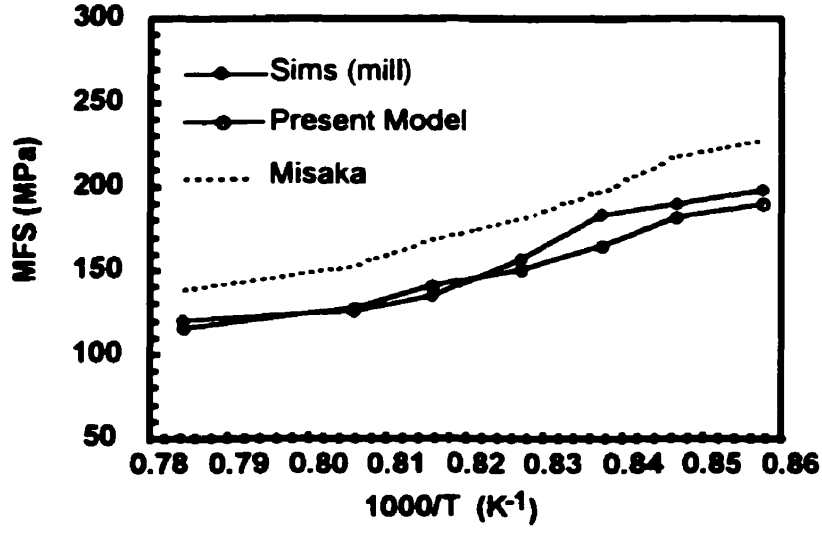

Figure 8.9 - MFS chart for grade AD9.

Spreadsheet 8.10 - Microstructural and MFS predictions for the AD10 grade.

Grade: AD10

strip ID
A12800

C	0.063
Mn	0.628
Nb	0.007
Si	0.008
Reheat T(°C) =	1215

pass	d	T	$\dot{\varepsilon}$	i.p.time	time	Z	K_s	t_{ps}	Sum	PPTN?	ε	ε_a	ε_c	DRX
	(μm)	(°C)	(s^{-1})	(s)	(s)	(s^{-1})		(s)	t_p/t_{ps}					
F 1	80.0	985	15.7	3.09	0.01	5.9E+16	5.81	232.9	0.01	No	0.66	0.66	0.89	--
F 2	47.2	960	28.4	1.96	3.10	2.2E+17	7.38	123.0	0.03	No	0.56	0.56	0.85	--
F 3	37.8	931	44.6	1.38	5.06	8.4E+17	8.75	73.9	0.05	No	0.45	0.49	0.95	--
F 4	35.7	923	77.6	0.93	6.43	1.8E+18	9.43	40.1	0.07	No	0.47	0.63	1.06	--
F 5	30.0	915	115.3	0.67	7.37	3.6E+18	10.43	40.1	0.09	No	0.35	0.49	1.09	--
F 6	29.9	902	138.9	0.51	8.03	6.6E+18	11.72	29.3	0.11	No	0.25	0.55	1.21	--
F 7	29.2	891	147.9		8.54	1.0E+19	11.89	25.2	0.11	No	0.15	0.52	1.28	--

pass	$\varepsilon_{0.5}$	X_{dyn}	$t_{0.5}$	X	d if X >0.95		growth after		1000/T	MFS +	Sims	Misaka
			(s)		MRX	SRX	MRX	SRX	(K^{-1})	(MPa)	(MPa)	(MPa)
F 1	0.65	0	0.44	0.99	8.8	47.2	47.2	47.2	0.79	125	103	146
F 2	0.65	0	0.53	0.92	7.3	37.0	6.9	37.8	0.81	137	125	160
F 3	0.71	0	0.85	0.67	6.4	34.7	7.8	35.7	0.83	150	132	175
F 4	0.75	0	0.43	0.78	5.8	28.3	5.9	30.0	0.84	173	154	202
F 5	0.75	0	0.93	0.39	5.3	29.9	12.6	29.9	0.84	176	181	205
F 6	0.81	0	0.90	0.32	4.9	27.7	14.7	29.2	0.85	190	182	221
F 7	0.85	0	1.05		4.8	28.1	29.2	29.2	0.86	194	200	226

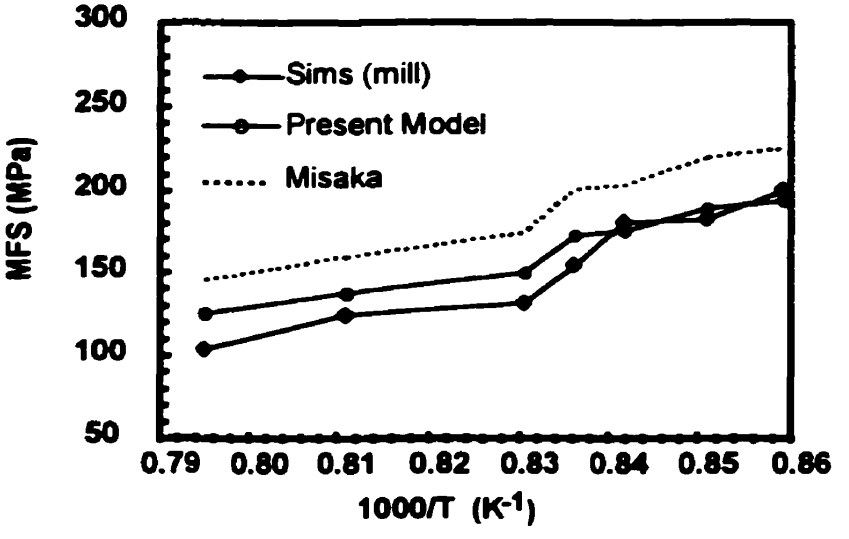

Figure 8.10 - MFS chart for grade AD10.

8.3.2 - SRX and DRX+MDRX and no Precipitation (DRX Controlled Rolling)

Considering a typical chemistry of a Nb grade, precipitation can be suppressed in several ways, e.g. by increasing the rolling temperature, decreasing the Si level, increasing the Mn, adding Ti (to tie up most of the N and C otherwise available for Nb(C,N) precipitation), and also by schedule modifications. The latter, by allowing sufficient softening between passes, prevents the strain accumulation required for the initiation of strain-induced precipitation. For the grades analyzed here, these conditions were observed in the MFS analysis, sometimes in association with each other. It is important to check the column "Sum t_{ip}/t_{ps}", which is a "measure" of the tendency for precipitation. When this ratio is greater than 1, by the additivity rule, precipitation is considered to occur.

Basically, there are two ways for DRX to take place during finishing: i) in the initial passes, where the high temperatures and low strain rates keep the critical strain low enough to be exceeded by the applied strain. The latter is usually large in the initial passes, because the steel is hotter. This mechanism is similar to the one occurring in the C-Mn grades. The other is to avoid softening by keeping the Nb in solid solution. After some strain accumulation generated due to incomplete softening between passes, if the Nb remains in solid solution, the total strain can be larger that the critical strain, initiating DRX. If precipitation occurs, however, the present model considers that there is no further softening. The grades that display SRX and DRX+MDRX and no precipitation are displayed in Spreadsheets and Figures 8.11 to 8.18. Note that the final grain sizes are quite small, especially if DRX occurs in the last passes, where the temperatures are low. In this case the grain size produced is about 7 μm. This is caused by the intense grain refinement attributable to DRX.

Typical cases of strain accumulation due to incomplete softening followed by DRX+MDRX are now presented for grades AA1, AB, AS2 and AD3.

For the AA1 grade, Spreadsheet 8.11 shows the incomplete softening after the first pass (X=0.65) quite clearly, which led to strain accumulation in

Spreadsheet 8.11 - Microstructural and MFS predictions for the AA1 grade.

Grade: AA1

strip ID
201105

C	0.05
Mn	0.35
Nb	0.035
Si	0.10
Reheat T(°C) =	1215

pass	d (μm)	T (°C)	$\dot{\varepsilon}$ (s^{-1})	i.p.time (s)	time (s)	Z (s^{-1})	K_s	t_{ps} (s)	Sum t_e/t_{ss}	PPTN?	ε	ε_a	ε_c	DRX
F 1	80.0	1024	16.7	3.21	0.01	2.3E+16	4.00	264.54	0.012	No	0.81	0.81	1.05	--
F 2	33.0	1017	31.8	1.98	3.22	6.7E+16	4.53	86.88	0.035	No	0.63	0.92	0.78	Y
F 3	21.9	994	59.0	1.27	5.19	3.2E+17	6.03	37.26	0.069	No	0.56	0.56	0.78	--
F 4	14.6	951	91.9	0.90	6.46	1.1E+18	7.68	15.86	0.126	No	0.42	0.64	0.85	--
F 5	10.8	940	116.4	0.69	7.36	2.0E+18	8.61	9.44	0.199	No	0.32	0.80	0.80	--
F 6	7.7	926	123.5		8.06	2.7E+18	9.22	8.42	0.199	No	0.21	0.80	0.74	Y

pass	$\varepsilon_{0.5}$	X_{dyn}	$t_{0.5}$ (s)	X	d if X >0.95 MRX	d if X >0.95 SRX	growth after MRX	growth after SRX	1000/T (K^{-1})	MFS + (MPa)	Sims (MPa)	Misaka (MPa)
F 1	0.70	0	2.13	0.65	10.4	41.1	33.0	33.0	0.77	118	118	142
F 2	0.59	0.039	0.10	1.00	9.1	20.9	21.9	23.1	0.78	134	133	160
F 3	0.61	0	1.00	0.59	7.4	22.0	14.6	14.6	0.79	136	146	164
F 4	0.67	0	0.95	0.24	6.3	15.5	10.8	10.8	0.82	161	167	193
F 5	0.66	0	0.66	0.26	5.8	10.8	7.7	7.7	0.82	178	198	214
F 6	0.64	0.006	0.11		5.6	8.6	7.7	7.7	0.83	185	201	222

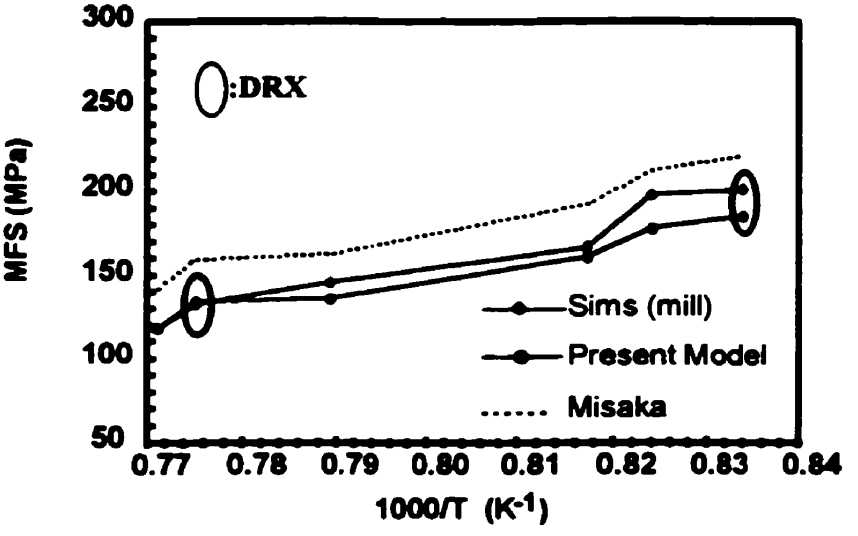

Figure 8.11 - MFS chart for grade AA1.

Spreadsheet 8.12 - Microstructural and MFS predictions for the AB grade.

Grade: AB

strip ID
1H3I2201

C	0.11
Mn	1.05
Nb	0.031
Si	0.010
Reheat T(°C) =	1220

pass	d (μm)	T (°C)	$\dot{\varepsilon}$ (s^{-1})	i.p.time (s)	time (s)	Z (s^{-1})	K_s	t_{ps} (s)	Sum t_p/t_{ss}	PPTN?	ε	ε_a	ε_c	DRX
F 1	80.0	1010	14.2	3.89	0.01	4.6E+16	5.0	153.7	0.02	No	0.78	0.78	0.88	--
F 2	40.8	970	23.7	2.80	3.90	2.1E+17	6.7	38.0	0.09	No	0.60	1.06	0.83	Y
F 3	15.8	941	32.1	2.36	6.69	6.5E+17	8.5	43.7	0.15	No	0.53	0.53	0.63	--
F 4	11.8	917	54.5	1.66	9.05	2.1E+18	10.4	20.6	0.23	No	0.48	0.70	0.68	Y
F 5	8.8	899	66.2	1.40	10.72	5.2E+18	12.7	30.7	0.27	No	0.37	0.37	0.66	--
F 6	7.4	874	90.5		12.12	1.0E+19	14.4	15.6	0.28	No	0.31	0.59	0.74	--

pass	$\varepsilon_{0.5}$	X_{dyn}	$t_{0.5}$ (s)	X	d if X >0.95 MRX	d if X >0.95 SRX	growth after MRX	growth after SRX	1000/T (K^{-1})	MFS + (MPa)	Sims (MPa)	Misaka (MPa)
F 1	0.73	0	5.11	0.41	9.5	42.3	40.8	40.8	0.78	135	151	146
F 2	0.74	0.061	0.21	1.00	7.8	22.0	15.8	17.2	0.80	167	173	180
F 3	0.67	0	1.85	0.59	6.8	18.5	11.8	11.8	0.82	160	156	172
F 4	0.71	0.0007	0.24	0.99	5.8	12.6	8.8	10.6	0.84	191	179	206
F 5	0.73	0	3.33	0.25	5.2	15.8	7.4	7.4	0.85	178	168	192
F 6	0.80	0	1.64		4.7	10.4	7.4	7.4	0.87	217	193	234

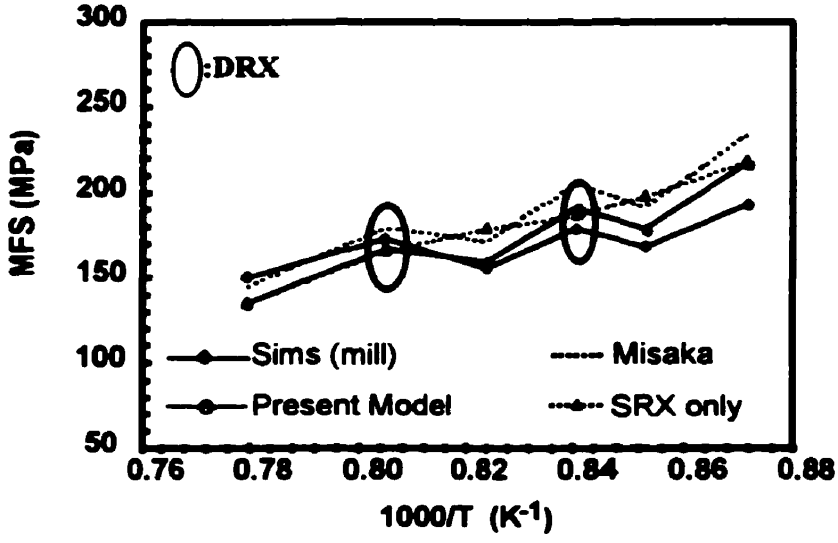

Figure 8.12 - MFS chart for grade AB.

Spreadsheet 8.13 - Microstructural and MFS predictions for the AS2 grade.

Grade: AS2

	C	0.09
	Mn	1.33
strip ID	Nb	0.036
219660	Si	0.060
(0.016% Ti)	Reheat T(°C) =	1215

pass	d (μm)	T (°C)	$\dot{\varepsilon}$ (s^{-1})	i.p.time (s)	time (s)	Z (s^{-1})	K_s	t_{ps} (s)	Sum t_p/t_{ss}	PPTN?	ε	ε_a	ε_c	DRX
F 1	80.0	1001	15.3	3.00	0.01	3.7E+16	5.03	118.2	0.03	No	0.72	0.72	0.96	--
F 2	78.1	961	24.7	2.05	3.01	1.8E+17	7.14	22.6	0.12	No	0.50	1.10	1.12	--
F 3	64.6	923	36.8	1.49	5.06	9.0E+17	9.39	8.5	0.29	No	0.40	1.38	1.33	Y
F 4	9.7	903	55.9	1.11	6.56	2.5E+18	10.60	18.2	0.35	No	0.38	0.41	0.61	--
F 5	9.6	898	85.9	0.83	7.67	4.6E+18	11.79	7.9	0.46	No	0.36	0.77	0.68	Y
F 6	6.6	882	109.4	0.65	8.50	1.0E+19	14.05	13.7	0.50	No	0.30	0.36	0.64	--
F 7	6.6	864	116.0		9.15	2.0E+19	15.44	6.8	0.50	No	0.22	0.58	0.72	--

pass	$\varepsilon_{0.5}$	X_{dyn}	$t_{0.5}$ (s)	X	d if X >0.95 MRX	d if X >0.95 SRX	growth after MRX	growth after SRX	1000/T (K^{-1})	MFS + (MPa)	Sims (MPa)	Misaka (MPa)
F 1	0.6	0	12.39	0.15	12.8	79.2	72.6	78.1	0.79	151	118	146
F 2	0.7	0	12.31	0.11	10.5	50.3	62.5	64.6	0.81	190	169	184
F 3	0.8	0	0.28	0.98	8.9	38.1	9.7	38.1	0.84	226	221	220
F 4	0.6	0	47.24	0.01	8.0	24.0	9.6	9.6	0.85	195	201	188
F 5	0.6	0.1	0.23	0.92	7.3	15.8	6.6	14.2	0.85	236	242	229
F 6	0.6	0	300.54	0.00	6.6	20.2	6.6	6.6	0.87	217	230	210
F 7	0.7	0	156.25		6.3	14.7	6.6	6.6	0.88	252	268	244

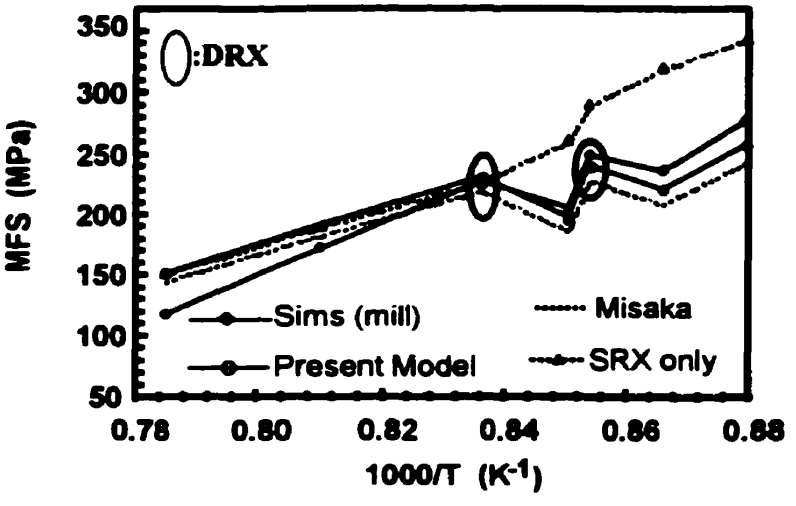

Figure 8.13 - MFS chart for grade AS2.

Spreadsheet 8.14 - Microstructural and MFS predictions for the AD3 grade.

Grade: AD3

strip ID
A12884

C	0.112
Mn	0.832
Nb	0.020
Si	0.227
Reheat T(°C) =	1215

pass	d (μm)	T (°C)	$\dot{\varepsilon}$ (s^{-1})	i.p.time (s)	time (s)	Z (s^{-1})	K_s	t_{ps} (s)	Sum t_e/t_{ss}	PPTN?	ε	ε_a	ε_c	DRX
F 1	80.0	1004	15.6	3.08	0.01	3.4E+16	5.82	33.7	0.09	No	0.64	0.64	0.78	--
F 2	68.7	977	25.5	2.07	3.09	1.2E+17	7.59	10.6	0.29	No	0.50	0.91	0.89	Y
F 3	15.4	948	44.1	1.41	5.17	4.9E+17	9.24	9.7	0.43	No	0.50	0.50	0.54	--
F 4	17.4	937	67.3	1.00	6.58	1.0E+18	10.32	5.6	0.61	No	0.41	0.62	0.65	--
F 5	17.5	926	91.4	0.74	7.57	2.0E+18	11.79	4.4	0.77	No	0.29	0.63	0.73	--
F 6	17.5	911	107.7	0.59	8.32	3.8E+18	13.59	3.3	0.95	No	0.22	0.68	0.81	--
F 7	17.4	899	111.4		8.91	5.8E+18	14.49	2.8	0.95	No	0.14	0.70	0.87	--

pass	$\varepsilon_{0.5}$	X_{dyn}	$t_{0.5}$ (s)	X	d if X >0.95 MRX	d if X >0.95 SRX	growth after MRX	growth after SRX	1000/T (K^{-1})	MFS + (MPa)	Sims (MPa)	Misaka (MPa)
F 1	0.60	0	4.85	0.36	9.4	48.2	35.5	68.7	0.78	126	116	144
F 2	0.66	0.029	0.19	1.00	8.0	34.5	15.4	15.4	0.80	153	145	174
F 3	0.53	0	1.14	0.57	6.9	18.8	6.1	17.4	0.82	154	141	175
F 4	0.58	0	1.15	0.45	6.2	17.7	7.4	17.5	0.83	174	167	198
F 5	0.62	0	1.61	0.27	5.7	17.6	10.2	17.5	0.83	186	201	212
F 6	0.67	0	1.95	0.19	5.2	16.7	12.1	17.4	0.84	200	206	228
F 7	0.71	0	2.15		5.1	16.4	17.4	17.4	0.85	208	235	237

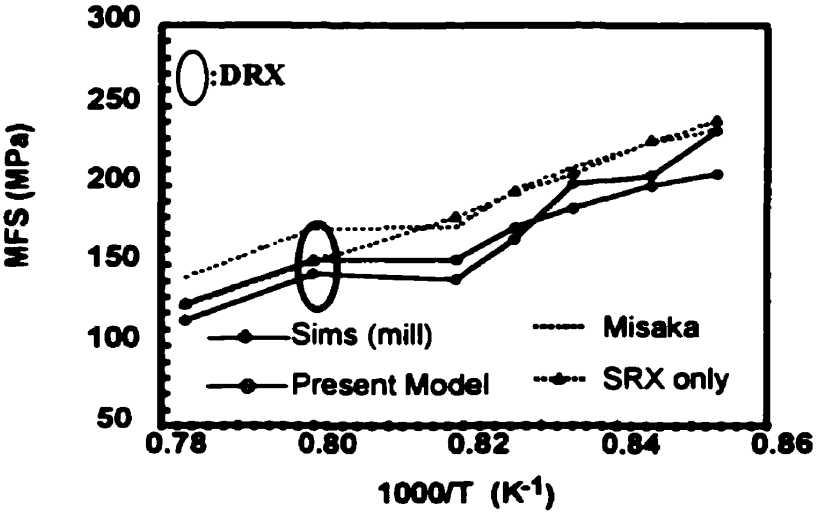

Figure 8.14 - MFS chart for grade AD3.

Spreadsheet 8.15 - Microstructural and MFS predictions for the AA2 grade.

Grade: AA2

strip ID
235215

C	0.05
Mn	0.70
Nb	0.053
Si	0.100
Reheat T(°C) =	1215

pass	d (μm)	T (°C)	$\dot{\varepsilon}$ (s^{-1})	i.p.time (s)	time (s)	Z (s^{-1})	K_S	t_{ps} (s)	Sum t_p/t_{ss}	PPTN?	ε	ε_a	ε_c	DRX
F 1	80.0	999	15.8	3.18	0.00	6.3E+16	5.83	16.52	0.193	No	0.94	0.94	0.77	Y
F 2	20.4	966	33.8	1.85	3.18	2.9E+17	7.41	9.05	0.397	No	0.68	0.68	0.52	Y
F 3	14.3	947	75.5	1.03	5.03	1.0E+18	8.54	5.38	0.588	No	0.62	0.62	0.55	Y
F 4	10.7	937	130.5	0.69	6.06	2.3E+18	9.31	4.75	0.734	No	0.48	0.48	0.55	--
F 5	10.1	929	164.2	0.47	6.75	3.7E+18	10.07	2.54	0.919	No	0.27	0.73	0.58	Y
F 6	6.3	921	205.7		7.22	5.4E+18	10.52	5.93	0.919	No	0.24	0.27	0.50	--

pass	$\varepsilon_{0.5}$	X_{dyn}	$t_{0.5}$ (s)	X	d if X >0.95 MRX	d if X >0.95 SRX	growth after MRX	growth after SRX	1000/T (K^{-1})	MFS + (MPa)	Sims (MPa)	Misaka (MPa)
F 1	0.77	0.034	0.20	1.00	9.2	37.2	20.4	21.8	0.79	136	116	152
F 2	0.65	0.043	0.17	1.00	7.5	18.5	14.3	15.9	0.81	150	134	167
F 3	0.67	0.007	0.13	1.00	6.4	15.6	10.7	12.5	0.82	168	149	189
F 4	0.67	0	5.16	0.04	5.7	15.2	10.1	10.1	0.83	175	155	196
F 5	0.69	0.035	0.10	0.96	5.4	11.0	6.3	9.2	0.83	201	217	224
F 6	0.65	0	25.83		5.1	15.7	6.3	6.3	0.84	170	188	191

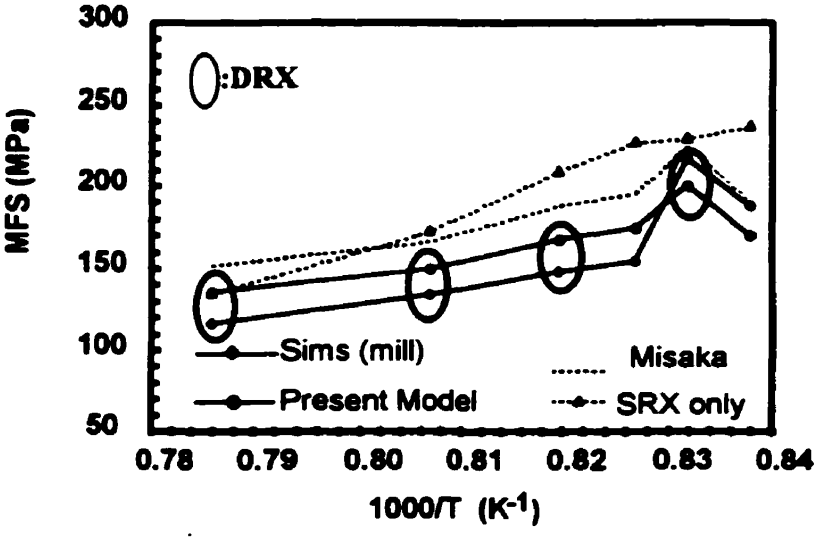

Figure 8.15 - MFS chart for grade AA2.

Spreadsheet 8.16 - Microstructural and MFS predictions for the AA3 grade.

Grade: AA3

strip ID
243205

C	0.06
Mn	0.70
Nb	0.058
Si	0.110
Reheat T(°C) =	1215

pass	d (μm)	T (°C)	$\dot{\varepsilon}$ (s^{-1})	i.p.time (s)	time (s)	Z (s^{-1})	K_s	t_{ps} (s)	Sum t_p/t_{ps}	PPTN?	ε	ε_a	ε_c	DRX
F 1	80.0	993	15.7	3.21	0.00	7.3E+16	6.16	16.55	0.194	No	0.95	0.95	0.88	Y
F 2	19.6	962	35.2	1.82	3.21	3.3E+17	7.71	9.13	0.393	No	0.72	0.72	0.58	Y
F 3	13.8	945	78.5	1.01	5.03	1.1E+18	8.78	5.87	0.565	No	0.62	0.62	0.61	Y
F 4	10.4	935	129.1	0.69	6.03	2.3E+18	9.51	5.82	0.684	No	0.44	0.45	0.61	--
F 5	10.0	928	147.1	0.49	6.73	3.4E+18	10.25	3.38	0.829	No	0.23	0.67	0.63	Y
F 6	6.1	920	183.4		7.22	4.9E+18	10.69	8.15	0.829	No	0.21	0.24	0.54	--

pass	$\varepsilon_{0.5}$	X_{dyn}	$t_{0.5}$ (s)	X	d if X >0.95 MRX	d if X >0.95 SRX	growth after MRX	growth after SRX	1000/T (K^{-1})	MFS + (MPa)	Sims (MPa)	Misaka (MPa)
F 1	0.79	0.005	0.21	1.00	9.0	37.0	19.6	21.0	0.79	138	145	155
F 2	0.65	0.0315	0.17	1.00	7.4	17.3	13.8	15.5	0.81	155	147	172
F 3	0.67	0.0001	0.13	1.00	6.3	15.1	10.4	12.2	0.82	172	163	192
F 4	0.67	0	7.67	0.03	5.7	15.7	10.0	10.0	0.83	174	160	195
F 5	0.69	0.0018	0.11	0.96	5.4	11.7	6.1	9.3	0.83	195	210	219
F 6	0.64	0	43.28		5.2	16.7	6.1	6.1	0.84	165	198	185

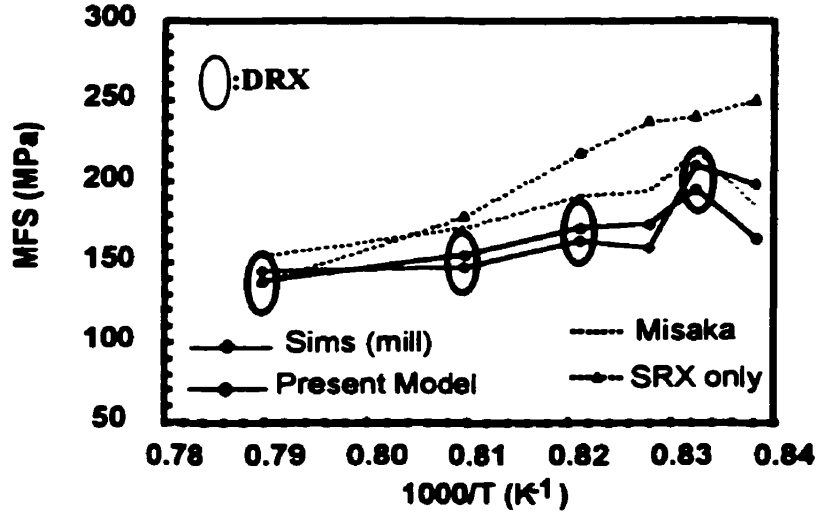

Figure 8.16 - MFS chart for grade AA3.

Spreadsheet 8.17 - Microstructural and MFS predictions for the AM1 grade.

Grade: AM1

strip ID (reference)

C	0.06
Mn	0.70
Nb	0.050
Si	0.070
Reheat T(°C) =	1250

pass	d (μm)	T (°C)	$\dot{\varepsilon}$ (s^{-1})	i.p.time (s)	time (s)	Z (s^{-1})	K_s	t_{ps} (s)	Sum t_p/t_{ps}	PPTN?	ε	ε_a	ε_c	DRX
F 1	80.0	1055	8.00	4.87	0.0	4.5E+15	4.78	66.46	0.07	No	0.70	0.70	0.60	Y
F 2	31.9	1002	19.26	2.72	4.8	4.5E+16	6.79	14.60	0.26	No	0.67	0.67	0.56	Y
F 3	20.4	973	35.06	1.69	7.5	1.8E+17	8.41	8.92	0.45	No	0.54	0.54	0.57	--
F 4	14.6	955	61.70	1.12	9.2	5.7E+17	9.67	4.93	0.68	No	0.46	0.61	0.58	Y
F 5	11.6	942	92.89	0.81	10.4	1.2E+18	10.67	6.04	0.81	No	0.36	0.36	0.59	--
F 6	11.4	934	95.81	0.67	11.2	1.6E+18	11.60	5.61	0.93	No	0.22	0.36	0.62	--
F 7	11.2	925	90.31		11.8	2.0E+18	12.11	5.90	0.93	No	0.13	0.32	0.64	--

pass	$\varepsilon_{0.5}$	X_{dyn}	$t_{0.5}$ (s)	X	d if X >0.95 MRX	d if X >0.95 SRX	growth after MRX	growth after SRX	1000/T (K^{-1})	MFS + (MPa)	Sims (MPa)	Misaka (MPa)
F 1	0.6	0.0185	0.18	1.00	11.8	26.3	31.9	31.9	0.75	106	119	119
F 2	0.61	0.0223	0.16	1.00	9.1	14.6	20.4	20.4	0.78	130	149	145
F 3	0.63	0	0.90	0.73	7.7	12.5	9.7	14.6	0.80	141	182	159
F 4	0.65	0.0252	0.13	1.00	6.7	9.3	11.6	11.6	0.81	162	203	181
F 5	0.66	0	0.60	0.61	6.1	11.2	7.6	11.4	0.82	156	189	176
F 6	0.68	0	0.74	0.47	5.9	11.1	7.2	11.2	0.83	160	171	180
F 7	0.7	0	0.83		5.8	11.8	11.2	11.2	0.83	158	182	178

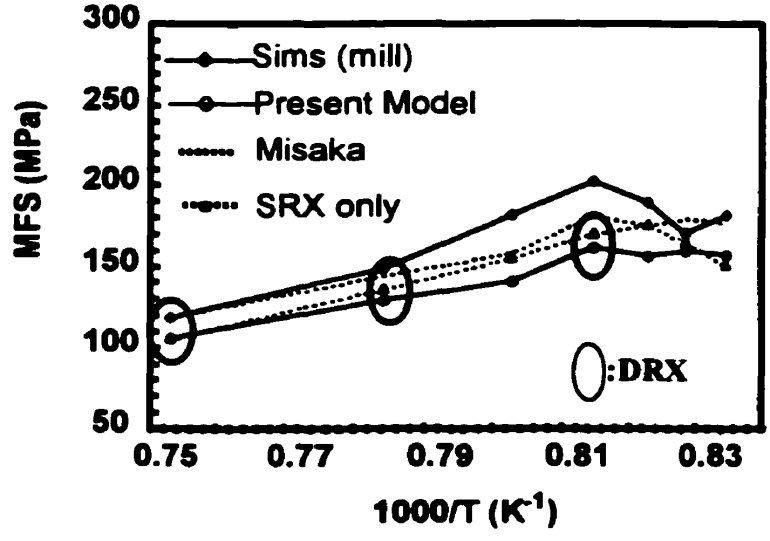

Figure 8.17 - MFS chart for grade AM1.

Spreadsheet 8.18 - Microstructural and MFS predictions for the AS1 grade.

Grade: AS1

strip ID
241675
(0.016% Ti)

C	0.07
Mn	1.12
Nb	0.023
Si	0.050
Reheat T(°C) =	1215

pass	d (μm)	T (°C)	$\dot{\varepsilon}$ (s^{-1})	i.p.time (s)	time (s)	Z (s^{-1})	K_s	t_{ps} (s)	Sum t_p/t_{ss}	PPTN?	ε	ε_a	ε_c	DRX
F 1	80.0	1021	14.2	3.37	0.01	1.9E+16	4.35	343.9	0.01	No	0.79	0.79	0.78	Y
F 2	23.3	975	26.2	2.14	3.38	1.3E+17	5.51	99.6	0.03	No	0.579	0.577	0.58	Y
F 3	16.7	966	44.8	1.45	5.53	2.9E+17	6.29	69.6	0.05	No	0.47	0.47	0.56	--
F 4	12.9	946	73.4	1.03	6.98	8.8E+17	7.36	27.2	0.09	No	0.43	0.64	0.59	Y
F 5	10.3	932	99.7	0.79	8.01	1.8E+18	8.67	36.5	0.11	No	0.33	0.33	0.60	--
F 6	10.0	911	132.6	0.61	8.79	4.7E+18	10.72	13.5	0.16	No	0.30	0.62	0.70	--
F 7	9.8	888	146.4		9.40	1.1E+19	11.99	7.4	0.16	No	0.22	0.83	0.79	Y

pass	$\varepsilon_{0.5}$	X_{dyn}	$t_{0.5}$ (s)	X	d if X >0.95 MRX	d if X >0.95 SRX	growth after MRX	growth after SRX	1000/T (K^{-1})	MFS + (MPa)	Sims (MPa)	Misaka (MPa)
F 1	0.6	0	0.17	1.00	9.8	41.8	23.3	23.3	0.77	113	105	140
F 2	0.5	0	0.17	1.00	8.2	22.6	16.7	16.7	0.8	124	129	155
F 3	0.5	0	1.20	0.57	7.2	20.8	6.5	12.9	0.81	130	151	162
F 4	0.5	0.1	0.13	1.00	6.3	14.3	10.3	10.3	0.82	156	162	192
F 5	0.5	0	13.75	0.02	5.7	18.9	10.0	10.0	0.83	144	147	180
F 6	0.6	0	11.02	0.02	5.0	12.2	9.7	9.8	0.84	178	163	222
F 7	0.7	0	0.17		4.7	9.9	9.8	9.8	0.86	203	181	251

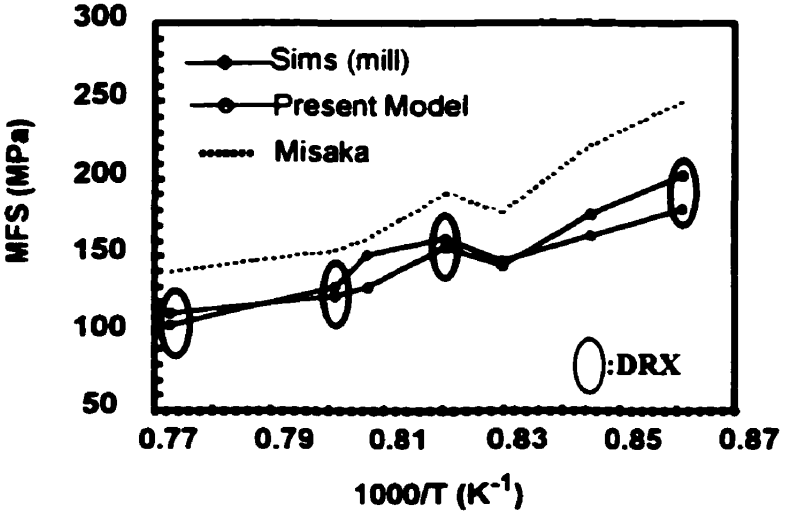

Figure 8.18 - MFS chart for grade AS1.

pass 2. As the critical strain is low due to the relatively high temperatures and low strain rates, the critical strain was passed during the deformation. With decreasing temperature and increasing strain rate, the same mechanism was again observed in the last pass, where the accumulated strain attained 0.8, compared to the nominal strain of pass 6 of 0.21. However, it was the last pass and, therefore, there is no following pass in which to detect a load drop due to DRX+MDRX softening. Precipitation was not about to occur, according to the sum of the t_{ip}/t_{ps} ratios, which was 0.199 at the last pass. Figure 8.11 indicates that the Sims (mill) MFS curve is predicted fairly well by the model. Misaka's equation clearly overpredicts the MFS.

The behavior of steel AB is displayed in Spreadsheet and Figure 8.12. This is a classic case of DRX+MDRX softening that causes MFS drops in the following passes. Incomplete softening after the first pass (X=0.41) led to a strain accumulation level of 1.06, which is greater than the critical strain (0.83). A similar situation arises after pass 3, resulting in DRX during pass 4 and a load drop in pass 5. It is important to note that this is a 6-stand mill, which forces the schedule to apply high strains in the first passes, when the temperatures are higher. It is also very common to observe higher rolling temperatures in 6-stand mills (as opposed to 7-stand HSM's). Note that if allowance is only made for SRX, the MFS drops are not predicted.

The behavior of the AS2 grade, represented by Spreadsheet and Figure 8.13, is also a good example of strain accumulation followed by dynamic softening. The small amounts of softening in the first 2 passes due to the Nb in solid solution caused the accumulated strain to rise to 1.38, which exceeded the critical strain of 1.33. The same mechanism was observed in pass 4, which led to DRX occurring during pass 5. The two DRX cycles resulted in MFS drops in the subsequent passes, 4 and 6. The small addition of 0.016% Ti combines with most of the N at high temperatures, leaving the Nb largely in solid solution (see discussion in section 4.1.1) during finish rolling. This effect, associated with the high Mn (1.33%) and low Si (0.06%) contents, completely eliminated Nb carbonitride precipitation. According to Figure 8.13, the Sims MFS is well predicted by the present model. In this particular case, allowance for SRX only results in a severe overprediction of the MFS after the first cycle of DRX. On the other hand, Misaka's equation predicts the mill behavior quite well. This is because the high Mn had increased the actual MFS, compensating for the generally observed overprediction of the Misaka relation. This demonstrates

one more time the effectiveness of the chemical compositional term of the new MFS equation.

The AD3 grade had just one cycle of DRX in the second pass and DRX was absent in the later passes, as can be seen in Spreadsheet and Figure 8.14. After 36% softening after the first pass, the addition of the 0.5 strain applied in the second pass triggered DRX. During the remaining passes, the critical strains remained high due to the low Nb and relatively high Mn levels as well as the temperature and strain rate conditions. Figure 8.14 displays the Sims MFS curve, which is fitted quite well by the prediction. One more time, Misaka's equation overpredicts the MFS and the lack of allowance for DRX leads to values that are clearly too high after the second pass, which is where DRX+MDRX occurs. The relatively high Mn, associated with the low Nb level, prevented the occurrence of Nb carbonitride precipitation. Note that the final grain size is large, when compared to the other grades of the present subgroup. This is because there was only one cycle of DRX; it refined the grain size from 68.7 to 15.4 μm.

Some cases of dynamic softening occurring after the first pass will now be shown; this affects grades AA2, AA3, AS1 and AM1.

The AA2, AA3 and AM1 grades (Spreadsheets and Figures 8.15, 8.16 and 8.17, respectively) display several cycles of DRX in their schedules. This multiple-cycle behavior is attributable to the higher Nb content, which decreased the critical strain ratio. The three grades were rolled under similar conditions (except for the AM1 grade) using higher temperatures in the early passes. In grades AA2 and AA3, DRX occurred in four out of six passes. All three steels, because of their relatively high Nb contents, were about to exhibit precipitation; this is evident from the column "Sum t_{ip}/t_{ps}", where the values are close to the unity. For these cases, the intense softening caused by DRX removed the strain which would otherwise have accelerated the initiation of precipitation. Figures 8.15 to 8.17 show that the Sims MFS values are quite well predicted by both the Misaka equation and the present model. The higher Nb and Mn contents of these grades raised the flow stress levels and in this way compensated for the overpredictions generally observed when the Misaka relation is employed. If no allowance is made for DRX, the predicted values are clearly too high.

Finally, Spreadsheet and Figure 8.18 display the results for grade AS1. In this case, a transition between the two subgroups analyzed above is observed. This is a low Nb (0.023%), high Mn (1.12%) steel, with Ti added to a level of 0.016%. As

in the case of grade AS2, the Ti combines with the N at the higher temperatures, leaving the Nb largely in solid solution. In this way, precipitation is avoided, and is not in fact about to begin, according to the "Sum" parameter in the spreadsheet. As the first pass temperature was quite high, the critical strain was decreased, allowing DRX to take place. In the second pass, the total strain and critical strain are very close, leading to a borderline DRX situation. This seems to be responsible for the shallow slope in the predicted MFS curve, which fits the (observed) Sims curve in this way.

8.3.3 - SRX and DRX+MDRX and Precipitation in the Final Passes

The combination of DRX+MDRX followed by strain accumulation due to Nb carbonitride precipitation appears to be the most attractive schedule for hot strip rolling. This is because there is at least one DRX cycle somewhere in the early passes, which causes intense grain refinement. After that, precipitation occurs, which leads to full strain accumulation. The latter is desirable in order to produce a fine ferrite grain size after transformation. From a mill operational point of view, this type of behavior allows strain accumulation to be accomplished at relatively low rolling forces, because of the occurrence of DRX+MDRX early in the schedule.

The AD1, AD2, AD5, AD6, AD7 and AD8 grades displayed the above behavior in this analysis, as represented by Spreadsheets and Figures 8.19 to 8.24. There include two pairs of 'coupled' steels: AD5 & AD6, and AD7 & AD8. Each pair involves a high-Si and low-Si version of the same base composition, which helps to establish the effect of Si addition.

In steel AD1, DRX occurred in the third pass, after some strain accumulation due to incomplete softening by SRX in the first two passes. Note that the grain structure is intensely refined by MDRX. The modified Dutta and Sellars model

Spreadsheet 8.19 - Microstructural and MFS predictions for the AD1 grade.

Grade: AD1

strip ID
A22144

C	0.060
Mn	0.650
Nb	0.020
Si	0.225
Reheat T(°C) =	1215

pass	d (μm)	T (°C)	$\dot{\varepsilon}$ (s^{-1})	i.p.time (s)	time (s)	Z (s^{-1})	K_s	t_{ps} (s)	Sum t_w/t_{ss}	PPTN?	ε	ε_a	ε_c	DRX
F 1	80.0	985	12.6	3.45	0.01	4.7E+16	6.98	28.9	0.12	No	0.55	0.55	0.86	--
F 2	95.2	960	20.6	2.35	3.46	1.6E+17	8.87	8.7	0.39	No	0.49	0.97	1.03	--
F 3	84.8	936	30.7	1.70	5.81	4.9E+17	10.48	4.4	0.77	No	0.40	1.18	1.18	Y
F 4	10.6	927	48.0	1.25	7.51	1.0E+18	11.44	9.1	0.91	No	0.41	0.42	0.47	--
F 5	13.3	919	68.8	0.93	8.76	1.9E+18	12.51	5.5	1.08	Y	0.32	0.55	0.59	--
F 6	13.3	910	89.8	0.71	9.68	3.3E+18	13.91	3.0	1.30	Y	0.28	0.83	0.64	--
F 7	13.3	899	91.7		10.39	4.8E+18	14.76	2.2	1.30	Y	0.16	0.99	0.69	--

pass	$\varepsilon_{0.5}$	X_{dyn}	$t_{0.5}$ (s)	X	d if X >0.95 MRX	d if X >0.95 SRX	growth after MRX	growth after SRX	1000/T (K^{-1})	MFS + (MPa)	Sims (MPa)	Misaka (MPa)
F 1	0.68	0	17.73	0.13	9.1	62.1	76.9	95.2	0.79	118	142	136
F 2	0.76	0	7.57	0.19	7.7	41.2	62.8	84.8	0.81	149	150	172
F 3	0.83	0.002	0.25	0.99	6.9	33.3	10.6	10.6	0.83	172	193	198
F 4	0.53	0	1.46	0.45	6.3	16.6	5.4	13.3	0.83	149	178	172
F 5	0.59	0	1.49	0.00	5.8	16.1	13.3	13.3	0.84	185	213	194
F 6	0.62	0	0.72	0.00	5.4	12.2	13.3	13.3	0.85	213	219	223
F 7	0.66	0	0.54		5.2	10.8	13.3	13.3	0.85	227	244	238

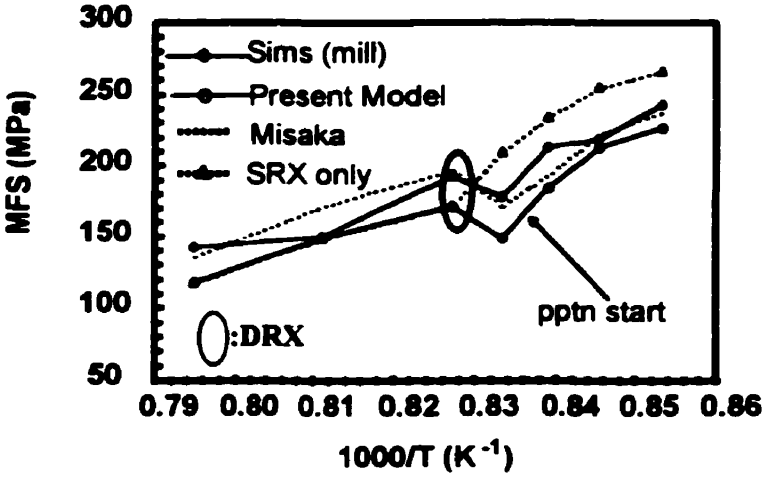

Figure 8.19 - MFS chart for grade AD1.

Spreadsheet 8.20 - Microstructural and MFS predictions for the AD2 grade.

Grade: AD2

strip ID
E20942

C	0.131
Mn	0.641
Nb	0.018
Si	0.230
Reheat T(°C) =	1215

pass	d (μm)	T (°C)	$\dot{\varepsilon}$ (s^{-1})	i.p.time (s)	time (s)	Z (s^{-1})	K_s	t_{ps} (s)	Sum t_p/t_{ps}	PPTN?	ε	ε_a	ε_c	DRX
F 1	80.0	976	12.1	3.91	0.01	5.9E+16	7.79	17.5	0.22	No	0.77	0.77	0.86	--
F 2	65.7	947	24.0	2.37	3.92	2.7E+17	9.50	6.0	0.62	No	0.60	1.08	1.01	Y
F 3	13.2	936	51.2	1.43	6.30	8.3E+17	10.63	6.2	0.85	No	0.64	0.64	0.54	Y
F 4	10.4	925	89.8	0.92	7.73	2.0E+18	12.04	5.5	1.01	Y	0.50	0.50	0.56	--
F 5	10.4	912	119.4	0.64	8.65	4.1E+18	13.74	2.7	1.25	Y	0.30	0.81	0.63	--
F 6	10.4	900	165.4	0.46	9.29	8.4E+18	15.81	1.6	1.52	Y	0.27	1.08	0.72	--
F 7	10.4	886	191.7		9.75	1.5E+19	17.08	1.1	1.52	Y	0.19	1.26	0.80	--

pass	$\varepsilon_{0.5}$	X_{dyn}	$t_{0.5}$ (s)	X	d if X >0.95 MRX	d if X >0.95 SRX	growth after MRX	growth after SRX	1000/T (K^{-1})	MFS + (MPa)	Sims (MPa)	Misaka (MPa)
F 1	0.66	0	5.66	0.38	8.7	42.5	33.1	65.7	0.80	133	132	154
F 2	0.74	0.12	0.25	1.00	7.4	29.8	13.2	13.2	0.82	168	164	192
F 3	0.54	0.23	0.18	1.00	6.4	14.4	10.4	10.4	0.83	175	161	195
F 4	0.55	0	0.94	0.00	5.7	14.5	10.4	10.4	0.83	185	192	204
F 5	0.59	0	0.39	0.00	5.2	10.6	10.4	10.4	0.84	219	235	241
F 6	0.63	0	0.27	0.00	4.7	8.7	10.4	10.4	0.85	249	250	275
F 7	0.68	0	0.22		4.5	7.8	10.4	10.4	0.86	272	274	299

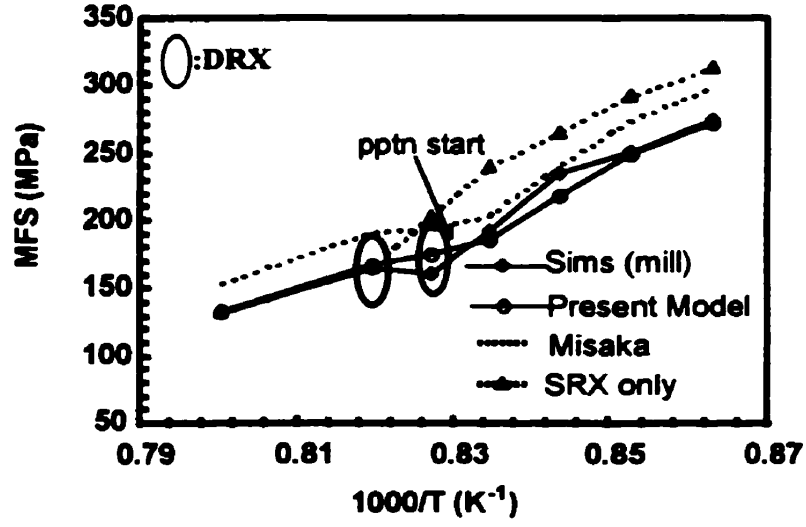

Figure 8.20 - MFS chart for grade AD2.

Spreadsheet 8.21 - Microstructural and MFS predictions for the AD5 grade.

Grade: AD5

strip ID
A20112

C	0.06
Mn	0.65
Nb	0.030
Si	0.115
Reheat T(°C) =	1215

pass	d (μm)	T (°C)	$\dot{\varepsilon}$ (s^{-1})	i.p.time (s)	time (s)	Z (s^{-1})	K_s	t_{ps} (s)	Sum t_p/t_{ss}	PPTN?	ε	ε_a	ε_c	DRX
F 1	80.0	1011	13.6	3.60	0.01	2.4E+16	5.24	15.9	0.23	No	0.74	0.74	0.74	--
F 2	64.7	982	25.5	2.24	3.61	1.0E+17	6.82	4.2	0.76	No	0.58	1.01	0.86	Y
F 3	16.5	953	48.8	1.41	5.85	4.7E+17	8.04	3.3	1.18	Y	0.58	0.58	0.56	--
F 4	16.5	947	91.0	0.89	7.26	1.0E+18	8.44	1.1	1.95	Y	0.54	1.12	0.64	--
F 5	16.5	943	139.2	0.59	8.15	1.8E+18	9.03	0.6	2.81	Y	0.36	1.48	0.70	--
F 6	16.5	933	180.2	0.43	8.75	3.2E+18	10.01	0.4	3.75	Y	0.27	1.76	0.77	--
F 7	16.5	922	199.8		9.17	5.0E+18	10.58	0.3	3.75	Y	0.17	1.93	0.83	--

pass	$\varepsilon_{0.5}$	X_{dyn}	$t_{0.5}$ (s)	X	d if X >0.95 MRX	d if X >0.95 SRX	growth after MRX	growth after SRX	1000/T (K^{-1})	MFS + (MPa)	Sims (MPa)	Misaka (MPa)
F 1	0.58	0	4.56	0.42	9.8	43.6	29.9	64.7	0.78	122	115	140
F 2	0.64	0.29	0.18	1.00	8.1	30.8	16.5	16.5	0.80	153	137	171
F 3	0.53	0	0.96	0.00	7.0	17.8	16.5	16.5	0.82	153	139	175
F 4	0.56	0	0.36	0.00	6.3	11.5	16.5	16.5	0.82	192	165	221
F 5	0.58	0	0.27	0.00	5.8	9.5	16.5	16.5	0.82	217	220	249
F 6	0.61	0	0.27	0.00	5.4	8.5	16.5	16.5	0.83	238	227	273
F 7	0.65	0	0.27		5.2	8.0	16.5	16.5	0.84	251	246	288

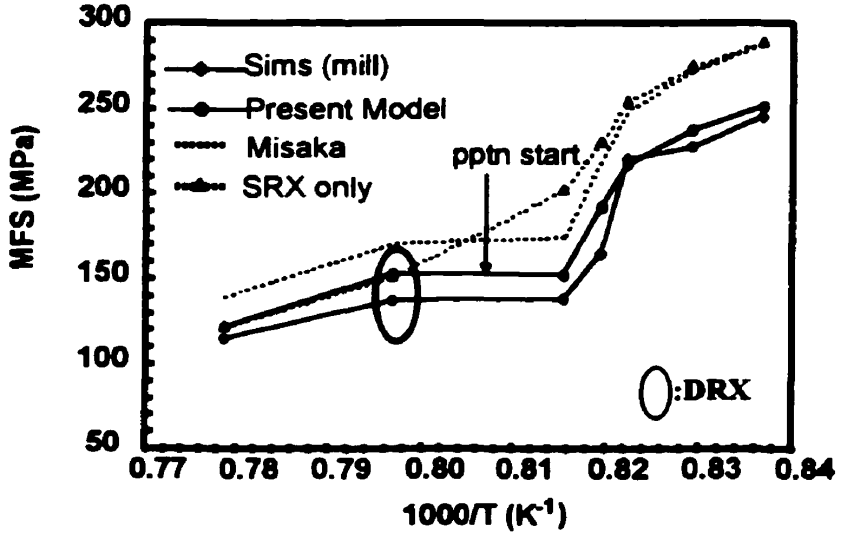

Figure 8.21 - MFS chart for grade AD5.

Spreadsheet 8.22 - Microstructural and MFS predictions for the AD6 grade.

Grade: AD6

strip ID
A73650

C	0.061
Mn	0.699
Nb	0.035
Si	0.009
Reheat T(°C) =	1215

pass	d (μm)	T (°C)	$\dot{\varepsilon}$ (s^{-1})	i.p.time (s)	time (s)	Z (s^{-1})	K_s	t_{ps} (s)	Sum t_e/t_{ss}	PPTN?	ε	ε_a	ε_c	DRX
F 1	80.0	1000	14.2	3.54	0.01	3.5E+16	5.29	23.1	0.15	No	0.79	0.79	0.81	--
F 2	67.9	968	25.9	2.23	3.55	1.6E+17	6.52	6.0	0.52	No	0.57	1.11	0.96	Y
F 3	15.4	952	46.7	1.45	5.78	4.6E+17	7.39	6.9	0.73	No	0.54	0.54	0.55	--
F 4	16.9	940	84.3	0.94	7.23	1.2E+18	8.02	3.2	1.02	Y	0.53	0.73	0.68	--
F 5	16.9	934	141.1	0.61	8.17	2.4E+18	8.76	1.5	1.43	Y	0.40	1.13	0.76	--
F 6	16.9	921	181.0	0.43	8.78	4.6E+18	10.01	0.9	1.89	Y	0.27	1.40	0.85	--
F 7	16.9	906	197.1		9.21	8.2E+18	10.76	0.6	1.89	Y	0.16	1.57	0.94	--

pass	$\varepsilon_{0.5}$	X_{dyn}	$t_{0.5}$ (s)	X	d if X >0.95 MRX	d if X >0.95 SRX	growth after MRX	growth after SRX	1000/T (K^{-1})	MFS + (MPa)	Sims (MPa)	Misaka (MPa)
F 1	0.61	0	6.43	0.32	9.3	42.0	39.3	67.9	0.79	129	115	146
F 2	0.68	0.253	0.19	1.00	7.9	30.0	15.4	15.4	0.81	162	152	180
F 3	0.52	0	1.04	0.62	6.9	17.9	5.9	16.9	0.82	153	148	173
F 4	0.58	0	1.08	0.00	6.2	15.6	16.9	16.9	0.82	180	165	204
F 5	0.61	0	0.79	0.00	5.6	11.6	16.9	16.9	0.83	213	207	241
F 6	0.65	0	0.89	0.00	5.1	10.1	16.9	16.9	0.84	237	235	268
F 7	0.70	0	0.95		4.9	9.4	16.9	16.9	0.85	253	275	287

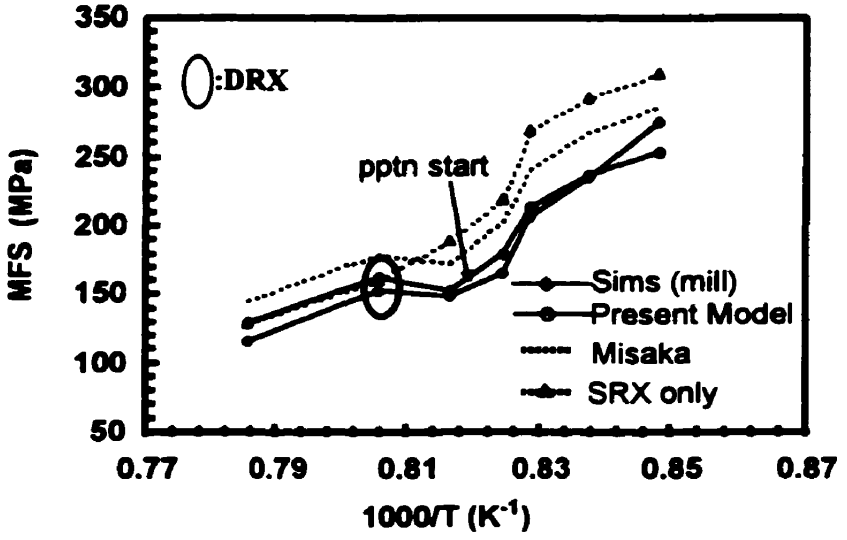

Figure 8.22 - MFS chart for grade AD6.

Spreadsheet 8.23 - Microstructural and MFS predictions for the AD7 grade.

Grade: AD7

strip ID
T37450

C	0.06
Mn	0.65
Nb	0.045
Si	0.115
Reheat T(°C) =	1215

pass	d (μm)	T (°C)	$\dot{\varepsilon}$ (s^{-1})	i.p.time (s)	time (s)	Z (s^{-1})	K_s	t_{ps} (s)	Sum t_e/t_{ss}	PPTN?	ε	ε_a	ε_c	DRX
F 1	80.0	1008	16.4	3.26	0.01	3.2E+16	5.45	11.1	0.29	No	0.92	0.92	1.03	--
F 2	66.0	976	35.0	1.85	3.27	1.7E+17	6.79	2.7	0.96	No	0.67	1.28	1.24	Y
F 3	15.9	960	63.1	1.18	5.12	4.9E+17	7.74	3.6	1.28	Y	0.55	0.55	0.73	--
F 4	15.9	948	113.2	0.76	6.30	1.2E+18	8.94	1.2	1.90	Y	0.50	1.05	0.85	--
F 5	15.9	930	148.7	0.50	7.06	2.9E+18	10.53	0.7	2.61	Y	0.27	1.32	0.98	--
F 6	15.9	915	194.5	0.39	7.56	6.1E+18	12.19	0.4	3.44	Y	0.24	1.56	1.12	--
F 7	15.9	901	225.6		7.95	1.1E+19	13.11	0.3	3.44	Y	0.17	1.72	1.24	--

pass	$\varepsilon_{0.5}$	X_{dyn}	$t_{0.5}$ (s)	X	d if X >0.95 MRX	d if X >0.95 SRX	growth after MRX	growth after SRX	1000/T (K^{-1})	MFS + (MPa)	Sims (MPa)	Misaka (MPa)
F 1	0.59	0	5.60	0.33	9.4	37.8	37.9	66.0	0.78	132	123	151
F 2	0.67	0.08	0.14	1.00	7.8	26.6	15.9	15.9	0.80	167	151	189
F 3	0.51	0	0.77	0.00	6.9	18.1	15.9	15.9	0.81	155	152	176
F 4	0.56	0	0.81	0.00	6.0	11.7	15.9	15.9	0.82	196	177	223
F 5	0.61	0	1.13	0.00	5.4	10.1	15.9	15.9	0.83	221	236	252
F 6	0.66	0	1.55	0.00	4.9	9.0	15.9	15.9	0.84	245	246	279
F 7	0.71	0	1.80		4.7	8.4	15.9	15.9	0.85	263	280	299

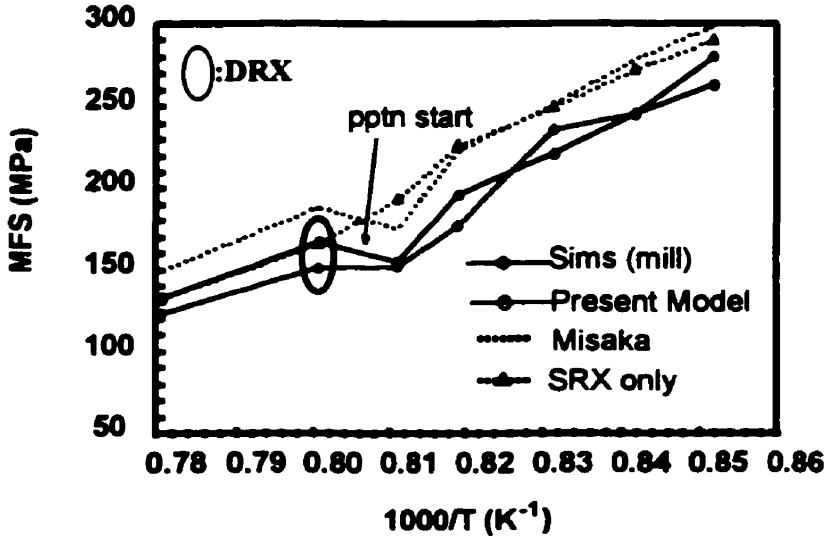

Figure 8.23 - MFS chart for grade AD7.

Spreadsheet 8.24 - Microstructural and MFS predictions for the AD8 grade.

Grade: AD8

strip ID
A73651

C	0.061
Mn	0.699
Nb	0.047
Si	0.009
Reheat T(°C) =	1215

pass	d (μm)	T (°C)	$\dot{\varepsilon}$ (s^{-1})	i.p.time (s)	time (s)	Z (s^{-1})	K_s	t_{ps} (s)	Sum t_p/t_{ps}	PPTN?	ε	ε_a	ε_c	DRX
F 1	80.0	1001	14.5	3.55	0.01	3.4E+16	5.32	20.1	0.18	No	0.85	0.85	0.89	--
F 2	66.9	967	25.8	2.26	3.56	1.6+17	6.65	5.5	0.59	No	0.56	1.13	1.06	Y
F 3	15.3	950	46.9	1.47	5.82	4.9E+17	7.61	6.3	0.82	No	0.55	0.55	0.61	--
F 4	16.8	937	84.2	0.95	7.30	1.3E+18	8.31	2.9	1.14	Y	0.52	0.73	0.75	--
F 5	16.8	931	141.1	0.62	8.24	2.6E+18	9.21	1.3	1.58	Y	0.40	1.12	0.85	--
F 6	16.8	915	172.8	0.44	8.87	5.3E+18	10.74	0.8	2.08	Y	0.25	1.37	0.96	--
F 7	16.8	899	179.6		9.31	9.4E+18	11.62	0.6	2.08	Y	0.14	1.52	1.05	--

pass	$\varepsilon_{0.5}$	X_{dyn}	$t_{0.5}$ (s)	X	d if X >0.95 MRX	d if X >0.95 SRX	growth after MRX	growth after SRX	1000/T (K^{-1})	MFS + (MPa)	Sims (MPa)	Misaka (MPa)
F 1	0.60	0	6.24	0.33	9.3	39.9	38.4	66.9	0.78	130	112	148
F 2	0.68	0.136	0.19	1.00	7.8	29.3	15.3	15.3	0.81	160	154	180
F 3	0.52	0	1.05	0.62	6.8	17.7	5.8	16.8	0.82	152	150	173
F 4	0.58	0	1.21	0.00	6.1	15.6	16.8	16.8	0.83	179	169	204
F 5	0.61	0	1.02	0.00	5.5	11.6	16.8	16.8	0.83	213	208	242
F 6	0.67	0	1.29	0.00	5.0	10.2	16.8	16.8	0.84	235	238	268
F 7	0.72	0	1.46		4.8	9.5	16.8	16.8	0.85	250	284	284

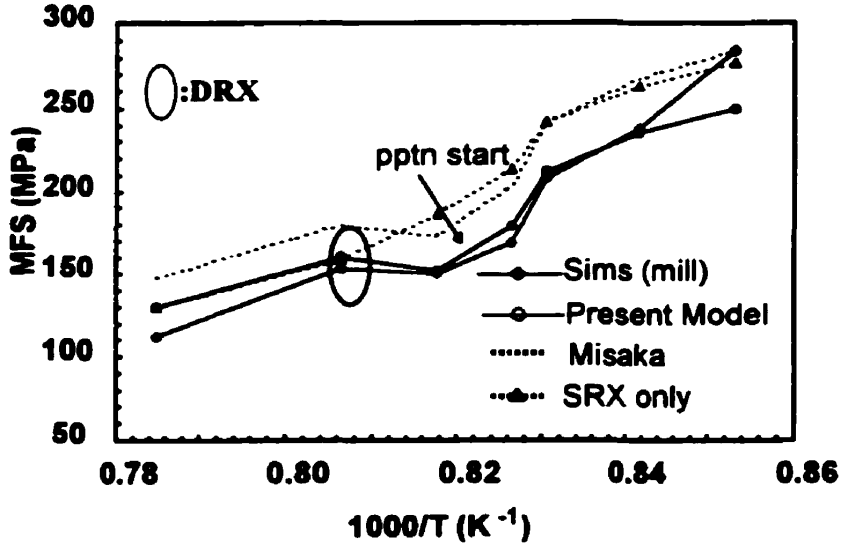

Figure 8.24 - MFS chart for grade AD8.

predicts that precipitation occurs between the fourth and fifth passes. Although the steel has quite a low Nb content, it contains 0.23% Si, which accelerates precipitation. It was also rolled at relatively low temperatures, a condition that increases the driving force for precipitation. The strain accumulated after the last pass was 0.99. The mill MFS curve is predicted fairly well, including the MFS drop caused by DRX+MDRX at pass 3. The Misaka prediction is good too, despite the initiation of DRX. There is an additional Misaka MFS curve showing that use of the accumulated strain in the model has considerable importance. Also, if the model does not allow for DRX, the MFS values are overpredicted.

Similar remarks can be made for grade AD2, represented by Spreadsheet and Figure 8.20. It had also been rolled at relatively low temperatures, but there are two major differences: the carbon content is slightly higher, and the strains applied were also greater than the ones employed in the AD1 schedule. These factors led to 2 differences in behavior: (i) precipitation started earlier, between passes 3 and 4, due to the higher carbon level, and (ii) there were two cycles of DRX, which caused intense grain refinement between passes 2 and 3. The strain accumulated in this schedule was 1.26, a somewhat higher amount than in the AD1 schedule; this is because precipitation began sooner. Figure 8.20 shows clearly that the allowance for DRX is responsible for the good fit to the Sims (mill) MFS curve.

Similar processing parameters apply to the 'coupled' pair, AD5 and AD6; these include the temperatures, reductions and strain rates. Both display a DRX cycle in the second stand due to the addition of the strain retained from the first pass due to incomplete softening. The grain sizes produced are similar too, about 17 μm. However, there is a slight difference in the precipitation behavior, which suggests that this is influenced by the different Si contents. In grade AD5, precipitation began sooner, between passes 2 and 3; in grade AD6, precipitation was initiated between passes 3 and 4. The same observations apply to the second pair, AD7 (high Si) and AD8 (low Si), represented by Spreadsheets and Figures 8.23 and 8.24, respectively. The high Si version experienced precipitation sooner for the same base composition and similar processing conditions (although the applied strains in the first two passes were slightly greater in the AD7 grade). At the end of the schedule, the retained strains were 1.93 in steel AD5 (in which precipitation began sooner) and 1.57 in steel AD6 (in which precipitation began later). In a similar way, the retained strains were 1.72 in AD7 (high Si) and 1.52 in AD8 (low Si). The Sims (mill) MFS curves are

well predicted for both grades, and again, the Misaka MFS values are too high, partly because no allowance is made for DRX.

The subtle trends deduced from the mill log analysis are not precise enough to *prove* conclusively the effect of Si addition on the precipitation kinetics of Nb(C,N). For this reason, further studies using mechanical testing and TEM will be necessary to quantify and confirm this influence.

8.3.4 - SRX and Precipitation (Conventional Controlled Rolling)

Among all the Nb grades analyzed, there was a total absence of DRX in only three, according to the present model. The reductions in the initial passes were not large (e.g. a total of 0.9 or so) in these particular schedules, which is why the critical strain was not exceeded and why DRX was not initiated. The grades can be divided into two groups, the low Nb AD4 and the two high Nb grades, AD11 and AD12. These are represented by Spreadsheets and Figures 8.25 to 8.27.

The applied strains remained small throughout the schedule employed for the AD4 steel. It had been rolled at unusually low temperatures, starting at 967°C and finishing at 858°C. These two factors led to interesting behavior regarding the grain size evolution and precipitation of the Nb carbonitrides. Firstly, DRX did not occur, mainly because of the low applied strains. As a result, there was very little grain refinement up to the last pass. Secondly, the relatively low temperatures, as well as the presence of 0.221% Si and 0.114% C, promoted precipitation, even at a Nb level of 0.022% and a relatively high Mn content (0.99%). According to this analysis, precipitation occurred between the third and fourth passes, and the strain accumulation attained 1.6 in the last stand. The Sims (mill) MFS is well predicted by the model; both display smooth increases, as can be seen in Figure 8.25. The Misaka MFS values are somewhat above the Sims curve, showing once again the effectiveness of the chemical composition factor used in the new MFS equation.

Spreadsheet 8.25 - Microstructural and MFS predictions for the AD4 grade.

Grade: AD4

strip ID
A38771

C	0.114
Mn	0.989
Nb	0.022
Si	0.221
Reheat T(°C) =	1215

pass	d (μm)	T (°C)	$\dot{\varepsilon}$ (s^{-1})	i.p.time (s)	time (s)	Z (s^{-1})	K_s	t_{ps} (s)	Sum t_p/t_{ss}	PPTN?	ε	ε_a	ε_c	DRX
F 1	80.0	967	8.5	4.28	0.01	5.4E+16	8.20	38.73	0.11	No	0.35	0.35	0.88	--
F 2	79.6	939	9.6	3.56	4.29	1.4E+17	10.89	16.16	0.33	No	0.25	0.58	1.03	--
F 3	77.9	910	12.5	2.96	7.85	4.6E+17	13.70	7.93	0.70	No	0.26	0.80	1.25	--
F 4	75.6	895	14.8	2.50	10.81	8.9E+17	15.83	5.47	1.16	Y	0.23	0.98	1.37	--
F 5	75.6	883	19.8	2.08	13.30	1.7E+18	18.16	3.71	1.72	Y	0.23	1.22	1.55	--
F 6	75.6	870	22.4	1.76	15.39	3.1E+18	20.89	2.94	2.32	Y	0.19	1.41	1.70	--
F 7	75.6	858	27.5		17.14	5.8E+18	17.76	1.52	2.32	Y	0.19	1.60	1.89	--

pass	$\varepsilon_{0.5}$	X_{dyn}	$t_{0.5}$ (s)	X	d if X >0.95 MRX	d if X >0.95 SRX	growth after MRX	growth after SRX	1000/T (K^{-1})	MFS + (MPa)	Sims (MPa)	Misaka (MPa)
F 1	0.67	0	58.26	0.05	8.9	72.5	72.4	79.6	0.81	115	103	126
F 2	0.76	0	38.81	0.06	7.8	51.4	70.3	77.9	0.83	138	133	151
F 3	0.88	0	32.64	0.06	6.9	40.7	68.9	75.6	0.85	163	154	179
F 4	0.94	0	28.58	0.00	6.3	34.9	75.6	75.6	0.86	180	172	197
F 5	1.01	0	25.34	0.00	5.8	30.2	75.6	75.6	0.87	201	189	220
F 6	1.08	0	26.61	0.00	5.4	27.4	75.6	75.6	0.87	217	215	238
F 7	1.16	0	12.83		5.1	25.2	75.6	75.6	0.88	236	247	259

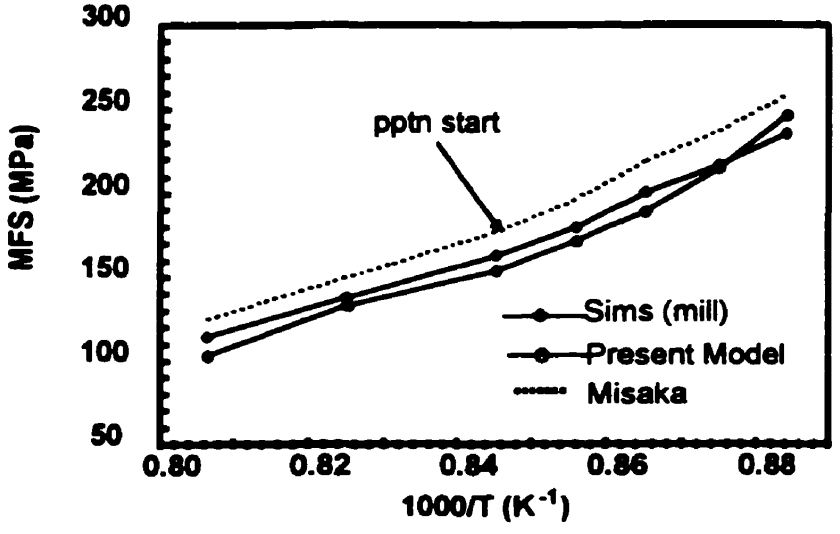

Figure 8.25 - MFS chart for grade AD4.

Spreadsheet 8.26 - Microstructural and MFS predictions for the AD11 grade.

Grade: AD11

	C	0.06
	Mn	1.25
strip ID	Nb	0.075
A20781	Si	0.325
(Ti: 0..024%)	Reheat T(°C) =	1215

pass	d (μm)	T (°C)	$\dot{\varepsilon}$ (s^{-1})	i.p.time (s)	time (s)	Z (s^{-1})	K_s	t_{ps} (s)	Sum t_p/t_{ps}	PPTN?	ε	ε_a	ε_c	DRX
F 1	80.0	1023	13.3	3.50	0.00	1.7E+16	5.10	20.46	0.17	No	0.60	0.60	0.83	--
F 2	40.4	992	22.2	2.35	3.50	6.9E+16	6.91	7.86	0.47	No	0.50	0.63	0.74	--
F 3	20.4	958	33.1	1.70	5.85	2.7E+17	8.78	4.25	0.87	No	0.41	0.48	0.67	--
F 4	20.0	943	45.6	1.28	7.55	5.9E+17	10.06	2.69	1.35	Y	0.33	0.78	0.76	--
F 5	19.3	931	65.2	0.98	8.83	1.2E+18	11.57	1.81	1.89	Y	0.30	1.08	0.86	--
F 6	18.8	916	74.8	0.76	9.81	2.2E+18	13.63	1.39	2.44	Y	0.22	1.29	0.95	--
F 7	18.6	900	74.7		10.57	3.8E+18	14.86	1.08	2.44	Y	0.13	1.42	1.04	--

pass	$\varepsilon_{0.5}$	X_{dyn}	$t_{0.5}$ (s)	X	d if X >0.95 MRX	d if X >0.95 SRX	growth after MRX	growth after SRX	1000/T (K^{-1})	MFS + (MPa)	Sims (MPa)	Misaka (MPa)
F 1	0.55	0	0.66	0.78	10.2	29.3	11.2	40.4	0.77	140	138	130
F 2	0.54	0	0.30	0.89	8.5	17.9	7.8	20.4	0.79	160	154	149
F 3	0.53	0	8.76	0.05	7.3	13.6	18.4	20.0	0.81	170	174	158
F 4	0.57	0	5.32	0.00	6.7	9.7	20.0	20.0	0.82	203	201	188
F 5	0.62	0	5.80	0.00	6.0	7.8	20.0	20.0	0.83	233	223	216
F 6	0.66	0	11.29	0.00	5.6	6.9	20.0	20.0	0.84	254	244	236
F 7	0.72	0	15.99		5.4	6.5	20.0	20.0	0.85	268	272	250

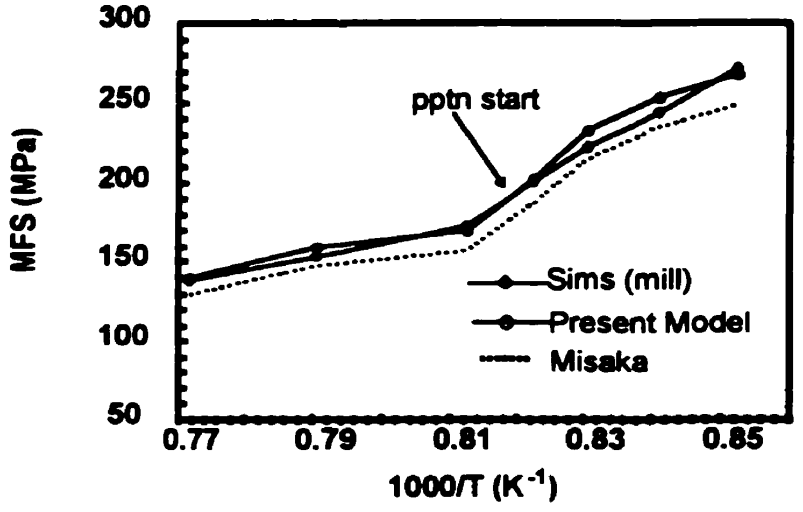

Figure 8.26 - MFS chart for grade AD11.

Spreadsheet 8.27 - Microstructural and MFS predictions for the AD12 grade.

Grade: AD12

strip ID
A20790

C	0.06
Mn	1.25
Nb	0.08
Si	0.325
Reheat T(°C) =	1215

pass	d (μm)	T (°C)	$\dot{\varepsilon}$ (s^{-1})	i.p.time (s)	time (s)	Z (s^{-1})	K_s	t_{ps} (s)	Sum tip/tps	PPTN?	ε	ε_a	ε_c	DRX
F 1	80.0	999	13.4	3.52	0.00	3.4E+16	5.56	12.78	0.28	No	0.62	0.62	1.06	--
F 2	51.7	975	24.5	2.23	3.52	1.2E+17	7.07	5.20	0.70	No	0.56	0.84	1.06	--
F 3	24.1	949	40.7	1.51	5.74	4.4E+17	8.17	3.12	1.19	Y	0.48	0.64	0.90	--
F 4	24.1	946	71.9	1.00	7.26	8.5E+17	8.55	2.01	1.69	Y	0.49	1.13	1.01	--
F 5	24.1	940	102.0	0.71	8.26	1.4E+18	9.32	1.43	2.19	Y	0.32	1.46	1.10	--
F 6	24.1	929	125.3	0.54	8.97	2.5E+18	10.61	1.05	2.70	Y	0.25	1.70	1.21	--
F 7	24.1	915	120.2		9.51	3.7E+18	11.42	0.84	2.70	Y	0.13	1.83	1.30	--

pass	$\varepsilon_{0.5}$	X_{dyn}	$t_{0.5}$ (s)	X	d if X >0.95 MRX	d if X >0.95 SRX	growth after MRX	growth after SRX	1000/T (K^{-1})	MFS + (MPa)	Sims (MPa)	Misaka (MPa)
F 1	0.6	0	1.27	0.55	9.5	28.6	20.5	51.7	0.79	134	142	137
F 2	0.6	0	0.39	0.80	8.0	17.4	8.0	24.1	0.80	162	166	165
F 3	0.6	0	8.48	0.00	7.1	12.5	24.1	24.1	0.82	172	185	176
F 4	0.6	0	2.32	0.00	6.4	8.6	24.1	24.1	0.82	210	209	213
F 5	0.6	0	2.11	0.00	6.0	7.2	24.1	24.1	0.82	235	236	234
F 6	0.7	0	3.46	0.00	5.5	6.5	24.1	24.1	0.83	255	243	251
F 7	0.7	0	4.79		5.4	6.2	24.1	24.1	0.84	265	267	260

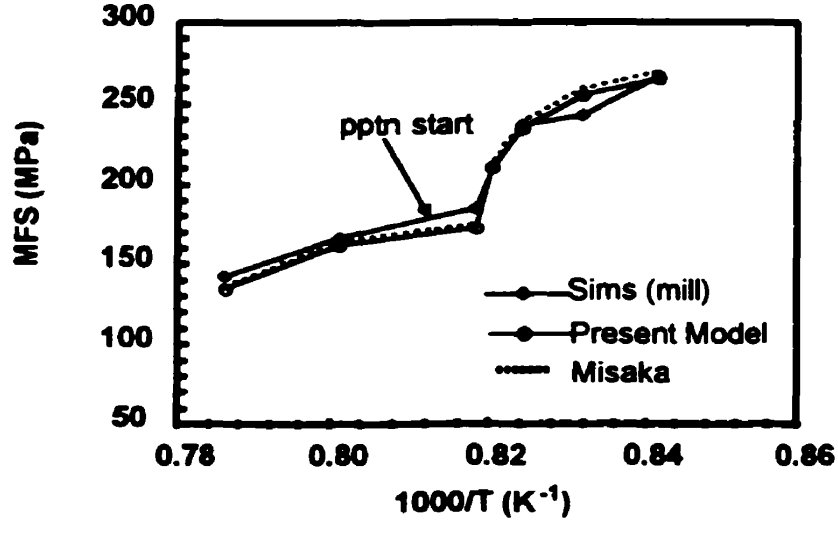

Figure 8.27 - MFS chart for grade AD12.

Grades AD11 and AD12 display similar behaviors. Firstly, they were rolled at relatively high temperatures, and considerable softening was observed during the interpass times, before precipitation occurred. This led to some grain refinement, but not to the same extent as produced by MDRX. The high Mn concentration (1.25%) delayed Nb carbonitride precipitation; nevertheless, because of the high Nb level, this occurred between the third and fourth passes for AD11 and between the second and third passes for AD12 (higher Nb). After precipitation starts, the strain was accumulated to 1.42 for AD11 and 1.83 for AD12. The absence of DRX agrees with the conclusion of Biglou et al. [10], who studied the same grade, but under different conditions (torsion testing, low strain rates). The Sims MFS curves are well predicted for both grades. In this case, the Misaka equation also provides a good prediction, probably due to the high Mn level.

8.4 - The Ferrite Grain Size After Transformation

The final ferrite grain size is one of the most important parameters involved in rolling, as it has considerable influence over the mechanical properties after coiling and cooling. The austenite grain size present after the last pass can be used as an input in a model for predicting the ferrite grain size. In their analysis of published data, Sellars and Beynon [124] derived a model that takes into account the accumulated strain, austenite grain size and cooling rate. In the present study, the cooling rate was taken as constant for all grades. There are different parameters for C-Mn and Nb steels. For the Cr-Mo steels, the parameters for the C-Mn steels are used here. The model is exemplified below, where d_α^0 is the ferrite grain size, and the effect of strain is not taken into account:

$$d_\alpha^0 = a + b\dot{T}^{-1/2} + c(1 - \exp(-1.5 \times 10^{-2} d_\gamma)) \qquad (8.1)$$

where T is the cooling rate in °C/s

d_γ is the austenite grain size.

The parameters a, b and c are given in Table 8.1:

Table 8.1- Parameters for Equation 8.1.

Steel	a	b	c
C-Mn	1.4	5.0	22
Nb	2.5	3.0	20

It is well known that residual strain in the austenite reduces the ferrite grain size, because the presence of an excess of dislocations increases the density of nucleation sites for the austenite-to-ferrite transformation. The presence of strain before transformation can be accounted for by the following equation, where d_α is the ferrite grain size after transformation:

$$d_\alpha = d_\alpha^0 (1 - 0.45\,\varepsilon^{1/2}) \tag{8.2}$$

For comparison purposes, a fixed cooling rate of 20°C/s was employed for all the grades considered here. The ferrite grain size predicted for each grade analyzed here is displayed in Table 8.2. According to the ferrite grain size model referred to above, the most important parameters that dictate the final size are the initial austenite grain size and the accumulated strain present before the strip is cooled on the run-out table.

It can be seen that all the C-Mn grades display similar behaviors, residual strains (about 0.27), and austenite grain sizes (about 15 μm) and, therefore, are characterized by similar ferrite grain sizes, about 5.5 μm. The different schedule variations (i.e. temperature, strain, strain rate, etc...) had little effect on the final result. Note that all these grades were rolled according to the DRCR paradigm.

Table 8.2-Input data, type of behavior and calculated ferrite grain size for each grade.

Group	Grade	Schedule type	$d\gamma$	ε	d_α^0	d_α
A	AA1	DRCR	7.7	0.80	5.4	3.2
	AA2	DRCR	6.3	0.27	5.0	3.8
	AA3	DRCR	6.1	0.24	4.9	3.8
	AS1	DRCR	9.8	0.83	5.9	3.5
	AS2	DRCR	6.6	0.58	5.1	3.3
	AB	DRCR	7.4	0.59	5.3	3.5
	AD1	DRX+PPT	13.3	0.99	6.8	3.8
	AD2	DRX+PPT	10.4	1.26	6.1	3.0
	AD3	DRCR	17.4	0.70	7.8	4.8
	AD4	CCR	75.6	1.60	16.7	7.2
	AD5	DRX+PPT	16.5	1.93	7.6	2.8
	AD6	DRX+PPT	16.9	1.57	7.7	3.3
	AD7	DRX+PPT	15.9	1.72	7.4	3.0
	AD8	DRX+PPT	16.8	1.52	7.6	3.4
	AD9	SRX	30.3	0.56	10.5	7.0
	AD10	SRX	29.2	0.52	10.3	6.9
	AD11	CCR	18.6	1.42	8.0	3.7
	AD12	CCR	24.1	1.83	9.2	3.6
	AM1	DRCR	11.2	0.32	6.3	4.7
C	CA	DRCR	15.4	0.33	7.1	5.2
	CS1	DRCR	13.4	0.29	6.5	4.9
	CS2	DRCR	15.6	0.26	7.1	5.5
	CD	DRCR	16.9	0.22	7.4	5.9
	CM	DRCR	16.3	0.35	7.3	5.4
	CU	DRCR	15.4	0.26	7.1	5.4
B	BCM	DRCR	14.6	0.87	6.8	4.0
	BCMVN	DRCR	16.8	0.58	7.4	4.9

The two Cr-Mo steels analyzed here were also rolled by DRCR methods, according to the model used in this study. However, there is more retained strain (0.87) in the BCM grade than in BCMVN (0.58) due to the different cycles of DRX

that apply to each schedule. This difference affects the final ferrite grain size slightly, with an end result of about 4μm for the BCM and 4.9 μm for the BCMVN grade.

There was more variation in the final ferrite grain sizes in the Nb grades, which fell in the range 2.8-7.2 μm. Analysing the data of Table 8.2, it appears that the occurrence of DRX always produces fine ferrite grains. The same can be said for the schedules in which DRX occurred in the initial passes, followed by precipitation. Here there was accumulated strain as well, which helped to maintain the ferrite grain sizes in the range 2.8 to 3.8 μm.

Only SRX was observed in the schedules applicable to grades AD9 and AD10; accordingly, the grain refinement was not so intense. The low strains and temperatures of the schedule and the low Nb level were responsible for this effect. The final austenite grain size was about 10 μm and the retained strain was about 0.5; this resulted in a ferrite grain size of about 7μm, which is larger than average.

Conventional controlled rolling leads to the presence of fine ferrite grains after transformation. In grades AD11 and AD12, which had undergone relatively large strains in the initial passes, the austenite grain size was refined by SRX. Subsequently, precipitation led to strain accumulation and these grades had large retained strains after the last pass (1.42 for AD11 and 1.83 for AD12); this state of affairs further contributed to refining the ferrite grain size. Another grade that underwent CCR was AD4, which had received light reductions and in which no DRX occurred during the entire schedule. In this case, the grain refinement was poor.

The finest final grain size was produced in grade AD5, in which DRX occurred in the initial passes and precipitation in the final passes, leading to a large accumulation of strain. The residual strain further refined the ferrite grain size, to an extent comparable to the grades that had cycles of DRX during the schedule (DRCR).

8.5 - General Remarks

Data taken from mill logs must be selected carefully. There are some numbers that are precisely recorded, such as the roll speed and strip thickness and width, but the roll forces must be checked with special attention. Systematic peaks can be found in the MFS curves, usually in the same stand in different grades such as Nb and C-Mn. This clearly indicates a miscalibration problem in the load cell.

The analysis could not be completed for grades BCMV, AM2 and AU. For the last two, the data were taken from the literature and there were insufficient data available for BCMV. The Sims MFS's for these grades displayed unusual shapes and the problems described above are probably responsible for the lack of agreement between predictions and measurements.

Note that the last stand MFS derived using the Sims equation is always slightly higher than that predicted by the present model. This discrepancy was also observed in a recent analysis and is attributed here to overestimation of the MFS by the Sims equation when small reductions are involved, as discussed in Section 5.4. Thus the latter does not apply to small strains, under which conditions there is less contribution from work hardening.

8.6 - Concluding Remarks

Several factors affect the rolling strategies that can be employed. Firstly, the maximum forces allowable on a mill can prohibit the use of CCR. In this particular case, large accumulated strains are generated, which lead to high rolling forces, especially in the final passes. Nevertheless, the use of CCR is quite simple when compared to DRCR or a mixture of DRCR and CCR. When CCR leads to forces that are too high for a given mill, some DRX+MDRX can be provoked in the beginning of the schedule, leading to an overall drop in the rolling force and to better austenite grain refinement. For mills with serious force limitations, true DRCR should be employed, which produces fine austenite grain sizes at low roll force levels. However, the rolling approaches that are possible are strongly related to the chemical composition of the steel under consideration. This study has pointed out that the composition has a very large effect on steel behavior during rolling. All the predictions were strongly influenced by the steel chemistry.

According to the present analysis, DRX is likely to occur during most finish rolling schedules. Although DRX followed by MDRX generally takes place in the initial passes, it does not make a large difference to the roll force predictions for the C-Mn steels, because the SRX kinetics are almost as fast as the MDRX kinetics at high temperatures in those materials. The behavior of the Nb grades, on the other hand, cannot be predicted without the aid of a mathematical model, such as the one described here.

Chapter 9 - Conclusions

A mathematical model was developed for the prediction of mean flow stress (MFS) during the hot strip rolling of Nb steels; it was then tested using industrial rolling data from different mills. In the present study, two main aspects were considered: mill log analysis and rolling simulation by torsion testing. Based on these two techniques and on the work presented in Chapters 3 to 8, the following conclusions can be drawn.

1- An expression for the redundant strain in flat rolling has been developed. For strip rolling, this falls in the range 0.07 to 0.16 times the nominal strain associated with each pass.

2- With the aid of the above redundant strain expression, together with factors for work roll flattening and forward slip, data from hot strip mill logs can be analyzed in terms of MFS vs. 1/T. This approach can be employed to determine the microstructural events that occur during the hot rolling of C-Mn, Cr-Mo, Nb-microalloyed and other grades of steel.

3- A model was developed to predict the MFS behaviour of plain C-Mn, Cr-Mo and Nb-bearing steels during strip rolling from the strains, strain rates, temperatures, and interpass times. It is based on an improved Misaka MFS equation and takes into account the quantities of the important alloying elements, the extent of recrystallization between passes, strain accumulation, and the possibility that dynamic recrystallization is initiated during a given pass. Good agreement is found between the model predictions and mill data.

4- The model indicates that dynamic recrystallization (followed by metadynamic recrystallization) occurs in the first few passes during the strip rolling of plain C-Mn grades. This is because the strains and temperatures are relatively high and the strain rates are quite low; thus the DRX critical strain can be readily exceeded in these passes. It should be noted, however, that the type of DRX observed here is not associated with strain accumulation. This is in sharp contrast to the case of Nb-containing steels, where strain accumulation plays an important role.

5- The peak strain associated with the occurrence of dynamic recrystallization in Nb-containing steels can be characterized by including a term that reflects the Nb level. This expression is required for accurate prediction of the critical strain for the initiation of dynamic recrystallization. The equation indicates that strain accumulation leading to dynamic recrystallization (followed by metadynamic recrystallization) occurs in the later passes when some of the Nb steels studied were rolled. Thus, when MFS predictions are made using only SRX equations (a softening mechanism that does not occur during the later passes of rolling), the predicted MFS values are much higher than those measured in the mill.

6- The $\varepsilon_c/\varepsilon_p$ ratio decreases with increasing Nb content in the present steels. (Here, ε_c represents the critical strain for the initiation of dynamic recrystallization and ε_p is the peak strain.). The elements Mn and Si have small (but not negligible) and opposite effects on the $\varepsilon_c/\varepsilon_p$ ratio. The relative effects (by weight or mass) of Nb, Si and Mn addition on the $\varepsilon_c/\varepsilon_p$ ratio are represented by the ratio 120:1.3:1. This is equivalent to about 13.5:1:2.6 for typical addition levels of these elements, respectively.

7- For the Nb steels, whether or not DRX + MDRX occurs in a given hot strip mill depends on the Mn and Si levels (in addition to the Nb concentration). It appears that the strain accumulation required to initiate DRX is more likely to take place when the Mn level is high (greater than 1.0 wt%) and the Si level is low (less than 0.1 wt%). These observations can be taken to imply that carbonitride precipitation is *absent* under the above conditions. Conversely, the presence of Si levels above about 0.1 wt% is likely to provoke precipitation during rolling and thus prevent the initiation and propagation of DRX.

8- The above observations indicate that Mn and Si have opposite effects on the rate of carbonitride precipitation. Increasing amounts of Si addition lead to faster kinetics, while increasing the Mn content retards the precipitation kinetics.

9- The precipitation start times applicable to strip mill rolling conditions can be predicted by modifying the Dutta and Sellars equation so as to take the Mn and Si levels into account. This can then be incorporated into a model of the MFS behaviour. The predictions obtained from the model described here are in good agreement with mill observations.

10- Mean flow stress, microstructure and precipitation models derived or 'tuned' with the aid of mill log data can be used to predict the metallurgical behavior of Nb steels during finish rolling.

Statement of Originality and Contribution to Knowledge

The present study includes the following original contributions:

1. A redundant strain equation was derived which can be used in any flat rolling model. Its simplicity does not require much computation time. In order to improve roll force calculations, it should be employed in association with roll flattening and forward slip corrections.

2. Compositional factors have been integrated into a previously developed mean flow stress equation that can now predict MFS values under a wide range of industrial conditions. The new equation allows for the solute effects attributable to the presence of various alloying elements.

3. The method used here to simulate grain size, fractional softening and strain-induced precipitation was used for the first time to follow the operation of the above mechanisms during the hot strip rolling of Nb steels.

4. Based on mill log analysis, an equation was derived to calculate the critical strain required to initiate dynamic recrystallization in Nb steels. The dependence of the above mentioned ratio on the "effective" Nb content was deduced for the first time.

5. By following the evolution of grain size and fractional softening, the model shows that it is possible to characterize the occurrence of strain accumulation followed by dynamic (plus metadynamic) recrystallization during hot strip rolling.

6. Evidence is presented for the first time that the elements Mn and Si have opposite effects on the critical strain/peak strain ratio and on strain-induced precipitation. These phenomena are explained in terms of the effects of Mn and Si on the diffusivity of Nb in austenite.

7. Based on the simulation results, it was shown that dynamic (followed by metadynamic) recrystallization occurred in most of the industrial rolling schedules analyzed.

References

[1] P.D. Hodgson: Ph.D. Thesis, University of Queensland, Australia, 1993, p. 3.

[2] Y.J. Hwu and J.G. Lenard: 37th MWSP Conference, ISS, Warrendale, PA, USA, 1996, p. 549.

[3] J.A. Biglou, M.S. Chun and J.G. Lenard: ISS Trans., 25 (1998), p. 63.

[4] E. Orowan: Proc. Inst. Mech. Eng., 150 (1943), p. 140.

[5] R.B. Sims: Proc. Inst. Mech. Eng., 168 (1954), p. 191.

[6] J.H. Hitchcock: Roll Neck Bearings, Appendix I, ASME, New York, 1935, p. 33.

[7] H. Ford and J.M. Alexander: J. Inst. Metals, 92 (1963-4), p. 397.

[8] Y. Misaka and T. Yoshimoto: J. Japan Soc. Technol. Plast., 8 (1967-8), p. 414.

[9] S. Shida: J. Japan Soc. Technol. Plast., 10 (1969), p. 610.

[10] J.A. Biglou, B.D. Nelson, D.R. Hall and J.G. Lenard: 37th MWSP Conference, ISS, Warrendale, PA, USA, 1996, p. 661.

[11] L.P. Karjalainen, T.M. Maccagno and J.J. Jonas: ISIJ Int., 35 (1995), p. 1523.

[12] M. Avrami: J. Chem. Phys. 7 (1939) p. 1103, 8 (1940) p. 212, 9 (1941), p. 177.

[13] W.A. Johnson and R.F. Mehl: Trans. AIME, 135 (1939), p. 416.

[14] A.N. Kolmogorov: Izv. Akad. Nauk. USSR-Ser-Matemat., 1 (1937), p. 355.

[15] C.M. Sellars: Hot Working and Forming Processes, ed. C.M. Sellars and G. Davies, The Metals Soc., London, 1980, p. 3.

[16] C.M. Sellars: Mat. Sci. Tech., 6 (1990), p. 1072.

[17] T. Senuma and H. Yada: 7th Risø Int. Symp., ed N. Hansen et al., Risø, Roskilde, Denmark, 1986, p. 547.

[18] H. Yada: Proc. Int. Symp. on Accelerated Cooling of Rolled Steel, ed. G.E. Ruddle and A.F. Crawley, Pergamon, 1988, p. 105.

[19] J.G. Williams, C.R. Killmore and G.R. Harris: Thermec '88, ed. I. Tamura, Tokyo, Japan, 1988, p. 224.

[20] P.D. Hodgson and R.K Gibbs: ISIJ Int., 32 (1992), p. 1329.

[21] P.D. Hodgson, L.O. Hazeldon, D.L. Matthews and R.E. Gloss: Microalloying '95, ed. M. Korchynsky et al., ISS of AIME, Warrendale, PA USA, 1995, p. 341.

[22] P. Choquet, P. Fabregue, J. Giusti, B. Chamont, J.N. Pezant and F. Blanchet: Mathematical Modelling of Hot Rolling of Steel, ed. S. Yue, CIM, Montreal, Canada, 1990, p. 34.

[23] W. Roberts, A. Sandberg, T. Siwecki and T. Werlefors: Int. Conf. Tech. Applications of HSLA Steels, ASM, Philadelphia, PA, 1983, p. 67.

[24] G. Li, T.M. Maccagno, D.Q. Bai and J.J. Jonas: ISIJ Int., 36 (1996), p. 1479.

[25] A. Laasraoui and J.J. Jonas: Metall. Trans., 21A (1991), p. 151.

[26] D. Q. Bai: Ph.D. Thesis, McGill University, 1995, pp. 18-19.

[27] M.J. Luton and C.M. Sellars: Acta Metall., 17 (1969), p. 1033.

[28] T. Sakai and J.J. Jonas: Acta Metall., 32 (1984), p. 189.

[29] D.C. Collinson, P.D. Hodgson and C.H.J. Davies: Thermec '97, ed. T. Chandra and T. Sakai, TMS, Warrendale, PA, 1997, p. 483.

[30] C. Roucoules, S. Yue and J.J. Jonas: Proc. Int. Conf. on Modeling of Metal Rolling Processes, The Inst. of Materials, London, UK, (1993), p. 165.

[31] C. Roucoules: Ph.D. Thesis, McGill University, 1992.

[32] P.D. Hodgson: Materials Forum, 17 (1993), p. 403.

[33] P.D. Hodgson: Thermec '97, ed. T. Chandra and T. Sakai, TMS, Warrendale, PA, 1997, p. 121.

[34] R.A.P. Djaic and J.J. Jonas: Metall. Trans., 4A (1973), p. 621.

[35] C. Roucoules, S. Yue and J.J. Jonas: Metall. Mat. Trans., 26A (1995), p. 181.

[36] T.M. Maccagno, J.J. Jonas and P.D. Hodgson: ISIJ Int., 36 (1996), p. 720.

[37] P.D. Hodgson, J.J. Jonas and S. Yue: Mat. Sci. Forum, 94-96 (1992), p. 715.

[38] C.M. Sellars and J.A. Whiteman: Met Sci., 13 (1979), p. 187.

[39] S. Yamamoto, C. Ouchi and T. Osuka: Thermomechanical Processing of Microalloyed Austenite, ed. A.J. DeArdo, TMS, New York, 1980, p. 613.

[40] J.G. Speer and S.S. Hansen: Metall. Trans. A, 20A (1989), p. 25.

[41] D. Q. Bai: Ph.D. Thesis, McGill University, 1995, pp. 28-32.

[42] C. Zener: in: C.S. Smith, Trans. AIME, 175 (1948), p. 11.

[43] A.F. Padilha and F. Siciliano Jr.: Encruamento, Recristalização, Crescimento de Grão e Textura, 2nd Ed., ABM, São Paulo, Brazil, 1996, pp. 63-71 (in Portuguese).

[44] L. Meyer, F. Heisterkamp and W. Mueschenborn: Microalloying '75, ed. M. Korchynsky, Washington, DC, USA, 1975, p. 153.

[45] L. Meyer, F. Heisterkamp, K. Hulka and W. Mueschenborn: Thermec '97, ed. T. Chandra and T. Sakai, TMS, Warrendale, PA, 1997, p. 87.

[46] S. Koyama, T. Ishii and K. Narita: J. Japan Inst. Metals, 35 (1971), p. 1089.

[47] S. Koyama, T. Ishii and K. Narita: J. Japan Inst. Metals, 35 (1971), p. 698.

[48] M.G. Akben, I. Weiss and J.J. Jonas: Acta Metall., 29 (1981), p. 111.

[49] B. Dutta and C.M. Sellars: Mat. Sci. Tech., 3 (1987), p. 197.

[50] W. Liu and J.J. Jonas: Metall. Trans. A, 20A (1989), p. 689.

[51] E. Valdes and C.M. Sellars: Mat. Sci. Tech., 7 (1991), p. 622.

[52] F.G. Arieta and C.M. Sellars: Int. Symp. on Low-Carbon Steels for the 90's, ed. R. Asfahani and G. Tither, TMS, 1991, p. 101.

[53] K.J. Irvine, F.B. Pickering and T. Gladman: J. Iron and Steel Inst., 205 (1967), p. 161.

[54] S.H. Park and J.J. Jonas: Mathematical Modelling of Hot Rolling of Steel, ed. S.Yue, CIM, Montreal, Canada, 1990, p. 446.

[55] T. Senuma, H. Yada, Y. Matsumura and T. Futamura: Tetsu-to-Hagane, 70 (1984), p. 322 (in Japanese).

[56] S.H. Park: Ph.D. Thesis, McGill University, 1991, p. 82.

[57] E. Scheil: Arch. Eisenhüttenwes., 12 (1935), p. 565 (cited in Ref. [56]).

[58] P.D. Hodgson - Deakin University, Australia: personal communication.

[59] L.N. Pussegoda, P.D. Hodgson and J.J. Jonas: Mat. Sci. Tech., 8 (1992), p. 63.

[60] F. Boratto, R. Barbosa, S. Yue and J.J. Jonas: Thermec 88, ed. I Tamura, ISIJ, Tokyo, Japan, 1988, p. 383.

[61] D.Q. Bai, S. Yue and J.J. Jonas: Proc. Int. Conf. on Modeling of Metal Rolling Processes, The Inst. of Materials, London, UK, (1993), p. 180.

[62] D.Q. Bai, S. Yue, W.P. Sun and J.J. Jonas: Metall. Trans. A, 24A (1993), p. 2151.

[63] T.M. Maccagno, J.J. Jonas, S. Yue, B.J. McCrady, R. Slobodian and D. Deeks: ISIJ Int., 34 (1994), p. 917.

[64] L.N. Pussegoda, S. Yue and J.J. Jonas: Metall. Trans., 21A (1990), p. 153.

[65] F.H. Samuel, S. Yue, J.J. Jonas and B.A. Zbinden: ISIJ Int., 29 (1989), p. 878.

[66] E.C. Sarmento and J.F. Evans: Proc. Int. Conf. on Processing, Microstructure and Properties of Microalloyed and Other High Strength Low Alloy Steels, ed. A.J. DeArdo, Iron and Steel Soc. of AIME, Warrendale, PA, USA, (1992), p. 105.

[67] Microalloying '75, International Symposium on HSLA Steels, Washington, DC, USA, 1975.

[68] M. Cohen and W. Owen: Microalloying '75, International Symposium on HSLA Steels, Washington, DC, USA, 1975, p. 2.

[69] F.B. Pickering: Microalloying '75, International Symposium on HSLA Steels, Washington, DC, USA, 1975, p. 9.

[70] T. Gladman, D. Dulieu and I.D. McIvor: Microalloying '75, International Symposium on HSLA Steels, Washington, DC, USA, 1975, p. 32.

[71] R.D. Stout: Microalloying '75, International Symposium on HSLA Steels, Washington, DC, USA, 1975, p. 488.

[72] P.H.M. Hart, R.E. Dolby, N. Bailey and D.J. Widgery: Microalloying '75, International Symposium on HSLA Steels, Washington, DC, USA, 1975, p. 540.

[73] J.J. Jonas and C.M. Sellars: Future Developments of Metals and Ceramics, ed. J.A. Charles et al., Institute of Materials, London, 1992, p. 148.

[74] E.A. Simielli, S. Yue and J.J. Jonas: Metall. Trans., 23A (1992), p. 597.

[75] I. Tamura, C. Ouchi, T. Tanaka and H. Sekine: Thermomechanical Processing of High Strength Low Alloy Steels, Butterworths, 1988, pp. 10-13.

[76] J.J. Jonas: Recrystallization '90, ed. by T. Chandra, Metall. Soc. AIME, Warrendale, PA, USA, 1990, p. 27.

[77] C.M. Sellars: 7th Risø Int. Symp., ed. N. Hansen et al., Risø National Laboratory, Roskilde, Denmark, 1986, p. 167.

[78] H.J. McQueen: Deformation Processing and Microstructure, ed. G. Krauss, ASM, 1984, p. 231.

[79] H.J. McQueen: Mat. Sci. Forum, 113-115 (1993) , p. 429.

[80] W. Roberts and B. Ahlblom: Acta Metall., 26 (1978), p. 801.

[81] C. Ouchi and T. Okita: Trans. ISIJ, 22 (1982), p. 543.

[82] R. Kaibyshev and O. Sitdikov: Recrystallization '96, ed. T.R. McNelley, Monterrey, CA, USA, 1996, p. 287.

[83] H.J. McQueen, E. Evangelista and M.E. Kassner: Zeitschrift für Metallkunde, 82 (1991), p. 336.

[84] H.J. McQueen, N.D. Ryan, E.V. Konopleva and X. Xia: Can. Metall. Quarterly, 34 (1995), p. 219.

[85] N. Pokutylowicz, F. Mucciardi and S. Yue: Proc. Int. Conf. on Modelling of Metal Rolling Processes, The Inst. of Materials, London, UK, 1993, p. 321.

[86] N. Pokutylowicz, L. Collins, D. Baragar and S. Yue: 37th MWSP Conference, ISS, Warrendale, PA, USA, 1996, p. 427.

[87] Hot Deformation of Metals, course notes, McGill University , 1994.

[88] J.H. Beynon and C.M. Sellars: ISIJ Int., 32 (1992), p. 359.

[89] H. Caglayan and J.H. Beynon: Proc. Int. Conf. on Modelling of Metal Rolling Processes, The Inst. of Materials, London, UK, 1993, p. 274.

[90] S.R. Wang and A.A. Tseng: Iron and Steelmaker, 23 (1996), p. 49.

[91] S. Torizuka, N. Ohkouchi, T. Minote, M Niikura and C. Ouchi: Thermomechanical Processing, Theory,, Modeling and Practice, ed. B Hutchinson et al., ASM, Stockholm Sweden, 1996, p. 227.

[92] T. Siwecki: ISIJ Int., 32 (1992), p. 368.

[93] S. Namba, M. Kitamura, M. Shimada, M. Katsumata, T. Inoue, H. Imamura, Y. Maeda and S. Hattori: ISIJ Int., 32 (1992), p. 377.

[94] J.J. Jonas and C.M. Sellars: Iron and Steelmaker, 19 (1992), p. 67.

[95] W.F. Hosford and R.M. Caddell: Metal Forming: Mechanics and Metallurgy, 2nd Ed., Prentice Hall, Englewood Cliffs, NJ, 1993, p. 222.

[96] Theory and Practice of Flat Rolling, Ed. by ISIJ, ISIJ, Tokyo, 1984, p. 7.

[97] D.S. Fields and W.A. Backofen: Proc. ASTM, 57 (1975), p. 1259.

[98] S.L. Semiatin, G. Lahoti and J.J. Jonas: Application of Torsion Testing to Determine Workability. ASM Metals Handbook, v. 8 (Mechanical Testing), 9th Ed., ASM, Metals Park, USA, 1985, p. 154.

[99] A. Kirihata, F. Siciliano Jr., T.M. Maccagno and J. J. Jonas: ISIJ Int., 38 (1998), p. 187.

[100] R.K. Gibbs, P.D. Hodgson and B.A. Parker: Recrystallization '90, ed. T. Chandra, TMS-AIME, 1996, p. 585.

[101] P.D. Hodgson: Mat. Sci. Tech., 12 (1996), p. 788.

[102] M. Militzer, W.P. Sun and J.J. Jonas: Acta Metall.Mater, 42 (1994), p. 133.

[103] I.V. Samarasekera, D.Q. Jin and J.K. Brimacombe: 38th Mechanical Working and Steel Processing Conf., ISS, Warrendale, PA, 1996, p. 313.

[104] C. M. Sellars: Metals Forum, 4 (1981), p. 75.

[105] C. M. Sellars: University of Sheffield, U.K., personal communication.

[106] F. Siciliano Jr. and J.J. Jonas: Microalloying in Steels, Microalloying in Steels: New Trends for the 21st Century, CEIT, San Sebastian, Spain, ed. J.M. Rodriguez-Ibabe et al., Trans-Tech Publications, 1998, p. 377; Materials Science Forun, 284-286 (1998), p. 377

[107] S. Kurokawa, J.E. Ruzzante, A.M. Hey and F. Dyment: Metal Science, 17 (1983) p. 433.

[108] L.T. Mavropoulos and J.J. Jonas: Canadian Metallurgical Quarterly, 28 (1989) p. 159.

[109] S. Akamatsu, T. Senuma and H. Yada: Mathematical Modelling of Hot Rolling of Steel, ed. S.Yue, CIM, Montreal, Canada, 1990, p. 467.

[110] Y. Saito, C. Shiga and T. Enami: Thermec 88, ed. I. Tamura, ISIJ, Tokyo, Japan, 1988, p.753.

[111] L. Meyer: Z. Metallkd., 58 (1966), p. 334.

[112] T.H. Johansen et al.: Trans. AIME, 239 (1967), p. 1651

[113] F. Kazinsky et al.: Jernkont. Ann., 147 (1963), p. 408.

[114] F. Siciliano Jr., K. Minami, T.M. Maccagno and J.J. Jonas ISIJ International, vol 36, 1996, p.1500.

[115] K. Minami, F. Siciliano Jr., T.M. Maccagno and J.J. Jonas ISIJ International, vol 36, 1996, p. 1507.

[116] F. Siciliano Jr., T.M. Maccagno and J.J. Jonas: International Conference on Thermomechanical Processing of Steel and Other Materials (THERMEC'97), University of Wollogong, Australia, July, 1997.

[117] F. Siciliano Jr. and J.J. Jonas ABM (Associação Brasileira de Metalurgia e Materiais), vol 53, 1997, p 95 (in Portuguese).

[118] F. Siciliano Jr. and J.J. Jonas The 7th International Conference on Steel Rolling, Tokyo, Japan, November, 1998.

[119] A. Schmitz, J. Neutjens, J.C. Herman and V. Leroy: 40th MWSP Conference, ISS, Warrendale, USA, 1998, p. 295.

[120] J. Neutjens, P. Harlet, T. Bakolas and P. Cantinieaux: 40th MWSP Conference, ISS, Warrendale, USA, 1998, p. 311.

[121] C. Ouchi, T. Sampei and I. Kozasu: Trans. Iron Steel Inst. Jpn., 22 (1982), p. 214.

[122] M.G. Akben and J.J. Jonas: Proc. Int. Conf. on Technology and Applications of HSLA Steels, ASM, Philadelphia, PA, 1983, p. 149.

[123] H.J. McQueen and J.J. Jonas: J. Appl. Metalwork., 3, (1985), p. 410.

[124] C.M. Sellars and J.H. Beynon: Proc. Conf. on HSLA Steels, ed. D.P. Dunne and T. Chandra, South Coast Printers, 1985, p. 142.

Appendix

In this section, a full calculation of the MFS's and grain sizes is shown. The example selected is the grade AS2 rolled at Sumitomo Metal Industries in Kashima, Japan. Note that the auxiliary parameters required for use of the Sims MFS calculation are displayed. The MFS chart obtained in this way follows the spreadsheets.

THE SIMS SPREADSHEET

The inputs (bold characters) are taken from the mill log.

Steel: AS2	Strip #:	241676
Temperature Info.		
TS Entry Temp (°C)=	1091	
TS-F1 moving Time (s)=	20.6	
F4-F5 interstand Temp (°C)=	964	

Pass	Roll radius (mm)	Width (mm)	Gauge (mm)	Temp (°C)	Roll Force (t)	Roll spd (rpm)	Forward slip ratio	Strip spd (m/min)
			26.40	**1091**				
F1	**394**	**1030**	**14.04**	**1007**	**1846**	**31.7**	0.116	90
F2	**399**	1030	**8.79**	**988**	**1544**	**50.2**	0.096	147
F3	**376**	1030	**5.77**	**980**	**1485**	**77.8**	0.091	221
F4	**362**	1030	**3.96**	**967**	**1446**	**109.9**	0.083	317
F5	**359**	1030	**2.96**	**963**	**1281**	**137.9**	0.067	422
F6	**366**	1030	**2.32**	**936**	**1066**	**168.8**	0.059	545
F7	**372**	1030	**1.96**	**909**	**849**	**175.0**	0.038	652

Steel: AS2				Strip #: 241676								Sims	Misaka
pass	ε	$\dot{\varepsilon}$ (s^{-1})	i.p. time (s)	Hitchcock R'(mm)	r	Φ_n	Y	Q	strip spd. (mm/min)	t def (s)	1000/T (K^{-1})	MFS (MPa)	MFS (MPa)
F1	0.62	13.43	3.65	406.2	0.47	0.064	15.694	1.648	90358	0.053	0.781	130.36	161.83
F2	0.60	25.80	2.25	424.6	0.37	0.045	9.646	1.822	146902	0.021	0.786	148.05	167.86
F3	0.53	46.91	1.49	415.5	0.34	0.036	6.298	2.017	221423	0.010	0.792	171.36	180.56
F4	0.46	77.01	1.04	424.2	0.31	0.028	4.312	2.223	317329	0.006	0.806	194.55	197.61
F5	0.36	105.92	0.78	456.9	0.25	0.021	3.180	2.344	422452	0.003	0.815	210.83	201.77
F6	0.31	142.58	0.61	485.7	0.22	0.017	2.457	2.499	545265	0.002	0.827	185.36	212.06
F7	0.20	143.95		571.1	0.15	0.011	2.055	2.419	651881	0.001	0.846	207.76	206.90

t_{def} = deformation time
r = reduction = (H-h)/H

MICROSTRUCTURE PREDICTION SPREADSHEET

The inputs (bold characters) are taken from the Sims spreadsheet.

pass	d (μm)	temp	$\dot{\varepsilon}$ (s^{-1})	i.p.time (s)	Z	K_s	t_{ps} (s)	SUM t_{ip}/t_{ps}	PPTN?	ε_{calc}	ε_a	ε_c	DRX?
F 1	80.0	**1007**	**13.4**	**3.66**	2.75E+16	4.17	218.6	0.02	No	**0.82**	0.82	0.82	Y
F 2	25.4	**998**	**26.8**	**2.25**	6.59E+16	4.46	147.2	0.03	No	**0.60**	0.60	0.53	Y
F 3	21.3	**990**	**46.9**	**1.49**	1.54E+17	5.14	75.1	0.05	No	**0.53**	0.53	0.56	–
F 4	23.2	**967**	**77.0**	**1.04**	4.91E+17	6.05	27.8	0.09	No	**0.46**	0.62	0.72	–
F 5	18.1	**963**	**106.9**	**0.78**	1.02E+18	6.97	14.9	0.14	No	**0.36**	0.73	0.72	Y
F 6	11.1	**936**	**142.6**	**0.61**	2.31E+18	8.56	22.7	0.17	No	**0.31**	0.31	0.65	–
F 7	10.7	**909**	**143.9**		5.46E+18	9.75	10.6	0.17	No	**0.29**	0.45	0.74	–

pass	$\varepsilon_{0.5}$	X_{dyn}	$t_{0.5}$ (s)	X	d if X>0.95 (μm)	d aft t_{ip} (μm)	d if X >0.95 (μm) MRX	(μm) SRX	MFS^+ (MPa)
F 1	0.6	0	0.17	1.00	14.0	25.4	14.0	62.4	151
F 2	0.5	0.1	0.13	1.00	12.5	21.3	12.5	35.7	156
F 3	0.5	0	0.87	0.69	34.5	23.2	11.0	34.5	167
F 4	0.6	0	1.36	0.41	32.8	18.1	9.6	32.8	193
F 5	0.6	0	0.10	1.00	8.7	11.1	8.7	25.0	214
F 6	0.5	0	1.99	0.19	31.6	10.7	7.8	31.6	193
F 7	0.6	0	22.69	0.00	24.2	10.7	7.4	24.2	222

THE MFS CHART